Regularization Formulations and Numerical Solutions for Image Processing

Stephen L. Keeling*

Abstract. This work is concerned both with the enhancement of bounded variation images as well as the extraction of usually smoother distributions from imaging data such as optical flows and intensity modulations. For these tasks, novel variational principles are formulated to select solutions which are preferred from an application-oriented perspective. These variational formulations are analyzed analytically and numerically, and they are efficiently implemented computationally. Specifically, formulations and discretizations of these variational principles are consistent with application requirements and free of expedient modifications such as convenient boundary conditions. Also, a geometric multigrid framework is developed for high-order optimality systems, and iterative schemes are adapted to be suitable for image processing systems used in a clinical environment.

Keywords: inverse interferometry, total variation, balanced-forward-backward, edge-flat-grey, concave filter, convex filter, dynamic contrast enhanced magnetic resonance imaging, tracer transport, magnetic resonance coil sensitivity estimation, sensitivity encoded image reconstruction, surface estimation, early vision, geometric multigrid, image registration and interpolation, generalized rigid, generalized affine, histological reconstruction, intensity scaling

Contents

1 Introduction

The most significant aspects of image processing are that images are generally non-smooth and often noise corrupted while desired information to be inferred from imaging data may indeed be smooth. For instance, objects displayed in measured images generally have edges which

*Institut für Mathematik und Wissenschaftliches Rechnen, Karl-Franzens-Universität Graz, Heinrichstraße 36, 8010 Graz, Austria; email: stephen.keeling@uni-graz.at; tel: +43–316–380–5156; fax: +43–316–380–9815.

give rise to sudden changes in intensity. When regarded as distributed as opposed to pixelated intensities, images are conceptualized as functions rich with discontinuities but nevertheless of bounded variation. With less regularity, a noise corruption is regarded as Lebesgue measurable and square integrable. By contrast, the flow of such irregular intensities within an image sequence may be so smooth as to correspond to a rigid body motion. Similarly, the illumination of a single scene may be quite smoothly varying even though it manifests itself only through a reflectivity varying discontinuously among objects in the scene. This work is concerned both with the enhancement of bounded variation images as well as the extraction of usually smoother distributions from imaging data such as optical flows and intensity modulations. Significant contributions are made for these tasks by formulating novel variational principles to select solutions which are preferred from an application-oriented perspective. These variational formulations are analyzed analytically and numerically, and they are efficiently implemented computationally. Specifically, formulations and discretizations of these variational principles are consistent with application requirements and free of expedient modifications such as convenient boundary conditions. Also, a geometric multigrid framework is developed for high-order optimality systems, and iterative schemes are adapted to be suitable for image processing systems used in a clinical environment.

It was first recognized in [73] that total variation regularization performs well to filter noise from images. Similarly, inverse problems in imaging can be solved effectively by penalized minimum residual methods using total variation penalties [1]. This approach is used in [27] and [28] for inverse interferometry, and the discrete approximation of the total variation is a central theme; see also [14]. In particular, it is shown in [27] that while images are naturally approximated on a grid of cells as piecewise constant, the total variation of the approximation does not converge to the total variation of the image unless the grid conforms to the level curves of the image. This condition can of course not be met by a grid constructed before the solution to an inverse problem is known. Alternatively, it is shown in [27] that the total variation may be redefined in a non-rotationally invariant fashion to achieve convergence on Cartesian grids.

Such penalized minimal residual problems may be solved by a descent method as used, e.g., in [73], or else a diffusion of variational energy may be formulated directly to define a sequence of image scales as discussed in detail in [80]. Using an image dependent diffusitivity in order to steer diffusion locally leads to nonlinear anisotropic diffusion filtering. A well known class of anisotropic diffusion methods are the Perona-Malik filters [69], which are used to sharpen edges. However, these methods only sharpen a narrow range of edge slopes which depends upon tuned parameters. On the other hand, it is found in [53] that nonlinear anisotropic diffusion filters exist which enhance edges over a wide range of edge slopes; see also [81] and [59]. This multiscale edge enhancement is accomplished in [53] with a so-called balanced-forward-backward filter employing a nonlinear and nonparametric diffusivity for which backward diffusion normal to levels sets is equal to forward diffusion tangent to level sets.

Variationally based filters divide naturally into those with a penalty function which is purely concave, e.g., balanced-forward-backward; purely convex, e.g., Gaussian; a mixture, e.g., Perona-Malik; and linear, i.e., total variation. While concavity is required for edge sharpening [65], concave filters as well as total variation suffer from a staircasing effect by which gradual variations are estimated by a sequence of steps [80]. Nevertheless, total variation is well suited to smoothing piecewise constant intensities while preserving edges [42]. Additionally, it was recognized in [42] that total variation can be modified with selective convexity to smooth intensities with gradual variations without staircasing. Such filters are called edge-flat-grey because of their suitability for image regions with edges, with flat zones and with grey or intermediate gradient scales. However, the boundaries between these three gradient scales are partitioned in [42] by parameters which require tuning. On the other hand, an edge-flat-grey filter satisfying certain extremal properties is constructed in [44] which depends only upon a single parameter defining the lower bound of edge scales. The filter is also compared extremely favorably with several other filters in [44] for their suitability to medical imaging with respect to denoising and

to segmentation pre-conditioning. The constructed edge-flat-grey filter has been applied in medical contexts as a preprocessor for diffusion tensor imaging in [6] and [7] and for segmentation in [3], [76] and [4].

In [51] intensity data are given in a temporal sequence of dynamic contrast enhanced magnetic resonance images measured while injected contrast agent is transported by convection and diffusion through imaged tissues. It is required to determine the spatial distribution of static transport properties from these data and to visualize potential pathology by imaging such properties. The measured intensity data are related algebraically to the dynamic distributed concentration of contrast agent, which in turn is related to local transport properties by voxelwise temporal convolution. The underlying convolution kernel has been related to transport properties in a purely parametric fashion in [31], [35], [43], [57] and [77], but for fully nonparametric deconvolution the main works in the magnetic resonance literature are [15] and particularly [67]. However, monotonicity constrained nonparametric deconvolution was first studied in this context in [51]. In this work it is shown that under an implicit bounded variation constraint, the monotonicity constrained solution readily manifests the staircasing effect, which is regularized in [51] with a suitable basis. Based upon compartmental analysis, an exponential basis is preferred in the physiological community, and a condition for monotonicity in an exponential basis is derived in [51] which is considerably more general than the standard established in [19]. This approach is used for the dense set of exponential functions with a harmonic distribution of time scales. Although the so implemented monotonicity constrained deconvolution is performed voxelwise without explicit spatial coupling, the imaged transport properties manifest a relative sharpness, typical of total variation regularization, while the often used approach of truncated singular value decomposition [67] manifests a relative blurredness, typical of Gaussian regularization. The study of an explicit spatial coupling is in preparation in joint work with the author of [30] using related regularization techniques.

This deconvolution work led to an investigation of precisely which information about transport properties can be inferred from even the most accurately recovered kernel. It is shown in [49] that the foundational work of [83], cited in most modern works, e.g., [15], [31], [35], [43], [57], [67], [77], requires revision. Specifically, in [83] intravascular and extravascular compartments are defined with separate distributions of tracer transport times, and it is shown in [49] that these distributions cannot be decoupled. A revised theory is built up from a fully distributed convection diffusion model from which the familiar convolution model can be derived using semigroup theory with explicitly articulated assumptions. Within this framework it is proved that perfusion dominated and permeation dominated tissues cannot be distinguished on the basis of a single convolution kernel alone. Nevertheless, it shown that transport properties such as mean transit time, effective volume fraction and volumetric flow rate per unit tissue volume can be identified from the kernel.

For such investigations involving dynamic contrast enhanced magnetic resonance imaging, temporal resolution is a particular challenge, since there is a trade-off between image clarity and temporal resolution. One mechanism for improving resolution is artificial and involves image interpolation as described below. Another mechanism involves to accelerate acquisition by measuring in parallel with coils which under-sample in a complementary fashion. Then the images measured in parallel suffer from aliasing and from a nonuniform sensitivity modulation, and to correct for these corruptions requires to estimate coil sensitivities. This task is similar to that, described earlier, of estimating a smoothly varying illumination of a scene from a discontinuously varying reflectivity among objects in the scene. In general, it is required to estimate a coil sensitivity in a global field of view within which tissues may move during a dynamic examination. While a more challenging procedure, generalizing [24], is presently under investigation, one possibility is that a sensitivity be estimated from a single static pair of images, one measured with the coil in question and the other measured with a uniformly sensitive coil. However, the measurements are corrupted by noise, the data are compactly supported and discontinuous at tissue boundaries, and yet the sensitivity is globally very smooth. Conventional

approaches for this problem have involved filtering techniques employing local polynomials [10] or other basis functions such as thin-plate splines [5] or wavelets [61]. In contrast to these parameterized approaches, whose disadvantages are discussed in [48], the estimation procedure proposed in [48] is to minimize a sum of a data residual and a high-order regularization suitable for exponentially varying sensitivities. In this form, the problem is related to the surface estimation problem of early vision [70]. While high-order operators are often expediently approximated with a product of low-order factors [54], such factorizations are shown in [48] to lead to conspicuously spurious boundary conditions for a sparce data support which is typical in the present context. Furthermore, while finite elements present a natural numerical approach for solving the optimality system, it is demonstrated in [48] that lumping of discontinuous data terms is required for regularized early vision problems in order to avoid aberrant consequences in the limit of vanishing regularization corresponding to an ever improving signal-to-noise ratio. The developed formulation is shown in [48] to perform very well for sensitivity encoded image reconstruction [71]. These techniques are applied in medical contexts in [7], [8] and [9].

This surface estimation problem, as well as the optical flow [41] and image registration and interpolation problems discussed below [63] [47], are early vision problems in the sense that dense spatial or spatiotemporal information must be inferred from sparse data in flat images or sequences of images [70]. Such problems are solved here with variational formulations employing in some cases high-order regularization. In order to solve the associated high-order optimality systems sufficiently rapidly for clinical applications and within image processing systems such as IDL, a corresponding geometric multigrid framework is developed in [50]; see also [55] for related multigrid work. Alternative algebraic multigrid formulations are ruled out because their application is generally constrained by an M-matrix condition which does not hold for discretizations of high-order problems [78]. It is shown in the developed framework that the convergence criteria of [34] are met. In particular, since in the present context the standard assumptions on the smoothness of coefficients and of the domain boundary do not apply [2], the techniques of [29] are adapted in [50] to prove the general elliptic regularity required. Further, the Galerkin formalism is used together with a multi-colored ordering of unknowns to permit vectorization of a symmetric Gauss-Seidel relaxation in image processing systems. Several implementation aspects, e.g., accurate and inaccurate floating point representations, apparently natural but inaccurate alternative finite difference formulations, and the effect of parameters including data support, are investigated in detail in order to achieve a robustly successful code for computing smooth solutions to early vision problems.

The geometric multigrid framework described above is adapted for image registration and interpolation in [45]. Specifically, images are said to be *registered* when an explicit coordinate transformation connecting like points is constructed. When a parameterized transformation permits images to be morphed one to the other, images are said to be *interpolated*. In [52], [45] and [46], a registration or interpolation method is said to be *generalized rigid* or *generalized affine* if it selects a rigid or an affine transformation, respectively, when one fits the given images. These concepts are formulated variationally by penalizing the departure of a transformation from being rigid or from being affine while necessarily avoiding expediently unnatural boundary conditions. Some authors relax rigidity by constraining transformations to be conformal or isometric [33]. Others employ a local rigidity constraint [58] or allow identified objects to move as rigid bodies [60]. Affine registration is also relaxed by parametric spline-based formulations regularized by penalizing second-order derivatives [74]. Such curvature based regularization has also been applied non-parametrically [25]. The motivation for considering generalizations of rigid or affine transformations lies in their applicability in two important categories of biomedical imaging. First, because of the ubiquity of rigid objects in the human body, generalized rigid registration and interpolation are of special interest, for instance, to facilitate medical examination of dynamic imaging data particularly by increasing the temporal resolution. Secondly, generalized affine registration and interpolation are of special interest, for instance, for object reconstruction from histological data since histological sections may be affine deformed in the

process of slicing.

In [45] it is shown that finite displacements can be formulated efficiently for generalized affine registration, as can optical flow additionally for generalized affine interpolation. On the other hand, it is shown in [52] that generalized rigid transformations are not selected by finite displacements regularized by linearized elastic potential energy, as used, e.g., in [26] and [68]. It is shown further in [52] that it is not feasible to regularize finite displacements with unlinearized elastic potential energy. By contrast, it is shown in [52] that generalized rigid registration is conveniently formulated by penalizing the departure from skew symmetry of the derivative of the optical flow. Furthermore, the penalty function can be patterned after total variation to permit discontinuities in optical flow corresponding to an object excision. The results of formulations of [45] and [46] are also found to be independent of image order when optical flow is used but in general not when finite displacements are used; see also [17] and [33].

All variational formulations described here for finite displacements and for optical flows produce a nonlinearity in the optimality system which results at least from the image similarity measure. Although nonlinear multigrid formulations have been considered for such nonlinearities, the geometric multigrid procedure is situated in [45] as an inner iteration within an outer quasi-Newton or lagged diffusivity iteration, which in turn is embedded within a pyramidal scheme that initializes each outer iteration from predictions obtained on coarser levels. Computations in [52] suggest that the optical flow used for registration can as well be assumed to be autonomous. However, an explicit counterexample is given in [45] to show the existence of images which lead to a non-autonomous optical flow in the general variational formulation. Nevertheless, it is found for practical examples that the optical flow may be assumed to be autonomous, and this assumption leads to a great computational savings with the added benefit that image interpolation is obtained for the cost of image registration. This autonomous flow approach is used in [45] to interpolate image pairs; furthermore, in [45] image sequences are registered with coupled finite displacements while sequences are interpolated pairwise with optical flow. On the other hand, a stronger coupling among neighboring interpolated images is obtained by computing autonomous flows of a semi-discretization as introduced in [45] for a work in preparation. Other multigrid formulations for other registration methods have been implemented successfully [36] [37], as have fast Fourier methods [26] [63]. Also, a prescribed correspondence between selected points, or landmark constraints, have been implemented for finite displacements, e.g., in [63] and [68], and these are formulated for optical flow in [47].

Although the simplest image similarity measure is based upon differences in pure intensities, the medical applications described above are complicated by the appearance of contrast agent or an intensity modulation in one image and not in another to which the first must be matched. For such applications, an image similarity measure is formulated and investigated in [46] which is based upon intensity scaling. This measure is introduced for both optical flow and for finite displacements. While other morphological image matching methods involve differentiation of potentially noisy image intensities [20] [21], the image similarity of [46] simply involves composition with scaling functions. Such rescaling is additionally found to have a smoothing effect on noisy images, even when the scaling functions are treated with Tikhonov regularization. It is found that the computational cost for the implementation of scaling functions is very small, and yet the resulting image similarity can provide a match between images which is closer than that obtained by a sum of squared differences alone.

2 Image Enhancement

2.1 Inverse Interferometry and Total Variation Approximation [27] [28]

The principal motivation in [27] is to solve an inverse interferometry problem in which a density perturbation $f = \rho - \rho_\infty$ in an axisymmetric flow field is to be determined non-invasively from a monochromatic intensity interference pattern ϕ such as shown in Fig. 1. This interference

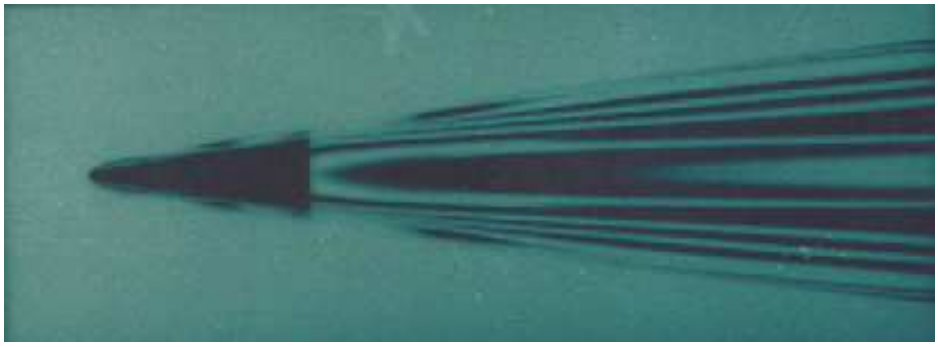

Figure 1: An interference pattern obtained by passing monochromatic light through a density perturbed fluid medium and adding the result to unperturbed light.

pattern is obtained by passing monochromatic light through the fluid medium and adding the density modulated result to unperturbed light. The density perturbation $f = f(x, r)$ is defined in a bounded cylindrical flow field, $(x, r) \in F$, where x varies along the cylinder axis and r varies radially up to the domain radius R. The intensity pattern $\phi = \phi(x, y)$ is measured in a bounded rectangular region, $(x, y) \in P$, where y varies orthogonal to the x direction. For a medium-specific constant G, the intensity ϕ is related to the desired density perturbation f according to:

$$\phi = \Phi f, \quad \phi(x, y) = G \int_y^R \frac{f(x, r)}{\sqrt{r^2 - y^2}} r dr. \tag{2.1}$$

An explicit inversion formula shows that Φ has a discontinuous inverse. Yet the regularized inverse must not rule out discontinuous density perturbations corresponding to high-speed flows. Thus, for given data $g \approx \phi$ the density perturbation f is estimated by minimizing the functional:

$$J_\mu(f) = \|\Phi f - g\|_{L^1(P)} + \mu TV(f), \qquad g \in L^1(P), \quad f \in BV(F) \subset L^1(F) \tag{2.2}$$

where TV denotes the total variation, or the BV semi-norm, which has the property addressed below that $BV(F)$-bounded sets are compactly embedded in $L^1(F)$ [23]. This estimation problem is formulated abstractly according to:

$$J_\mu(f) = D(\Phi f - g) + \mu U(f) \tag{2.3}$$

for $\Phi : X \to Z$, $D : Z \to \boldsymbol{R}$ and $U : Y \subset X \to \boldsymbol{R}$, e.g., $X = L^1(F)$, $Y = BV(F)$, $Z = L^1(P)$, and for computations according to:

$$J_\mu^N(f_N) = D^N(\Phi^N f_N - g_N) + \mu U^N(f_N) \tag{2.4}$$

for $f_N \in X^N$, $g_N \in Z^N$, $\Phi \approx \Phi^N : X^N \to Z^N$, $D \approx D^N : Z^N \to \boldsymbol{R}$ and $U \approx U^N : X^N \to Z^N$, where $X^N \subset Y \subset X$ and $Z^N \subset Z$ are finite dimensional spaces such as piecewise constant functions.

A central question in [27] concerns the convergence of minimizers of J_μ^N to minimizers of J_μ. For the existence of minimizers it is assumed that Y is compactly imbedded in X and that J_μ and J_μ^N are Y-coercive and lower semi-continuous on X and X^N respectively. For subsequential convergence of minimizers of J_μ^N to a minimizer of J_μ for a fixed μ, it is additionally assumed that J_μ and J_μ^N are consistent, uniformly Y-coercive, and that the spaces X^N possess the J_μ-approximation property, i.e., for every $f \in Y$ there exists a sequence $\{\tilde{f}_N\} \subset X^N$ which converges in X while $J_\mu(f) - J_\mu(\tilde{f}_N)$ vanishes.

The next approximation question concerns the convergence of minimizers with vanishing regularization. For this, the following conditions are added to those given above for the case that μ is fixed. Specifically, it is assumed that D and D^N are consistent, uniformly continuous on Z-bounded sets of Z and Z^N respectively, and that they coerce the Z-norm uniformly on

Z and Z^N respectively. Similarly, it is assumed that U and U^N are consistent, lower semi-continuous on X and X^N, respectively, and that they coerce the Y-norm uniformly on Y and X^N respectively. A technical difficulty emerges here when U is a semi-norm on Y. In this case it is assumed that operators $A : X \to \mathcal{N}$ and $A^N : X^N \to \mathcal{N}^N \subset X^N$ exist, e.g., the average value operators for interferometry, so that $(I - A)$ and $(I - A^N)$ are uniformly bounded in $\mathcal{L}(X, Y)$ and $\mathcal{L}(Y)$ while Φ and Φ^N coerce the Y-norm uniformly on the ranges of A and A^N respectively. Finally, it is assumed that the linear operators Φ^N and Φ are bounded and converge strongly and that the data g_N and g converge in Z. Then μ_N are chosen to vanish while $\mu_N^{-1} D^N(\Phi^N \tilde{f}_N - g_N)$ vanish, where $\tilde{f}_N$ approximate f^* according to the J_μ-approximation property. Under these conditions, minimizers f_N^* of $J_{\mu_N}^N$ are shown to converge to f^* when f^* is the unique solution to $\Phi f^* = g$.

The bottleneck in the above developed theory is to verify the J_μ-approximation property for a total variation penalty while using piecewise constant elements. On the other hand, when a density perturbation is smooth enough to lie in $W^{1,1}(F)$, the J_μ-approximation property can be established for the inverse interferometry problem using continuous piecewise linear elements as stated in the following and proved in [27].

Proposition 1 *Suppose that $\{X^N\}$ is a sequence of spaces of piecewise linear continuous functions with the property that $\inf_{\chi \in X^N} \|f - \chi\|_{W^{1,1}(F)} \to 0$ as $N \to \infty$ for all $f \in W^{1,1}(F)$. Then the J_μ-approximation property holds for (2.2).*

However, when the desired density perturbation is not smooth, piecewise constant elements are more natural, and an explicit calculation shows that the J_μ-approximation property fails. Specifically, let $f \in C^1(F)$ be chosen conveniently smooth so that $TV(f) = \int_F |\nabla f|_{\ell_2} dxdr$. Let F be discretized with a smooth curvilinear grid whose grid lines are parameterized by constant $\xi(x, r)$ and $\eta(x, r)$. For convenience define $\boldsymbol{\xi} = (\xi, \eta)$ and $\boldsymbol{x} = (x, r)$, and let h be the maximum diameter of any cell. Finally, let f_N be constant on grid cells assuming on each cell the value of f at a cell center. Then in [27], $TV(f_N)$ is shown to converge as follows:

$$TV(f_N) \xrightarrow{h \to 0} \int_F |(\partial \boldsymbol{x}/\partial \boldsymbol{\xi})^{\mathrm{T}} \nabla f|_{\ell_1} |\partial \boldsymbol{\xi}/\partial \boldsymbol{x}| dxdr \quad \text{while} \quad TV(f) = \int_F |\nabla f|_{\ell_2} dxdr. \tag{2.5}$$

Therefore, $TV(f_N) \to \int_F |\nabla f|_{\ell_1} dxdr \neq TV(f)$ holds in case the grid is Cartesian with $\partial \boldsymbol{\xi}/\partial \boldsymbol{x} = I$. On the other hand, if the grid conforms to the level curves of f according to $\nabla \xi = \nabla f / |\nabla f|_{\ell_2}$, $\nabla \eta = \nabla f^\perp / |\nabla f|_{\ell_2}$ and $|\partial \boldsymbol{\xi}/\partial \boldsymbol{x}| = 1$, then $TV(f_N) \to TV(f)$ holds. Nevertheless, such a grid cannot easily be known in advance. This result leads to the following alternative definition of the total variation:

$$TV_p(f) = \sup_{\Psi \in \mathcal{C}_p} \int_F f \nabla \cdot \Psi dxdr, \quad \mathcal{C}_p = \{\Psi \in C_0^1(F, \boldsymbol{R}^2) : |\Psi|_{\ell_q} \leq 1, 1/q + 1/p = 1\}. \tag{2.6}$$

Since TV_p is p-independent for piecewise constant elements on Cartesian grids, the calculation above suggests to use TV_1 to obtain the following. Note that similar results have been established in [14].

Proposition 2 *Suppose that $\{X^N\}$ is a sequence of spaces of piecewise constant functions defined on Cartesian grids made of identical cells with vanishing diameter as $N \to \infty$. Then when $TV_2(f)$ in (2.2) is replaced by $TV_1(f)$, the J_μ-approximation property holds for $\{X^N\}$.*

For the full discretization of the inverse interferometry problem, let both P and F be discretized by Cartesian grids made respectively of identical cells having widths and heights (h_x, h_y) and (h_x, h_r) and diameters which vanish with grid refinement. Define X^N as functions which are piecewise constant on the grid of F. Also, define $\Pi_{Z^N} : Z \to Z^N$ so that $\Pi_{Z^N} v$ assumes the average value of v on grid cells. Then take $\Phi^N = \Pi_{Z^N} \Phi$ and $g_N = \Pi_{Z^N} g$ and define:

$$J_\mu^N(\chi) = \|\Phi^N \chi - g_N\|_{L^1(P)} + \mu TV_1(\chi). \tag{2.7}$$

With these definitions, the following is proved in [27].

Theorem 1 *Let J_μ be defined by (2.2) with TV_2 replaced by TV_1, and let J_μ^N be defined by (2.7). Then J_μ and J_μ^N have minimizers in $L^1(F)$ and X^N respectively. Also a subsequence of minimizers f_N^* of J_μ^N over X^N converges to a minimizer of J_μ. If there is a unique $f^* \in BV(F)$ such that $\Phi f^* = g$, then μ_N for $J_{\mu_N}^N$ can be chosen to vanish in a way so that f_N^* converges in $L^1(F)$ to f^*.*

Also, uniqueness of solutions to $\Phi f = g$ is established in [27] in terms of Laplace Transforms. In addition, Theorem 1 is proved in [27] with (2.7) replaced by an approximate cost function which *rounds off the corners* of the absolute values appearing in J_μ according to $|\chi| \approx \sqrt{\gamma^2 + \chi^2}$ so that the resulting cost is differentiable.

The results of solving the inverse interferometry problem numerically, as explained in detail in [28], are shown graphically in Fig. 2. Specifically, a synthetic density perturbation corre-

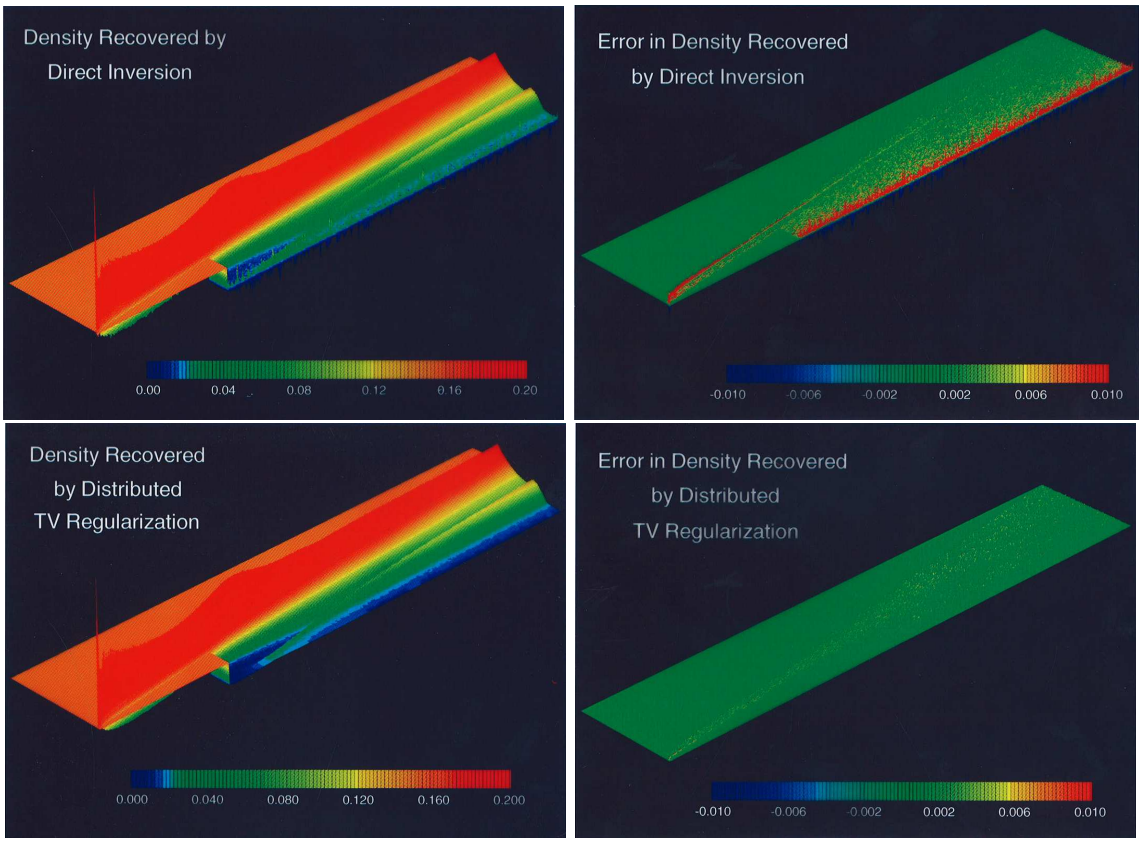

Figure 2: The results of solving (2.1) by direct inversion and by distributed total variation regularization are shown respectively above and below in the left column while the associated errors are shown in the right column. The left and right edges of each rectangular plot region correspond to $x = x_{\min}$ and $x = x_{\max}$ respectively while the upper and lower edges correspond to $r = R$ and $r = 0$ respectively.

sponding to the flow field shown in Fig. 1 is corrupted with noise, and the simulated data are used to solve (2.1) by the two methods compared in Fig. 2. One method involves direct inversion of (2.1). The other method involves minimization of a cost function in which absolute values are rounded as described above and in which total variation regularization is applied in a distributed fashion and weighted as $1/r$ in accordance with (2.1). The results from direct inversion and from distributed total variation regularization are shown respectively above and below in the left column of Fig. 2 while the associated errors are shown in the right column. Clearly, the result with total variation regularization is more accurate.

2.2 Anisotropic Diffusion Filtering [53]

The work of [53] was motivated by the need for segmentation preprocessing to extract the morphology of atherosclerotic vessels from magnetic resonance images of the type shown shown below in Fig. 4 and used in [3], [76] and [4] for the assessment of plaque stability. The approach of [53] is that of nonlinear anisotropic diffusion filtering which is based on nonlinear evolution partial differential equations of the form:

$$\partial_t u = \nabla \cdot (g(|\nabla u|)\nabla u), \qquad u(0) = u_0 \tag{2.8}$$

where u_0 is an unfiltered image, and after some diffusion time t, $u(t)$ is the filtered image. A nonlinear diffusivity g depends upon the image in order to steer diffusion locally and thereby to avoid the excessive smoothing associated with linear diffusion techniques. The method is said to be anisotropic since direction dependent diffusion results from the nonlinearity as can be seen below in (2.9). Such an approach is oriented to improve images in a fashion which is more qualitative than quantitative as noise is reduced while certain details are preserved and certain features enhanced.

Defining $u_{\nu\nu}$ as the second derivative of u in the direction of ∇u, the diffusion in (2.8) can be decomposed into the following two diffusion terms which respectively capture diffusion normal and tangent to the level sets of u:

$$\partial_t u = \Phi'(|\nabla u|)u_{\nu\nu} + g(|\nabla u|)(\nabla^2 u - u_{\nu\nu}). \tag{2.9}$$

Such filters are usefully classified according to the properties of the flux function $\Phi(s) = sg(s)$. For instance, the Perona Malik filters [69] are characterized by a flux function which is first increasing and then decreasing, as can be seen in the following popular example in which $\Phi'(\lambda) = 0$ defines the contrast parameter λ:

$$g(s) = \exp\left[-\tfrac{1}{2}\left(\tfrac{s}{\lambda}\right)^2\right], \quad \Phi'(s) = \frac{1 - \left(\frac{s}{\lambda}\right)^2}{\exp\left[\frac{1}{2}\left(\frac{s}{\lambda}\right)^2\right]}. \tag{2.10}$$

For such filters, diffusion normal to the level sets of u is forward where variations in u are sufficiently small, i.e., $|\nabla u| < \lambda$, and it is backward where variations in u are sufficiently large, i.e., $|\nabla u| > \lambda$. Diffusion tangent to the level sets of u is always forward since $g(s) > 0$. Thus, intra-region diffusion is favored over inter-region diffusion. However, the contrast parameter implicitly defines the regions which are flattened by intra-region forward diffusion as well as the edges of these regions which are to be strengthened by inter-region backward diffusion. Computational experiments with Perona-Malik filters in [53] demonstrate that diffusivities with a narrower bell shape, as in (2.10), will create sharper edges in a narrower range of edge slopes, while diffusivities with a wider bell shape, as in $g(s) = [1 + (\frac{s}{\lambda})^2]^{-1}$, will sharpen edges over a wider range of edge slopes. The goal in [53] is to derive diffusivities which can be used to achieve edge enhancement over a wide range of edge strengths without suffering from a sensitivity to parameters such as the contrast parameter λ or a regularization parameter σ in $g(|\nabla u_\sigma|)$ where $u_\sigma = K_\sigma * u$ is a convolution with a Gaussian kernel K_σ of width σ.

Continuum level analysis of smooth images (cf. [69], [12] and [81]) shows first that the diffusivity should be chosen so that u_ν increases at edges, i.e., so that $\partial_t u_\nu > 0$. Furthermore, to avoid staircasing requires that $\partial_t u_\nu$ be locally maximal in the normal direction, i.e., that $\partial_t u_{\nu\nu} = 0$ and $\partial_t u_{\nu\nu\nu} < 0$ at edges. Assuming that normal derivatives of even order vanish at edges leads from (2.9) to the following explicit formulation of these conditions for one-dimensional images:

$$\begin{aligned} \partial_t u_\nu &= \Phi' u_{\nu\nu\nu} > 0 \\ \partial_t u_{\nu\nu} &= 0 \\ \partial_t u_{\nu\nu\nu} &= 3\Phi'' u_{\nu\nu\nu}^2 + \Phi' u_{\nu\nu\nu\nu\nu} < 0. \end{aligned} \tag{2.11}$$

Assuming that normal derivatives of odd order alternate in sign means that these conditions can be met with $\Phi' < 0$ and $\Phi'' < 0$. If the flux function has a single peak at λ and a single inflection point at χ, then edge slopes satisfying $\lambda < |u_x| < \chi$ are heightened at a locally maximal rate which leads to sharpening. Otherwise, smaller slopes with $|u_x| < \lambda$ are blurred and larger slopes with $|u_x| > \chi^+$ (i.e., $\Phi'' > \frac{1}{3}|\Phi'|u_{\nu\nu\nu\nu\nu\nu}u_{\nu\nu\nu}^{-2}$) are heightened at a locally minimal rate which leads to staircasing. In higher dimensions, the situation is more complex since tangential diffusion can contribute to edge development by flattening homogeneous regions, and it can also contribute to edge degradation by drawing edge mass tangentially away.

Aside from this continuum level analysis, it is found in practice that separate Perona-Malik diffusivities with the same values for λ and χ can still provide very different edge enhancement results. Computational experiments performed for [53] suggested that the most uniformly effective diffusivity would be that for which the normal diffusion coefficient Φ' in (2.9) would be as uniformly negative as possible. For example, if M is the maximum possible gradient magnitude on a given grid, then defining $g(s) = (M - s)/s$ gives $\Phi'(s) = -1$. This approach is successful for one-dimensional images, but for two-dimensional images excessive smoothing results apparently since the tangential diffusion coefficient g is so much larger in magnitude than the normal diffusion coefficient Φ'. Such tangential smoothing can be explicitly subtracted away, as seen in the shock filters of [66], but a dissipative mechanism is desirable for noise reduction. These considerations suggest to balance smoothing in the tangential direction with sharpening in the normal direction as follows:

$$-1 = \frac{\Phi'(s)}{g(s)} = \frac{sg'(s) + g(s)}{g(s)} \quad \text{to obtain} \quad g(s) = \frac{1}{s^2}. \tag{2.12}$$

Computational results shown below in Fig. 3 demonstrate that this *balanced forward-backward* (BFB) diffusivity can sharpen edges over a wide range of slopes. On the other hand, to control the enhancement of noise, such as in Fig. 4 below, the balance can be introduced gradually in the *parameterized BFB-κ* diffusivity as follows:

$$-\frac{s}{\kappa + s} = \frac{\Phi'(s)}{g(s)} = \frac{sg'(s) + g(s)}{g(s)} \quad \text{to obtain} \quad g(s) = \frac{1}{s(\kappa + s)}. \tag{2.13}$$

The BFB-κ diffusivity follows the TV model, $g(s) = s^{-1}$, for gradients that are small in relation to κ, and then it passes to the BFB model for gradients that are large in relation to κ. By comparison, all Perona-Malik diffusivities follow the Gaussian model, $g(s) = 1$, for small gradients, while only $g(s) = [1 + (\frac{s}{\lambda})^2]^{-1}$ follows the BFB model for large gradients. Since the BFB and the BFB-κ filters never follow the Gaussian model, they do not introduce normal smoothing for any gradient magnitudes. Paradoxically, in spite of such extremely limited dissipation in (2.12) and (2.13), these filters are seen in computational experiments to be remarkably stable and effective for image enhancement.

Since most implementations of nonlinear anisotropic filters are based upon finite differences and single-step time stepping [80], such discretizations are used for the comparisons shown in [53]; however, because of the requirements of the unbounded diffusivities, implicit time stepping is implemented uniformly instead of using the more usual explicit methods where they might be applicable. The unbounded diffusivities are computed numerically according to $g(\max\{s, \varepsilon\})$, where ε is simply chosen small enough for results to be insensitive to its variation. Time stepping equations are solved only approximately using a few iterations of a Jacobi preconditioned conjugate gradient scheme.

The diffusion operator is discretized compactly at cell centers in a diagonal fashion using cell corners. Horizontal-vertical discretizations necessarily involve a broader stencil for the gradient calculation; consequently, they are more dissipative and conspicuously so where the gradient is diagonally oriented. The diagonal discretization employed involves interleaved (red-black) diagonal grids coupled through the diffusivity calculated from the gradient at cell corners. In

some cases, the coupling can be weak enough that diagonal artifacts may result [65]; however, for images with mildly well behaved statistics, this coupling is sufficient.

Several filters are compared in [53] and representative results can be summarized as follows. First consider the synthetic image u_0 shown on the left in Fig. 3. Here, u_0 is a sum of six

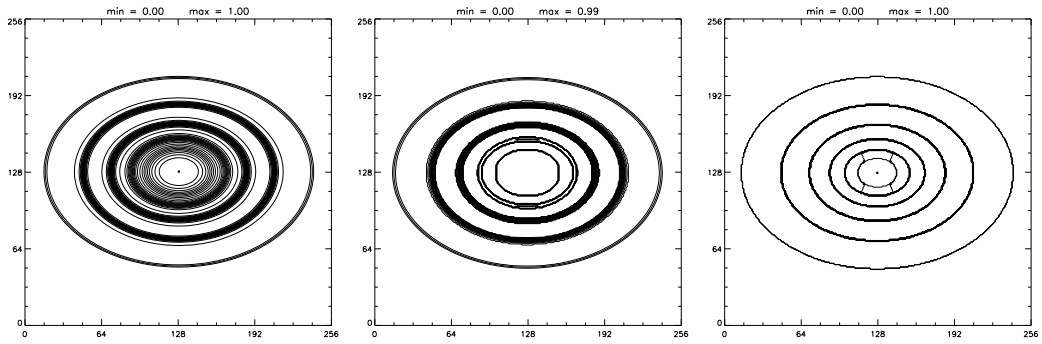

Figure 3: On the left is an unfiltered image u_0 containing six edge strengths which are progressively weaker toward the image center. A lined contour plot with unequally spaced levels $\{(i/i_{\max})^{1/4}\}$ is used to accentuate small-slope features near the center of each image. The image u_0 is filtered using (2.10) and (2.12), and the results are shown respectively in the middle and on the right.

functions of the form $a(1+bx^2+cy^2)^{-d}$ chosen to create ever weaker edges. Then u_0 is filtered using (2.10) and (2.12), and the results are shown respectively in the middle and on the right. A lined contour plot with unequally spaced levels $\{(i/i_{\max})^{1/4}\}$ is used to accentuate small-slope features near the center of each image. Note that the Perona-Malik filter can only be tuned to capture one of the edges, the fifth from outside in the present case, and otherwise the innermost region is flattened while other edges are staircased. On the other hand, the BFB filter clearly captures all six edge strengths.

The filters are compared in terms of measured magnetic resonance images in Fig. 4. Shown here on the left is u_0 an unfiltered magnetic resonance image of an atherosclerotic vessel. Then u_0 is filtered using (2.10) and (2.13), and the results are shown respectively in the middle and on the right. The parameters λ for (2.10) and κ for (2.13) are chosen just large enough to smooth the background noise. In the middle image, this choice also levels the signal into smoothly shaped flat zones bounded by high contrast edges to which λ happens to be tuned. The result creates a kind of *watercolor* effect in the image. On the other hand, the BFB-κ filter captures image features more realistically by preserving edges while significantly reducing the noise level. Even though tangential smoothing is the only explicit dissipative mechanism for this filter, such limited smoothing performs remarkably well at noise reduction.

2.3 Edge-Flat-Grey Filtering [44], [6], [7] ([3], [76], [4])

As explained above, the work of [53] was motivated by the requirements of the studies of [3], [76] and [4], but it was finally a filter developed in [44] which was used to preprocess magnetic resonance images of atherosclerotic vessels for segmentation and subsequent assessment of plaque stability. All the filters studied in [44] are variationally based. Specifically, for an unfiltered image u_0 defined on an image domain P let u be a filtered image defined as a minimizer for the functional:

$$J(u) = \int_P \phi(|\nabla u|)dx + \frac{\mu}{2}\int_P |u_0 - u|^2 dx \tag{2.14}$$

for which the necessary optimality condition is expressed in the steady state for the following descent minimization method:

$$\left\{\begin{array}{rcll} \partial_t u & = & \nabla\cdot(g(|\nabla u|)\nabla u) + \mu(u_0-u), & P\times[0,\infty) \\ u_n & = & 0, & \partial P\times[0,\infty) \\ u(0) & = & u_0, & P. \end{array}\right. \tag{2.15}$$

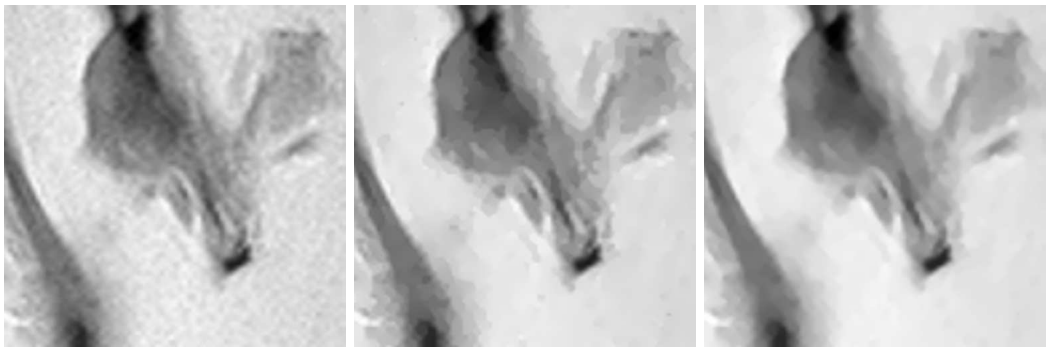

Figure 4: On the left is an unfiltered magnetic resonance image u_0 of an atherosclerotic vessel. The image u_0 is filtered using (2.10) and (2.13), and the results are shown respectively in the middle and on the right.

Here, the variational penalty function ϕ gives the diffusivity $g(s) = \phi'(s)/s$, and as in (2.9),

$$\partial_t u = \phi''(|\nabla u|)u_{\nu\nu} + g(|\nabla u|)(\nabla^2 u - u_{\nu\nu}) + \mu(u_0 - u) \tag{2.16}$$

u_ν is the partial derivative of u in the direction ∇u. Such filters are also implemented by nullifying μ and alternatively choosing a final diffusion time as a regularization parameter. In either case, this diffusion can be seen as a natural filtering process in which undesirable image features are dissipated while desirable features are either preserved or accentuated.

These filters are usefully classified according to whether the variational penalty function ϕ is convex ($\phi'' > 0$), concave ($\phi'' < 0$), or mixed in the sign of ϕ''. This classification is revealing since convexity has a smoothing effect on the filtered image, while concavity is necessary for edge sharpening [65]. On the one extreme of convexity is classical Gaussian filtering which is known for its excessive smoothing properties [80]. On the other extreme of concavity is balanced-forward-backward (BFB) diffusion filtering [53] which provides multiscale edge enhancement over a wide range of slopes. Perona-Malik filtering [69] involves combining a zone of convexity with a zone of concavity, but such filters are necessarily tuned to enhance a narrow range of edge slopes; otherwise, edges are either blurred or staircased [53]. At the interface between convexity and concavity is total variation (TV) filtering [73] for which $\phi'' = 0$. TV filtering is known for its excellent reconstruction of apparently piecewise constant or *blocky* images. However, while TV filtering provides excellent edge preservation and excellent smoothing of flat regions, it suffers from a well known staircasing effect in regions with gradual image variations [80]. In other words, TV filtering treats *edge* and *flat* scale gradients well, but not *grey* scale gradients; therefore, edge-flat-grey (EFG) scale filtering [42] was developed by making ϕ'' strictly positive for grey scales. Finally, Gauss-TV filtering [75] can be used to treat images as consisting of only grey and edge scale gradients.

The suitability of a given filter for medical imaging in particular depends naturally upon the specific goal of interest, and two classes of objectives are identified in [44]. On the one hand, it may be necessary to remove image noise without altering any underlying image details. Such denoising can be required, for example, prior to further quantitative image processing which can be particularly susceptible to measurement error; consider, e.g., diffusion tensor imaging [7]. On the other hand, it may be necessary to enhance specific features qualitatively by significantly modifying the image at the expense of quantitative accuracy. For example, accentuation of edges [53] or of fibers [80] can greatly facilitate a detailed visual examination of (potentially pathological) sites containing such features. Also, a reduction in the image histogram spread, or rather an increased flattening of homogeneous image regions, can greatly facilitate the segmentation of an image into its component tissue types. In [44] a specific edge-flat-grey filter satisfying certain extremal properties is constructed and compared with several filters once applied to measured noisy magnetic resonance images, and the results are discussed primarily with respect to the goal of denoising. However, since some of these filters

apparently provide good edge enhancement or good segmentation pre-conditioning, these goals are discussed as well. It is apparent from the results that convex total variation based filters can be implemented to perform very well for the medical imaging objectives explained here.

The excellent performance of total variation for filtering blocky images can be understood from (2.16), since the TV penalty function $\phi(s) = s$ provides neither forward nor backward diffusion normal to level sets. Thus, edges are neither sharpened nor smoothed, but rather *preserved* during diffusion filtering. On the other hand, the pure tangential diffusion effectively smoothes flat regions of an image. However, by adding $\mu(u_0 - u)$ to the right side of each line in (2.11) it can be seen that the reaction term can contribute to staircasing [12].

To overcome these disadvantages, the following novel edge-flat-grey function,

$$\phi(s) = \int_0^s \sigma g(\sigma) d\sigma, \quad g(s) = \begin{cases} \frac{1}{s} e^{-q(s)^2} & 0 \le s \le \gamma \\ \frac{1}{s} & s \ge \gamma \end{cases}, \quad q(s) = 1 - \left(\frac{s}{\gamma}\right)^2 \tag{2.17}$$

is introduced in [44] as a smooth variational penalty function meeting the conditions set forth in [42] while providing excellent EFG scale filtering. To motivate the definition of the function (2.17), suppose for simplicity that $\gamma = 1$ and observe that the EFG penalty function takes the following form on the interval $[0, 1]$:

$$\phi'(s) = e^{-(1-s^2)^2} = s^{p(s)-1} \quad \text{with} \quad p(s) = 1 + \frac{(1-s^2)^2}{\log(1/s)}. \tag{2.18}$$

Thus, the EFG penalty corresponds roughly to an L_p penalty on $|\nabla u|$ where p varies as shown in the left plot of Fig. 5. Also, shown on the right in Fig. 5 is a plot of $\phi''(s)$ on the interval

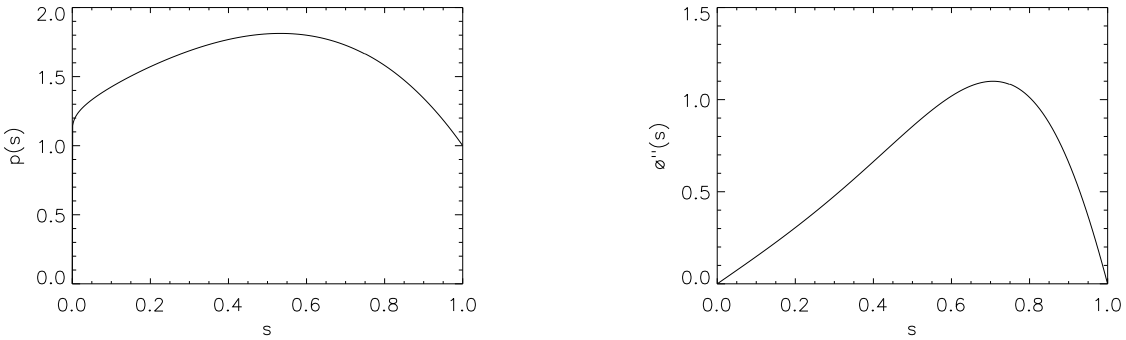

Figure 5: For $\gamma = 1$ the exponent p from (2.18) is shown on the left and ϕ'' in (2.16) is shown on the right.

$[0, 1]$. Note further that $p(0) = p(1) = 1$ and that $\phi'''(s)$ is bounded. In light of (2.16), the plot of $\phi''(s)$ illustrates that diffusion normal to level sets of u is strictly positive for a range of gradient magnitudes, but drops to zero for sufficiently large and for vanishing gradients. Thus, the EFG filter flattens image regions with small gradients $|\nabla u| \approx 0$, it smooths image regions with gradual variations $|\nabla u| < \gamma$, and it preserves edges with $|\nabla u| > \gamma$.

As in [53], the numerical implementation of (2.15) in [44] is based upon finite differences and single-step implicit time stepping, where unbounded diffusivities are computed numerically according to $g(\max\{s, \varepsilon\})$, and time stepping equations are solved only approximately using a few iterations of a Jacobi preconditioned conjugate gradient scheme. On the other hand, the diffusion operator is discretized in [44] in a Cartesian fashion which circumvents the decoupling between interleaved (red-black) diagonal grids discussed earlier.

Both convex and concave filters as well as total variation filters with and without the reaction term are compared in [44], and representative results can be summarized as follows. In Fig. 6, four selected magnifications of an unfiltered magnetic resonance image u_0 of the abdominal region are shown on the left. The image u_0 is filtered using the total variation penalty $\phi(s) = s$

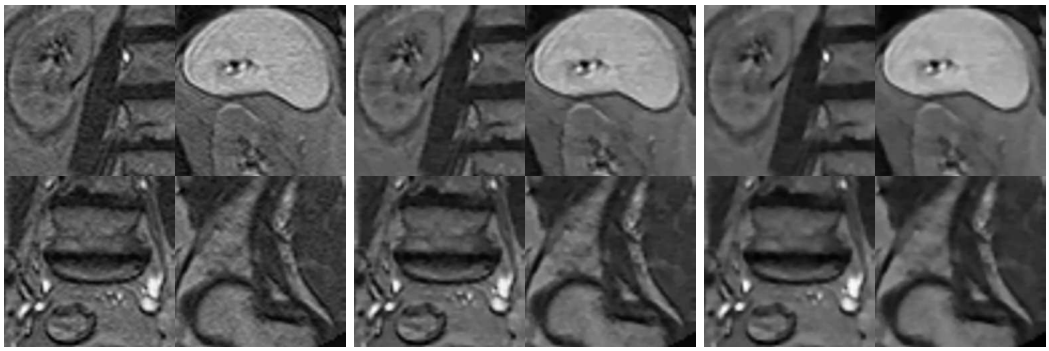

Figure 6: On the left are four selected magnifications of an unfiltered magnetic resonance image u_0 of the abdominal region. The image u_0 is filtered using the total variation penalty $\phi(s) = s$ and the edge-flat-grey penalty of (2.17), and the filtered results are shown respectively in the middle and on the right.

and the edge-flat-grey penalty of (2.17), and the results are shown respectively in the middle and on the right. In both cases (2.14) is minimized using the descent procedure (2.15) with $\mu > 0$. Note that the result with total variation filtering manifests an unnatural image flattening while the result with EFG filtering is smoother and yet preserves details more naturally. The tabulation of advantages and disadvantages found in [44] among the compared filters is shown in Table 1.

3 Dynamic Magnetic Resonance Imaging

3.1 Nonparametric Deconvolution Approaches [51]

While the problems discussed in the previous section are static in nature, the work of [51] involves analysis of spatiotemporal intensity data. Specifically, dynamic contrast enhanced magnetic resonance imaging involves to inject a bolus of contrast agent into a patient and to use rapid magnetic resonance imaging techniques to obtain a temporal sequence of images such as shown in Fig. 7, where the left and right images were measured, respectively, before and after

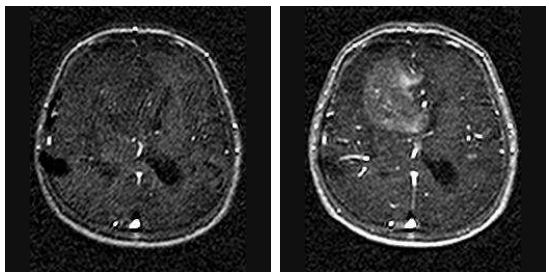

Figure 7: Magnetic resonance images taken from a series of images measured during the injection of a Gadolinium-DTPA based contrast agent. From left to right the images were measured, respectively, before and after the appearance of the contrast agent.

the appearance of the contrast agent. In this particular sequence of images, the contrast agent causes a local elevation in the otherwise rather uniform intensity, and the change in intensity improves image contrast. The degree of intensity change from a baseline to a contrast enhanced intensity is used to compute the local concentration of the contrast agent algebraically; see, e.g., [67]. Once the dynamic distributed concentration of contrast agent is determined, it is used to estimate variations in tissue transport properties, which in turn may reveal or better visualize pathology such as the brain tumor which is partially visible in Fig. 7.

A commonly used approach for estimating distributed transport properties is to model the

Filter	Advantages	Disadvantages
Median	Preserves stronger edges.	Changes the shapes of edges by saw-toothing or by smoothing. Smoothes some details.
BFB	Preserves image details. Can provide multiscale edge enhancement. Is a candidate for segmentation pre-conditioning.	Creates unnatural image flattening, though less so than PM and TV.
PM	Can enhance a targeted edge strength.	Enhances only a limited range of edge strengths and otherwise edges are either smoothed or staircased. Blurs details and strongly flattens images.
TV	Reduces noise while preserving details.	Staircases regions of gradual variation, and more so with a reaction term. Creates unnatural image flattening.
EFG	Preserves details and avoids staircasing. Is a good candidate for segmentation pre-conditioning.	Flattens images.
Gauss-TV	Preserves details and avoids staircasing. Preserves natural roundedness of image objects.	Partially preserves some noisy patterns.
Gaussian	Reduces noise.	Preserves some noisy patterns. Isotropic smoothing blurs details.

Table 1: Summary of filter results obtained in [44].

interaction between tracer and a voxel of tissue with a convolution:

$$C_{\mathrm{T}}(t) = \int_0^t K(t-s) C_{\mathrm{AIF}}(s) ds. \tag{3.1}$$

Here, C_{T} is the concentration of tracer within the selected tissue voxel T, C_{AIF} is the concentration of tracer entering the voxel, i.e., the arterial input function, and K is a convolution kernel representing the response of the tissue to an impulsive arterial input. Note that C_{AIF} is commonly assumed to be spatially invariant over a wide tissue region and it estimated by the tracer concentration within a nearby major artery. Thus, C_{AIF} is determined from intensities at an artery site while C_{T} is determined from intensities at the selected tissue site. Then the goal is to determine the convolution kernel K voxelwise and to represent its static properties by imaging. The question concerning what can be inferred from the convolution kernel K is a major topic of [49], but the following accepted parameters are derived in [49] on the basis of a revised theory: the volumetric flow rate per unit tissue volume, $\mathcal{F}_{\mathrm{T}} = K(0)$, the mean transit time, $\mathcal{T}_{\mathrm{T}} = \int_0^\infty K(t)/K(0) dt$, and the effective volume fraction, $\mathcal{V}_{\mathrm{T}} = \mathcal{T}_{\mathrm{T}} \mathcal{F}_{\mathrm{T}}$.

The problem of solving for the kernel K in (3.1), from given data C_{T} and C_{AIF}, is well known to be ill-posed; see [22] and the references cited therein. This ill-posedness is considered in the present context in [51] by supposing that the tracer is injected impulsively and that it travels through at least three major compartments: from the injection site through the right heart, from the right heart through the lungs to the left heart, and from the left heart to the tissue. When each of $n+1$ compartments is well mixed with the same compartment kernel $\nu e^{-\nu t}$, then the arterial input at the tissue site is given through the $(n+1)$-fold convolution of the unit kernel:

$$C_{\mathrm{AIF}}(t) = \delta(t) * [\nu e^{-\nu t}]_1 * \cdots * [\nu e^{-\nu t}]_{n+1} = \nu \frac{(\nu t)^n}{n!} e^{-\nu t}. \tag{3.2}$$

Since convolution is linear, it follows for C_{AIF} fixed according to (3.2) that the kernel K depends discontinuously on data C_{T} when a noisy disturbance N_ε of C_{T} can be found which generates an error E_ε in K where N_ε vanishes while E_ε diverges as ε vanishes. The following is proved in [51] and shows further that the deconvolution problem is progressively more sensitive to noise as the number of injection-to-tissue compartments increases and thereby increases the initial smoothness of C_{AIF}.

Theorem 2 *For each $n \in \boldsymbol{N}$ and for C_{AIF} given by (3.2) there exist functions N_ε and E_ε depending upon $\varepsilon > 0$ and satisfying $N_\varepsilon = E_\varepsilon * C_{\mathrm{AIF}}$ and*

$$\sup_{t\geq 0} |N_\varepsilon(t)| \leq c_1\varepsilon, \quad \sup_{t\geq 0} |E_\varepsilon(t)| \geq c_2\varepsilon^{-n} \tag{3.3}$$

for constants c_1 and c_2 which do not depend upon n or ε.

Since $K(t)$ represents the amount of tracer which has not yet cleared the tissue after an impulsive injection [49], the kernel is necessarily non-increasing and thus the solution to the deconvolution problem is naturally regularized according to the following constrained minimization:

$$\min_{K\in B} \|C_{\mathrm{T}} - K * C_{\mathrm{AIF}}\|_{L_2[0,T]} \qquad \text{subject to:} \quad K' \leq 0, \quad K \geq 0 \tag{3.4}$$

where B is an appropriate function class. Although a square-integrable, unbounded, decreasing kernel can satisfy the convolution equation $C_{\mathrm{T}} = K * C_{\mathrm{AIF}}$ for differentiable functions C_{AIF} and C_{T}, e.g., $K(t) = t^{-1/4}$ and C_{AIF} in (3.2), discretized data provide an *a priori* bound on the kernel. Specifically, it is assumed in [51] that the discrete data $\{t_i, C_{\mathrm{AIF}}(t_i)\}$ and $\{t_i, C_{\mathrm{T}}(t_i)\}$ are represented as continuous piecewise linear functions, and the following is proved to establish the resulting bound on K.

Theorem 3 *Assume that the data C_{T} and C_{AIF} are continuous, non-negative functions which are linear in each interval $[t_i, t_{i+1}]$, $i = 0, \ldots, N-2$, $t_i = iT/(N-1)$, and that these data vanish with positive slope at $t = t_0$. Let (K, λ, μ) be a solution to the optimality system for (3.4) for which $\mu \in \mathcal{C}^0[0,T]$, $\lambda \in \mathcal{C}^1(t_i, t_{i+1}) \cap \mathcal{C}^0[0,T]$, and $K \in \mathcal{C}^2(t_i, t_{i+1}) \cap L_2[0,T]$ hold for $i = 0, \ldots, N-2$. Then K is constant in each interval (t_i, t_{i+1}), non-increasing, and bounded in terms of the data values.*

It follows from this theorem that a kernel K so estimated has bounded variation on $[0,T]$. Thus, approximation schemes employing a finite dimensional set B in (3.4) are vulnerable to the *staircasing effect* which is well known for total variation regularization.

Specifically, both spline bases and exponential bases are considered in [51], and it is found that a monotonicity constrained spline basis can provide an excellent reconstruction of a piecewise constant kernel corresponding to a plug flow; however, a kernel with gradual variations corresponding to a mixing flow can be estimated with a sequence of stair-steps. On the other hand, a monotonicity constrained exponential basis resists staircasing since very many exponential functions are required to approximate a stair-step; thus, an exponential basis is less well suited for plug flow and better suited for a mixing flow.

Computational experiments in [51] reveal that both spline and exponential bases require further regularization. It is found that spline nodes are best distributed uniformly and the number of spline nodes is determined by an L-curve criterion in which the equation residual is balanced against the derivative of the kernel. Spline knots are chosen according to the spline smoothness desired. On the other hand, on the basis of the Müntz Theorem and computational experiments, the time scales of an exponential basis are chosen to be harmonically distributed, and the number of time scales is determined by an L-curve criterion in which the equation residual is balanced against the derivative of the kernel.

For both spline functions and exponential functions, the monotonicity constraint must be implemented in a discretized fashion, and experimentation with various candidates demonstrates

the best discretizations among those considered and reveals additionally that the monotonicity constraint is indeed active. The most natural condition for splines, which is sufficient but not necessary, is that the coefficients of canonical basis functions be monotone; see [51]. On the other hand, the standard condition for monotonicity of an exponential basis established in [19] is considerably generalized in [51]. Specifically, when the estimated kernel K takes the form:

$$K(t) = \sum_{m=1}^{M} k_m e^{-\lambda_m t} \tag{3.5}$$

it is guaranteed to be monotone when the coefficients k_m are non-negative, but in this case K is completely monotone and thus extremely smooth. A more general condition is given by:

$$\boldsymbol{k}^{\mathrm{T}}[\Lambda D_1^{-1} \cdots D_{M-1}^{-1}] \geq 0 \tag{3.6}$$

where $\boldsymbol{k}^{\mathrm{T}} = \langle k_1, \ldots, k_M \rangle$, $\Lambda = \mathrm{diag}\{\lambda_1, \ldots, \lambda_M\}$ and

$$D_m = \mathrm{tridiag}\left\{ \begin{bmatrix} -\Delta_{m+1}^1 & -\Delta_{m+2}^2 & \cdots & -\Delta_M^{M-m} & 0 & \cdots & 0 & - \\ \Delta_{m+1}^1 & \Delta_{m+2}^2 & \cdots & \Delta_M^{M-m} & 1 & \cdots & 1 & 1 \\ - & 0 & \cdots & 0 & 0 & \cdots & 0 & 0 \end{bmatrix}^{\mathrm{T}} \right\}, \quad \Delta_i^j = (\lambda_i - \lambda_j)^{-1}. \tag{3.7}$$

The following is proved in [51].

Theorem 4 *Assume that the values $\{\lambda_m\}_{m=1}^M$ are positive and distinct. Then under the condition (3.6), the function $K(t)$ in (3.5) is non-negative and non-increasing.*

The accuracy of spline and exponential bases is examined in detail in [51] in relation to known solutions, and the results are described above for plug flow and for mixing flow. On the other hand, results from applying these constrained bases to measured data are compared qualitatively in Fig. 8 with the result obtained from the standard truncated singular value decomposition (TSVD) approach [67]. The estimation from TSVD clearly manifests significant oscillations. Consistent with the ill-posedness of the deconvolution, all residuals $C_{\mathrm{T}} - K * C_{\mathrm{AIF}}$ are small, although the regularization present in all methods prevents to match the steep ascent in the data, which could otherwise be achieved with unconstrained and sufficient freedom in (3.4). The constrained splines estimation is evidently more accurate than the TSVD estimate, but the constrained exponentials estimate appears the most natural.

On the basis of these results and because exponential functions are widely regarded by practitioners to have a natural physiological basis, the constrained exponentials approach is applied to the dynamic contrast enhanced magnetic resonance imaging sequence of Fig. 7, and the pixelwise computed physiological parameters $\mathcal{V}_{\mathrm{T}}$, $\mathcal{F}_{\mathrm{T}}$ and $\mathcal{T}_{\mathrm{T}}$ are shown in the respective columns of Fig. 9 compared with results from the standard TSVD approach. The images in the top row of Fig. 9 were computed using the constrained exponentials approach while the images in the second row were computed using the standard TSVD approach. In all images, a cerebral tumor is evident in the upper portion of the images. Note that in spite of there being no explicit spatial coupling among the deconvolutions in either approach, the images manifest the following surprising spatial correlation. The images obtained by the constrained exponentials approach manifest a sharpness typical of images regularized through spatial total variation, while the images obtained by TSVD manifest a slight blur typical of images spatially regularized through Gaussian filtering. This apparent spatial correlation will be studied further in relation to the theory developed in [30].

3.2 Revision of the Theory of Tracer Transport [49]

The development of the kernel estimation techniques in [51] led to efforts to clarify precisely what can be determined from dynamic contrast enhanced magnetic resonance imaging data,

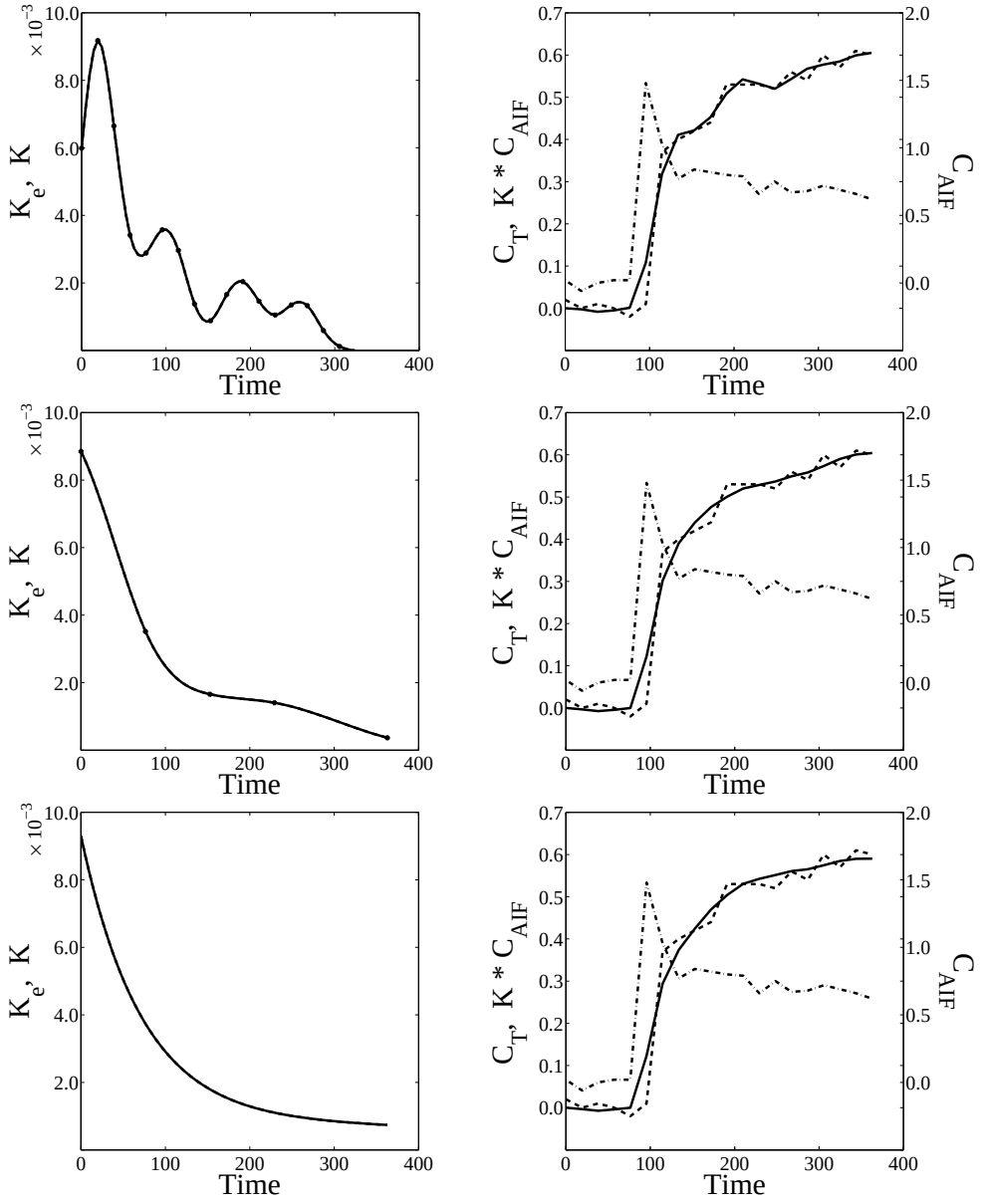

Figure 8: Results of solving (3.1) with TSVD, constrained splines, and constrained exponentials are shown respectively in rows 1 through 3. The solid curves in the left column are the kernel estimations. In the right column the dash-dotted curve is C_{AIF}, the dashed curve is C_{T}, and the solid curves are the convolutions $K * C_{\mathrm{AIF}}$.

and thus it was discovered in [49] that the foundational work of [83] on the theory of tracer transport requires revision. The need for revision can be seen readily by considering the simple compartmental examples of Fig. 10, in which the physiological mechanisms of interest in [83] are represented in Fig. 10b while the mathematical formulation appearing in that work applies to Fig. 10a. In both the examples of Fig. 10, a tissue region is divided into two compartments which are assumed to be well mixed and with constant volumes V_i. Tracer concentration in compartment i is denoted by C_i. Transport of a tracer into and out of the tissue region occurs only through concentration functions C_{AIF} and C_{VOF}, respectively, i.e., an arterial input function and a venous output function. The passive transport mechanisms of convection and diffusion are represented respectively by unidirectional and bidirectional transport paths and corresponding rate constants k_i or k_{ij} between compartments. When compartments 1 and 2 are regarded respectively as intravascular and extravascular spaces, Fig. 10b is clearly the more fitting description of perfusion and permeation in the tissue region. Specifically, perfusion

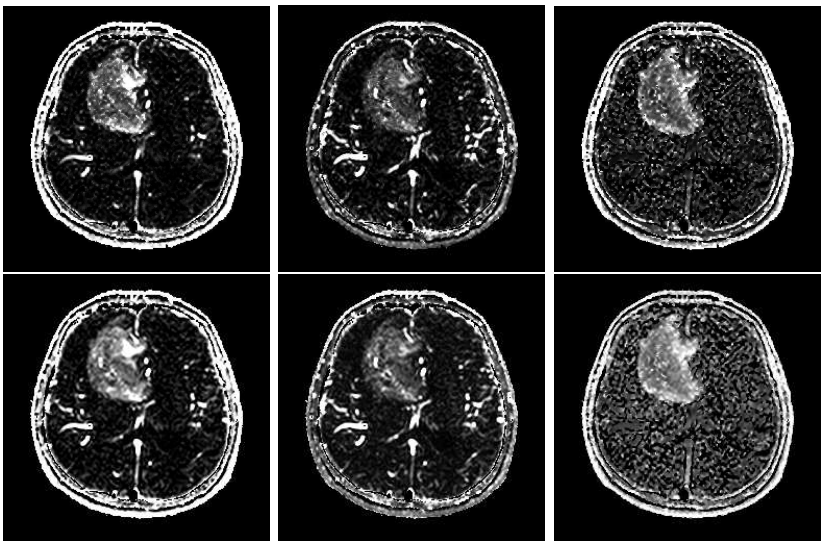

Figure 9: The pixelwise computed parameters, $\mathcal{V}_{\mathrm{T}}$, $\mathcal{F}_{\mathrm{T}}$ and $\mathcal{T}_{\mathrm{T}}$ were derived from the image sequence shown in Fig. 9 and are shown respectively in columns 1 through 3. Results for the constrained exponentials approach and the TSVD approach are shown respectively in the top and bottom rows.

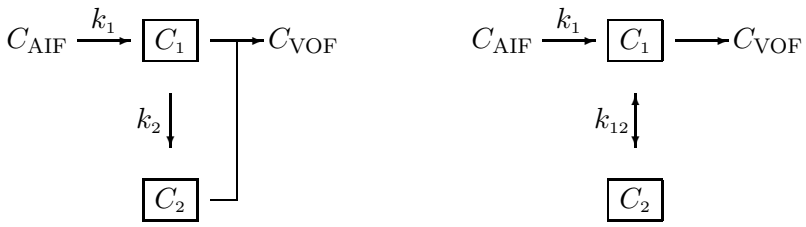

Figure 10: Compartment networks with (a) purely convective exchange shown on the left, and (b) convective and diffusive exchange shown on the right. The parameters in (3.8) may be chosen so that the respective residue functions are identical.

is unidirectional convection, being driven by a fixed pressure gradient, while permeation is bidirectional diffusion being driven by a varying concentration gradient. Thus, a permeable substance injected into either the intra- or extravascular space would diffuse into the opposite space where the concentration is lower. Such bidirectional transport is not permitted in Fig. 10a.

The differential formulation of transport for systems such as in Fig. 10 is given by:

$$V_i C_i' + k_i(C_i - C_{i-1}) = \sum_{j \neq i} k_{ij}(C_j - C_i) \quad \text{or} \quad V\boldsymbol{C}' = A\boldsymbol{C} + \boldsymbol{b}C_{\mathrm{AIF}} \tag{3.8}$$

where $\boldsymbol{C}$ is a vector of concentrations, V is a diagonal matrix of volumes, $\boldsymbol{b}$ is a vector whose nontrivial ith component is k_i when $i-1$ is out of range, and A is a matrix representing all other multiplications shown in the index formulation on the left in (3.8). For Fig. 10a the matrix A is lower triangular and for Fig. 10b the matrix A is full.

According to [83], if h_1 and h_2 are the distributions of tracer transit times through the intravascular and extravascular spaces respectively, and E is the fraction of tracer extracted from the intravascular space, then the distribution of tracer transit times through the tissue region is given by:

$$h(t) = (1 - E)h_1(t) + Eh_2(t) * h_1(t) \tag{3.9}$$

where $*$ denotes convolution. As seen in [49], the distribution of transit times for a given tissue region is the venous output function for that region resulting from an impulsive arterial input

function. From the explicit solution to (3.8),

$$\boldsymbol{C}(t) = \exp\left[V^{-1}At\right]\boldsymbol{C}(0) + \int_0^t \exp\left[V^{-1}A(t-s)\right]V^{-1}\boldsymbol{b}C_{\mathrm{AIF}}(s)ds. \tag{3.10}$$

it is seen that the diffusive connection between compartments 1 and 2 in Fig. 10b creates such a strong coupling between them that independent impulse responses cannot even be defined for these two compartments. However, impulse responses are readily defined for the compartments of Fig. 10a, and the solution (3.10) is readily shown to agree with (3.9).

Notice that the intra- and extravascular spaces may be arbitrarily finely compartmentalized, even represented by distributed parameter models, and yet so long as the two are in passive diffusive contact with one another, impulse responses can no more easily be defined for the two spaces than they can for the simple two-compartment model considered above. More serious still is the fact that one cannot determine by measurement of the impulse response of a tissue region whether that region is characterized by a model such as Fig. 10a or Fig. 10b. To see this, note that the solution to (3.8) for both of the cases Fig. 10a and Fig. 10b is a sum of two exponentials. Given those exponentials, it cannot be determined whether the system eigenvalues are those of the lower triangular matrix for Fig. 10a or of the full matrix for Fig. 10b. This last observation is a special case of the general non-identifiability result shown below in Theorem 5.

From (3.10) the average tissue concentration is given by $C_{\mathrm{T}} = \boldsymbol{e}^{\mathrm{T}}V\boldsymbol{C}/\boldsymbol{e}^{\mathrm{T}}V\boldsymbol{e}$, where $\boldsymbol{e}$ is a vector with all components equal to one. Under the assumption that the initial concentration in the tissue region is zero, C_{T} and C_{AIF} are related by the convolution in (3.1) where the kernel is given through (3.10) by $K(t) = \boldsymbol{e}^{\mathrm{T}}\exp[AV^{-1}t]\boldsymbol{b}/\boldsymbol{e}^{\mathrm{T}}V\boldsymbol{e}$ for an arbitrary number of compartments. Tissue transport states are associated with the *spectral* properties of the convolution kernel as follows on the basis of the detailed results shown in [49].

For pure convection the eigenvalues of AV^{-1} are clustered, and the representative kernel is a sum of Erlang distributions. In the ischemic limit that flow is limited to a narrow convective chain, an Erlang distribution leads to a step function representation of a plug flow. On the other hand, high vascularization increases the variance in the eigenvalue cluster. For pure streamline oriented diffusion, the eigenvalues of AV^{-1} are widely distributed, and the representative kernel is a sum of decaying exponential functions. In the limit of high diffusivity, all but one eigenvalue of AV^{-1} give negligibly transient dynamics and the smallest eigenvalue leads to a mono-exponential kernel. For pure permeation oriented diffusion, the eigenvalues of AV^{-1} are widely distributed and can easily be complex. Such eigenvalues make the representative kernel a sum of products of trigonometric and decaying exponential functions, which corresponds to recirculation of contrast agent through the tissue region.

On the basis of such results, a physiologically meaningful basis with which to represent the desired kernel might consist of the span of decaying exponential functions, products between polynomials and decaying exponentials, and products between trigonometric and decaying exponential functions. Ideally, when a kernel is estimated from the span of such functions, the weights of these different types of span elements might be correlated to the respective tissue transport states described above. However, the following theorem shows that a kernel which could correspond to any one of these states may be approximated arbitrarily well by a purely convective kernel, and thus these different tissue transport states cannot be decided on the basis of the kernel alone. In the following, the tissue region may be viewed as divided into M convective tubes, each containing N subregions. Note that the assumption $\int_0^\infty K(t)dt \leq 1$ in the following is natural since $\mathcal{V}_{\mathcal{T}}$ is the effective volume *fraction*.

Theorem 5 *Suppose that* $K(t) \in L_1[0,\infty)$ *is non-negative and non-increasing and satisfies* $\int_0^\infty K(t)dt \leq 1$*, and suppose that a constant* $\mathrm{vol}(\Omega)$ *is given. Then* K *can be approximated arbitrarily well in* $L_1[0,\infty)$ *for sufficiently large* N*,* M*,* $S = N \times (M+1)$ *by* $\boldsymbol{e}^{\mathrm{T}}\exp[AV^{-1}t]\boldsymbol{b}/\boldsymbol{e}^{\mathrm{T}}V\boldsymbol{e}$ *where* V *is a block diagonal matrix* $\mathrm{diag}\{V_mI\}_{m=0}^M$ *with* $N \times N$ *diagonal blocks* V_mI*,* $V_m > 0$*, satisfying* $\boldsymbol{e}^{\mathrm{T}}V\boldsymbol{e} = \mathrm{vol}(\Omega)$*,* A *is a block diagonal matrix* $\mathrm{diag}\{A_m\}_{m=0}^M$ *with* $N \times N$ *lower*

bidiagonal blocks $A_m = \text{tridiag}\{k_m, -k_m, 0\}$*,* $k_m > 0$*, and* $\boldsymbol{b}$ *is the concatenation* $\{k_m \boldsymbol{\epsilon}_1\}_{m=0}^{M}$ *of vectors* $k_m \boldsymbol{\epsilon}_1 \in \boldsymbol{R}^N$ *where* $\boldsymbol{\epsilon}_1 = \langle 1, 0, \ldots, 0 \rangle^{\mathrm{T}}$*.*

In [49] a revised theory of tracer transport is formulated in terms of a fully distributed convection-diffusion model. For this, let Ω be a given tissue region containing both intravascular and extravascular spaces. Let $\boldsymbol{v}$ be a vector field such that $\boldsymbol{v}$ has the same orientation as convection when convection is present and $[I - \boldsymbol{v}\boldsymbol{v}^{\mathrm{T}}]$ has the same orientation as permeation when permeation is present. Assume further that $\boldsymbol{v}$ is supported only in regions of convection or permeation, where $\boldsymbol{v}^{\mathrm{T}}\boldsymbol{v} = 1$ holds, and otherwise $\boldsymbol{v} = 0$. Let F (length/time) denote the mean fluid velocity supported only on regions of convection, where the measure of this support depends upon the extent of vascularization in Ω. Then the spatiotemporal distribution of contrast agent concentration C (mass/volume) is modeled by:

$$\partial_t C + \nabla \cdot (F\boldsymbol{v}C) = \nabla \cdot (\mathcal{D}(\boldsymbol{v})\nabla C), \qquad \mathcal{D}(\boldsymbol{v}) = D\boldsymbol{v}\boldsymbol{v}^{\mathrm{T}} + P[I - \boldsymbol{v}\boldsymbol{v}^{\mathrm{T}}] \tag{3.11}$$

where $\mathcal{D}$ is a diffusivity tensor which includes a convection oriented diffusivity D (area/time) and a permeation oriented diffusivity P. While D is convection oriented in the lumen, D is permeation orthogonal in a membrane. Similarly, P is permeation oriented in a membrane and convection orthogonal in the lumen. Furthermore, in a membrane $P = \mathcal{P}\tau$ depends upon a distributed permeability $\mathcal{P}$ (diffusivity/depth) and a distributed membrane thickness τ. In the interstitial space, $\boldsymbol{v} = 0$ holds and P is the local isotropic diffusivity. Naturally, when membranes are disrupted, the convective space must be enlarged from the lumen to include the portion of interstitial space in which flow is present. The diffusivity tensor $\mathcal{D}(\boldsymbol{v})$ may of course be generalized, but the diffusion mechanisms shown in (3.11) are those which have received the most attention in the literature [16]. The (contrast agent) influx and outflux portions of the boundary $\partial\Omega$ are the subsets where $F\boldsymbol{n}^{\mathrm{T}}\boldsymbol{v}C < \boldsymbol{n}^{\mathrm{T}}\mathcal{D}(\boldsymbol{v})\nabla C$ and $F\boldsymbol{n}^{\mathrm{T}}\boldsymbol{v}C > \boldsymbol{n}^{\mathrm{T}}\mathcal{D}(\boldsymbol{v})\nabla C$ hold, respectively, where $\boldsymbol{n}$ is the outward directed unit normal vector. The (fluid) inflow and outflow boundaries are the arterial inflow $F\boldsymbol{n}^{\mathrm{T}}\boldsymbol{v} < 0$ and venous outflow boundaries $F\boldsymbol{n}^{\mathrm{T}}\boldsymbol{v} > 0$, respectively. As found in [49], diffusive exchange between Ω and its surroundings must be assumed zero in order to define an impulse response for Ω, and under this assumption, the influx and outflux boundaries coincide with the inflow and outflow boundaries respective.

The tissue states described above are related as follows in [49] to the convection-diffusion model. First assume that transport is convection dominated. When the tissue is ischemic, F is supported on a smaller subset of Ω, and a concentration wave entering Ω remains more coherent during transit and exits with a very narrowly distributed transit time. In case of high vascularization, F is more widely supported in Ω, and a concentration wave entering Ω manifests more dispersion during transit and exits with a widely distributed, yet finite, transit time. Now assume that transport is not convection dominated so that flux into and out of Ω may occur by diffusion in addition to convection. In such cases, the mixing resulting from diffusion leads not only to considerable dispersion of entering concentration waves but the contrast agent clears from Ω only after infinite time as a result of upstream diffusion.

One approach to identify tissue parameters is to identify the coefficients in (3.11) from spatiotemporally distributed concentration data; see [11]. Alternatively, (3.11) may be integrated and a semigroup theory used in order to develop the convolution model (3.1) for a selected tissue region Ω. For this, the following assumptions are made. It is evident from solutions given in [49], that in order to avoid diffusive coupling between Ω and its surroundings and thereby isolate Ω for the desired model, *the concentration flux at the boundary of* Ω *must be assumed to be purely convective.* Further, it is assumed that *the fluid flow through every subset of* Ω *is balanced* so that $\int_{\partial D} F\boldsymbol{v}^{\mathrm{T}}\boldsymbol{n}d\boldsymbol{x} = 0$ holds for every $D \subseteq \Omega$. It is also assumed that *the parameters* F*,* $\boldsymbol{v}$*,* P*, and* D *in (3.11) are time-independent*, and thus the tissue exhibits *stationarity* in the sense of [82]. Finally, it is assumed that *the concentrations* C_{AIF} *and* C_{VOF} *are spatially constant along the inflow and outflow boundaries respectively.*

Thus, the Cauchy problem associated with (3.11) is given as follows. Let χ be the characteristic function vanishing outside a very narrow but smooth subset of Ω which borders on $\Gamma = \{\partial\Omega : F\boldsymbol{v}^{\mathrm{T}}\boldsymbol{n} < 0\}$ with $\int_\Omega \chi d\boldsymbol{x} = 1$. Also define $\boldsymbol{n}$ on the support of χ by its value at the nearest point on Γ, and note that $\boldsymbol{v}^{\mathrm{T}}\boldsymbol{n} < 0$ holds on a sufficiently narrow support of χ. Then for an arbitrary $t^* > 0$, let the Cauchy problem be formulated as:

$$\left\{ \begin{array}{rcl} C' & = & \mathcal{A}C + \mathcal{B}C_{\mathrm{AIF}}, \quad 0 \le t \le t^* \\ C(0) & = & C_0 \end{array} \right. \tag{3.12}$$

where $\mathcal{A}$ is defined by:

$$\begin{array}{rcl} \mathcal{A}C & = & \nabla \cdot (\mathcal{D}(\boldsymbol{v})\nabla C) - \nabla \cdot (F\boldsymbol{v}C) + F\boldsymbol{v}^{\mathrm{T}}\boldsymbol{n}\chi C \\ \mathrm{Dom}(\mathcal{A}) & = & \{C \in H^2(\Omega) : \boldsymbol{n}^{\mathrm{T}}\mathcal{D}(\boldsymbol{v})\nabla C = 0, \partial\Omega\} \end{array} \tag{3.13}$$

and $\mathcal{B}$ is defined by:

$$\mathcal{B}C = -F\boldsymbol{v}^{\mathrm{T}}\boldsymbol{n}\chi C. \tag{3.14}$$

When χ is interpreted as δ_Γ, then spatial integration of (3.12) and application of the Gauss Theorem to divergence terms shows that the term $F\boldsymbol{v}^{\mathrm{T}}\boldsymbol{n}(C - C_{\mathrm{AIF}})\chi$ in $\mathcal{A}C + \mathcal{B}C_{\mathrm{AIF}}$ creates an arterial input source C_{AIF} on Γ. The existence of the semigroup $S(t) = \exp[\mathcal{A}t]$ is guaranteed by Theorem 6 given below and proved in [49], and the counterpart to (3.10) in the distributed parameter setting is given by the following solution to the Cauchy problem (3.12):

$$C(t) = S(t)C_0 + \int_0^t S(t-s)\mathcal{B}C_{\mathrm{AIF}}(s)ds. \tag{3.15}$$

Theorem 6 *Assume that the operator $\mathcal{A}$ satisfies the uniform ellipticity condition $\theta\|\boldsymbol{x}\|^2 \le \boldsymbol{x}^{\mathrm{T}}\mathcal{D}\boldsymbol{x}, \forall \boldsymbol{x} \in \boldsymbol{R}^3$, that $D, P, F \in L_\infty(\Omega)$ and that $\partial\Omega$ is smooth. Then $\mathcal{A}$ generates a semigroup $S(t) \in \mathcal{C}([0,\infty), L_2(\Omega))$ and satisfies $\|S(t)\| \le e^{\omega t}$ where $\omega = \|F\|_\infty^2/(4\theta)$. Also, for every $C_{\mathrm{AIF}} \in L_2([0,t^*], L_2(\Omega))$, the unique weak solution to (3.12) is given by the mild solution in (3.15).*

The average tissue concentration is then given from (3.15) by $C_{\mathrm{T}} = \int_\Omega C(t)d\boldsymbol{x}/\mathrm{vol}(\Omega)$, and under the assumption that the initial concentration in Ω is zero, C_{T} and C_{AIF} are related by the convolution (3.1) with a kernel which is given through (3.15) for vanishing support of χ as the limit of kernels of the form $K(t) = \int_\Omega S(t)F|\boldsymbol{v}^{\mathrm{T}}\boldsymbol{n}|\chi d\boldsymbol{x}/\mathrm{vol}(\Omega)$. Thus, on the basis of (3.11), the convolution model (3.1) is obtained from the semigroup formulation and the solution (3.15) to the Cauchy problem (3.12). Then formulas for physiological parameters, such as those for $\mathcal{F}_{\mathrm{T}}$, $\mathcal{T}_{\mathrm{T}}$ and $\mathcal{V}_{\mathrm{T}}$ given in the discussion following (3.1), are derived by integration of (3.11) as shown in detail in [49].

4 Numerical and Computational Formulations for Early Vision

4.1 Magnetic Resonance Coil Sensitivity Estimation [48], [7], [8], [9]

To improve temporal resolution for the dynamic contrast enhanced magnetic resonance imaging examinations discussed above, acquisition can be accelerated by measuring in parallel with coils which under-sample in a complementary fashion. However, when images are so measured for the phantom object shown on the left in Fig. 12, the result for four parallel coils is shown in Fig. 11. Specifically, because of under-sampling, each image is aliased or folded. Because each coil has a nonuniform sensitivity, each unfolded image is modulated with a smooth and nonuniform illumination. To correct for these corruptions requires to estimate the coil sensitivities.

In general, it is required to estimate a coil sensitivity $\mathcal{C}$ in a global field of view within which tissues may move during a dynamic examination; see the globally estimated coil sensitivity in

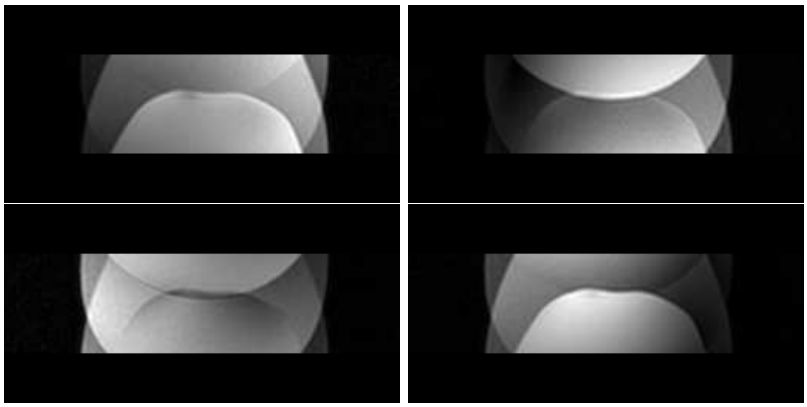

Figure 11: Aliased surface coil images $\mathcal{U}_{\mathrm{s}_i}$, $1 \leq i \leq 4$.

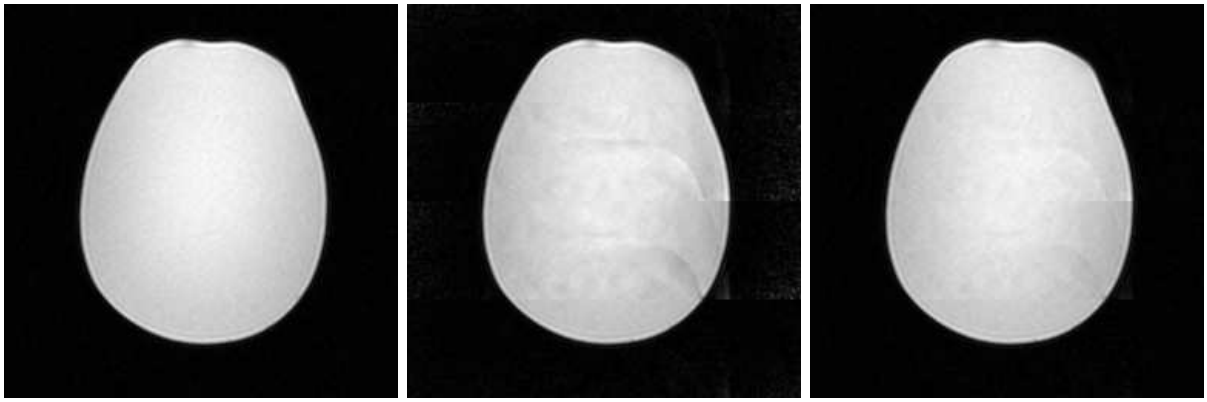

Figure 12: Shown at the left is a body coil image $\mathcal{U}_{\mathrm{b}}$. The images in the middle and at the right are reconstructions of $\mathcal{U}_{\mathrm{b}}$ from $\mathcal{U}_{\mathrm{s}_i}$ in Fig. 11, and from estimations of the sensitivities $\mathcal{C}_i$ obtained as follows. The sensitivities used for the reconstruction shown in the middle were obtained by solving (4.9) with $\nu = 2$ and using the factorization of the discrete biharmonic into discrete Laplacian factors. The sensitivities used for the reconstruction shown on the right were obtained by solving (4.15) with $\nu = 2$.

the image on the right of Fig. 13. In [48], the sensitivity is estimated as $\mathcal{C} \approx \mathcal{U}_{\mathrm{s}}/\mathcal{U}_{\mathrm{b}}$ from a single static pair of images, where $\mathcal{U}_{\mathrm{b}}$ is measured with a uniformly sensitive (body) coil and $\mathcal{U}_{\mathrm{s}}$ with the (surface) coil in question, as shown respectively in the first two images of Fig. 13. However, the measurements are corrupted by noise, the data are compactly supported and discontinuous at tissue boundaries, and yet the sensitivity is globally very smooth.

The estimation procedure proposed in [48] is to minimize a sum of a data residual and a high-order regularization suitable for exponentially varying sensitivities. Specifically, the complex-valued residual $\mathcal{U}_{\mathrm{b}}\mathcal{C} - \mathcal{U}_{\mathrm{s}}$ is partitioned into its real and imaginary parts and expressed as $m\varphi - r$ in terms of real-valued functions. Then the function φ is estimated on a rectangular domain $\Omega \subset \boldsymbol{R}^N$ as a minimizer for:

$$J(\varphi) = \int_\Omega |m\varphi - r|^2 d\boldsymbol{x} + \mu \sum_{|\alpha|=\nu} \frac{\nu!}{\alpha!} \int_\Omega |\partial^\alpha \varphi|^2 d\boldsymbol{x} \tag{4.1}$$

where a selected ν permits polynomial growth of degree $\nu - 1$ at the boundary $\partial\Omega$. Several other cost functionals are considered in [48], including those which attempt to remove the effect of the boundary and those involving high-order nonlinear penalties such as investigated in [56]; however, none of these functionals was found to perform better than (4.1). In the form (4.1), the problem is related to the surface estimation problem of early vision [70].

The high-order optimality system corresponding to (4.1), as well as other early vision problems considered below [45], is given by:

$$B(\varphi, \psi) = F(\psi), \quad \forall \psi \in H^\nu(\Omega) \tag{4.2}$$

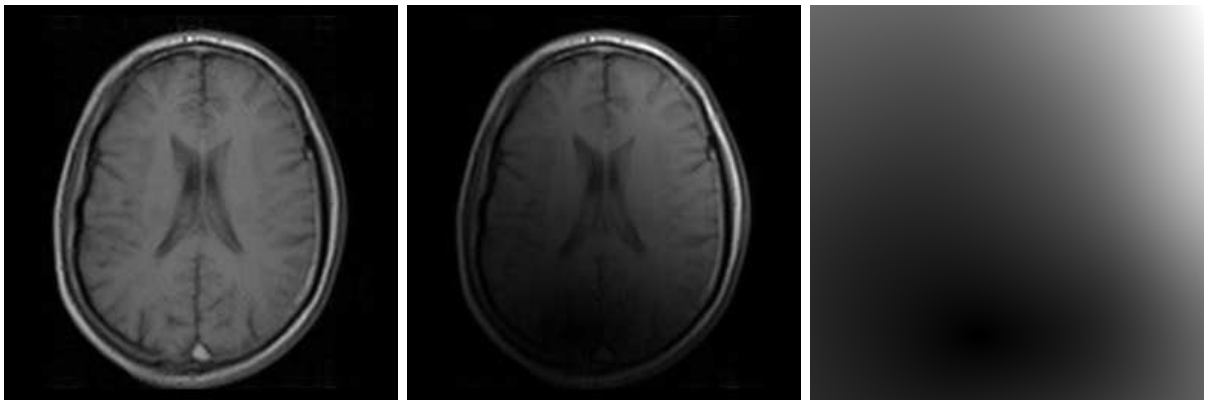

Figure 13: Shown at the left, in the middle, and at the right, respectively, are an image $\mathcal{U}_{\rm b}$ measured with a body coil, an image $\mathcal{U}_{\rm s}$ measured with a surface coil, and an estimated coil sensitivity $\mathcal{C}$.

in which B and F possess the structure:

$$B(\psi,\varphi) = B(\varphi,\psi) = B_\mu(\varphi,\psi) + B_0(\varphi,\psi) \tag{4.3}$$

$$F(\psi) = (f,\psi)_{L^2(\Omega)}, \quad f \in L^2(\Omega) \tag{4.4}$$

where a bilinear form B_0 involves no derivatives of its arguments but rather multiplication by intensity data,

$$B_0(\varphi,\psi) = (g\cdot\varphi, g\cdot\psi), \quad g \in L^\infty(\Omega), \quad \varphi,\psi \in H^\nu(\Omega) \tag{4.5}$$

and a bilinear form B_μ involves regularizing derivatives of its arguments. Under conditions on the data f and g [48], these forms are bounded:

$$|B(\varphi,\psi)| \le c\|\varphi\|_{H^\nu(\Omega)}\|\psi\|_{H^\nu(\Omega)}, \quad |F(\psi)| \le c\|\psi\|_{H^\nu(\Omega)} \tag{4.6}$$

and coercive:

$$|B(\varphi,\varphi)| \ge c\|\varphi\|^2_{H^\nu(\Omega)} \tag{4.7}$$

In the present context, B_μ satisfies $B_\mu(\varphi,\psi) = \mu\langle\varphi,\psi\rangle_{H^\nu(\Omega)}$ and $f = rm$ and $g = m$ hold. Furthermore, there exists an operator L satisfying:

$$(L\varphi,\psi)_{L^2(\Omega)} = (\varphi,L\psi)_{L^2(\Omega)} = B(\varphi,\psi), \quad \forall\varphi,\psi \in \mathrm{Dom}(L) = H^{2\nu}(\Omega), \quad L^* = L. \tag{4.8}$$

Several finite difference discretizations of this problem,

$$[\mu B_h + M]\bar{\Phi} = \bar{R} \tag{4.9}$$

are considered in [48], where the banded matrix μB_h is a discretization of B_μ, the diagonal matrix M is a discretization of B_0, the vector $\bar{R}$ is a discretization of F, and $\bar{\Phi}$ is a vector of grid values for φ. For instance, for $\nu = 2$ it is noted that a factorization of the discrete biharmonic into discrete Laplacian factors $B_h = \Delta_h\cdot\Delta_h$ is computationally convenient, and yet this expedient approximation implicitly employs Neumann boundary conditions which are conspicuously flattening at $\partial\Omega$ when the data are compactly supported. Furthermore, when the discrete biharmonic is not factorized and instead discretized in the standard way as shown on the right,

$$\begin{array}{ccccc} & & 1 & & \\ & 0 & -4 & 1 & \\ 0 & 0 & 7 & -4 & 1 \\ & 0 & -4 & 1 & \\ & & 1 & & \end{array} \qquad \begin{array}{ccccc} & & 1 & & \\ & 1 & -8 & 2 & \\ 0 & -4 & 19 & -8 & 1 \\ & 1 & -8 & 2 & \\ & & 1 & & \end{array} \qquad \begin{array}{ccccc} & & 1 & & \\ & 2 & -8 & 2 & \\ 1 & -8 & 20 & -8 & 1 \\ & 2 & -8 & 2 & \\ & & 1 & & \end{array} \tag{4.10}$$

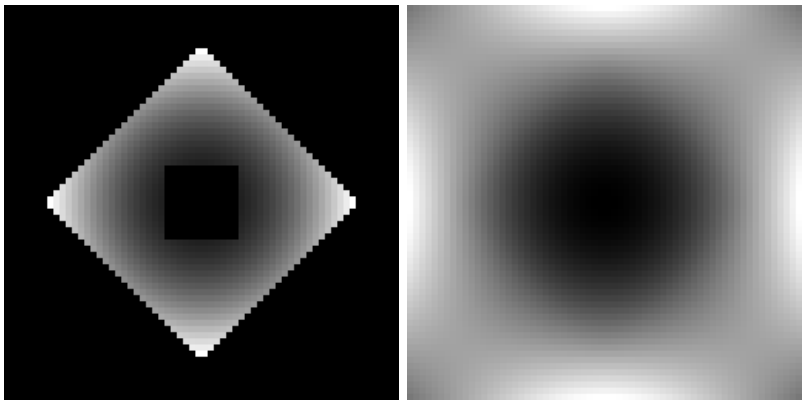

Figure 14: Shown on the left is r, a compactly supported restriction of a quadratic function, and m is the characteristic function for the support of r. The function shown on the right is obtained by solving (4.9) with B_h discretized according to (4.10).

along with natural modifications near the boundary as shown toward the left, the resulting estimate can manifest a conspicuously unnatural asymmetry as demonstrated in Fig. 14. In this example, the function r shown on the left in Fig. 14 is a compactly supported restriction of a quadratic function, and the function m is the characteristic function for the support of r. The function shown on the right in Fig. 14 is obtained by solving (4.9) with B_h discretized according to (4.10). Such results are improved in [48] with radially symmetric stencils, but the best results are achieved in [48] with finite element discretizations:

$$B(\varphi_h, \chi) = F(\chi), \quad \forall \chi \in S_h^\nu(\Omega) \tag{4.11}$$

where $S_h^\nu(\Omega) \subset C^{\nu-1}(\Omega) \cap H^\nu(\Omega)$ is the N-fold tensor product of B-splines of degree ν. According to Céa's Lemma [18], the solutions to (4.2) and (4.11) satisfy:

$$\|\varphi - \varphi_h\|_{H^\nu(\Omega)} \leq c \inf_{\chi \in S_h^\nu(\Omega)} \|\varphi - \chi\|_{H^\nu(\Omega)} \tag{4.12}$$

and convergence follows from the approximation property [2], which holds under minimal regularity $\varphi \in H^\nu(\Omega)$:

$$\inf_{\chi \in S_h^\nu(\Omega)} \|\varphi - \chi\|_{H^\nu(\Omega)} \leq c \sum_{|\alpha|=\nu} \sup_{|\boldsymbol{y}| \leq h} \int_\Omega |\partial^\alpha \varphi(\boldsymbol{x} - \boldsymbol{y}) - \partial^\alpha \varphi(\boldsymbol{x})|^2 d\boldsymbol{x} \to 0, \quad h \to 0. \tag{4.13}$$

In spite of the convergence guaranteed by the finite element method in the limit of grid refinement, it is shown in [48] that the practical implementation for regularized early vision problems suffers ameliorable flaws which can be understood with the 1D example of figure 15. In this example, the function r shown dotted in both plots of Fig. 15 is a compactly supported restriction of a quadratic function, and the function m is the characteristic function for the support of r. The solid curves shown in Fig. 15 are finite element solutions to (4.9) with $\nu = 4$ for μ/h^4 large and for for μ/h^4 small respectively. The example shows that when μ/h^4 is large, the estimation is naturally quite smoothed in relation to the data. To bring the estimation ever closer to the data requires that μ/h^4 be smaller, and in practice it is desirable for the method to provide consistent results in the limit that $\mu/h^4 \to 0$ as the signal-to-noise ratio becomes ever better. However, the numerical result here is quite aberrant as μ/h^4 becomes smaller. This behavior can be understood by showing that smooth trivial solutions do not satisfy the pure finite element discretization in (4.11) when the data are discontinuous.

This problem is corrected by using a lumping approach in which B_0 is diagonalized according to:

$$B_0(\chi_{\boldsymbol{i}}^\nu, \chi_{\boldsymbol{j}}^\nu) = (g \cdot \chi_{\boldsymbol{i}}^\nu, g \cdot \chi_{\boldsymbol{j}}^\nu)_{L^2(\Omega)} \to \delta_{\boldsymbol{ij}} (g_{\boldsymbol{i}-\frac{\nu}{2}} \cdot g_{\boldsymbol{i}-\frac{\nu}{2}}) \|\chi_{\boldsymbol{i}-\frac{\nu}{2}}^0\|_{L^2(\Omega)}^2. \tag{4.14}$$

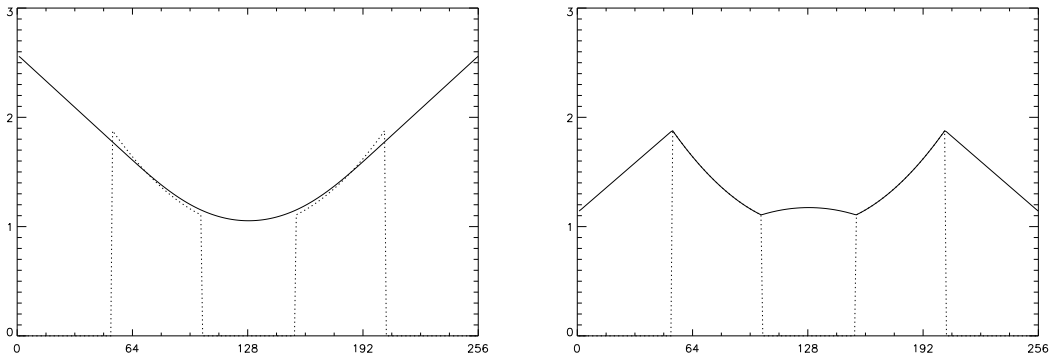

Figure 15: Shown dotted in both plots is r, a compactly supported restriction of a quadratic function, and m is the characteristic function for the support of r. The solid curves are finite element solutions to (4.9) with the case that μ/h^4 is large shown on the left, and the case that μ/h^4 is small shown on the right.

Here $g_{\boldsymbol{i}-\frac{\nu}{2}} = g(\mathbf{x}_{\boldsymbol{i}-\frac{\nu}{2}})$ where $\chi^\nu_{\boldsymbol{i}}$ peaks at $\boldsymbol{x} = \mathbf{x}_{\boldsymbol{i}-\frac{\nu}{2}}$ and $\{\chi^\nu_{\boldsymbol{i}}\}$ denotes the canonical basis of B-splines of degree ν for $S^\nu_h(\Omega)$ [40]. With the modification shown in (4.14), convergence in the limit of increasing data fidelity and vanishing regularization is obtained as explained in [48]. Furthermore, when the lumping in (4.14) is used, the grids can alternatively be taken to include the ghost cells as illustrated below in Fig. 16, the finite element coefficients $\Phi_{h,\boldsymbol{i}}$ can be taken as solution values $\Phi_{h,\boldsymbol{i}} = \varphi_h(\mathbf{x}_{\boldsymbol{i}-\frac{\nu}{2}})$ at basis function peaks, and the numerical solution is determined pointwise as the solution to:

$$\sum_{\mathbf{1}\le\boldsymbol{j}\le(2^p+\nu)\cdot\mathbf{1}} \left[B_\mu(\chi^\nu_{\boldsymbol{i}},\chi_{\boldsymbol{j}}) + B_0(\chi^0_{\boldsymbol{i}-\frac{\nu}{2}},\chi^0_{\boldsymbol{j}-\frac{\nu}{2}})\right]\Phi_{h,\boldsymbol{j}} = F(\chi^0_{\boldsymbol{i}-\frac{\nu}{2}}), \quad \mathbf{1}\le\boldsymbol{i}\le(2^p+\nu)\cdot\mathbf{1} \tag{4.15}$$

where $B_0(\chi^0_{\boldsymbol{i}-\frac{\nu}{2}},\chi^0_{\boldsymbol{j}-\frac{\nu}{2}}) = g(\mathbf{x}_{\boldsymbol{i}-\frac{\nu}{2}})\cdot g(\mathbf{x}_{\boldsymbol{i}-\frac{\nu}{2}})\|\chi^0_{\boldsymbol{i}-\frac{\nu}{2}}\|^2_{L^2(\Omega)}$ and $F(\chi^0_{\boldsymbol{i}-\frac{\nu}{2}}) = f(\mathbf{x}_{\boldsymbol{i}-\frac{\nu}{2}})\|\chi^0_{\boldsymbol{i}-\frac{\nu}{2}}\|_{L^2(\Omega)}$ follow from (4.5) and (4.4) with piecewise constant g and f extended by zero outside Ω. The system in (4.15) is characterized by the following as proved in [48].

Theorem 7 *Suppose the date $g = m$ are supported at least on a collection of adjacent cells with centroids $\{\mathbf{x}_\kappa : \kappa_1 \le \kappa \le \kappa_1+\nu\}$. Then the coefficient matrix of (4.15) is symmetric and positive definite.*

The four images $\{\mathcal{U}_{\mathrm{s}_i}\}_{i=1}^4$ shown in figure 11 are used together with the respective coil sensitivities $\{\mathcal{C}_i\}_{i=1}^4$ to estimate an unaliased image $\mathcal{U}^*$ according to:

$$\mathcal{U}_{\mathrm{s}_i}(x,y) = \sum_{j=1}^4 \mathcal{C}_i(x,y+j\Delta y)\mathcal{U}^*(x,y+j\Delta y), \qquad 1\le i\le 4 \tag{4.16}$$

where Δy is the height of the folded images. Solving these systems for each (x,y) provides the so-called sensitivity encoded or SENSE reconstructed image $\mathcal{U}^*$ [71].

Figure 12 now demonstrates the effect of the coil sensitivity estimation on the SENSE reconstruction. The SENSE reconstruction shown in the middle in Fig. 12 was obtained from coil sensitivities estimated by solving (4.9) with $\nu = 2$ and using the factorization of the discrete biharmonic into discrete Laplacian factors $B_h = \Delta_h\cdot\Delta_h$. The SENSE reconstruction to the right in Fig. 12 was obtained from coil sensitivities estimated by solving (4.15) for $\nu = 2$. Note in the middle image of Fig. 12 the ghost outlines of spuriously unfolded image boundaries resulting from coil sensitivity estimation insufficiencies. On the other hand, the image on the right in Fig. 12 suffers much less so from such ghostings, even with $\nu = 2$. These techniques have been applied in medical contexts and further details on the applications are found in [7], [8] and [9].

A procedure currently under investigation, a generalization of that reported in [24], is to reconstruct the image $\mathcal{U}^*$ from images $\{\mathcal{U}_{\mathrm{s}_i}\}_{i=1}^n$ such as those in Fig. 11 without having references

images such as shown in Fig. 13. Thus, the image $\mathcal{U}^*$ and the sensitivities $\{\mathcal{C}_i\}_{i=1}^n$ are estimated simultaneously by minimizing the following cost:

$$J(\mathcal{U}^*, \mathcal{C}_1, \ldots, \mathcal{C}_n) = \sum_{i=1}^{n} \int_\Omega |K * (\mathcal{C}_i \mathcal{U}^*) - \mathcal{U}_{\mathrm{s}_i}|^2 d\boldsymbol{x} + \mu \sum_{i=1}^{n} \sum_{|\alpha|=\nu} \frac{\nu!}{\alpha!} \int_\Omega |\partial^\alpha \mathcal{C}_i|^2 d\boldsymbol{x} + \int_\Omega \phi(|\mathcal{U}^*|^2) d\boldsymbol{x}. \tag{4.17}$$

Here, convolution with the kernel K represents, e.g., an operation such as shown on the right side of (4.16) corresponding to a standard scanning method. On the other hand, choosing a kernel K which makes the estimation in (4.17) particularly effective will suggest a scanning technique for the respective coils.

4.2 Geometric Multigrid for Early Vision [50]

The surface estimation problem discussed above is also a model problem for the wider class of early vision problems such as those involving optical flow or image registration discussed below, and rapid computational methods are required in order that the associated optimality systems may be solved practically in a medical context. These optimality systems are Neumann problems of potentially high-order and their natural boundary conditions may be expediently simplified at the expense of corrupting an otherwise natural solution as demonstrated in [48] and [50]. Because the application of algebraic multigrid is usually constrained by an M-matrix condition which does not hold for discretizations of high-order problems, a geometric multigrid framework is developed in [50] for the efficient solution of the optimality systems; see also [55].

It is shown in [50] for the surface estimation problem that the convergence criteria of [34] are met. This convergence framework requires to establish an approximation property and a smoothing property. The approximation property is fulfilled through the Galerkin formalism, and the smoothing property is fulfilled by a symmetric Gauss-Seidel relaxation.

For the Galerkin formalism, conditions of the previous subsection are used together with the following. In addition to the approximation property (4.13), $S_h^\nu(\Omega)$ also satisfies [2]:

$$\inf_{\chi \in S_h^\nu(\Omega)} \|\varphi - \chi\|_{H^\nu(\Omega)} \leq c h^\nu \|\varphi\|_{H^{2\nu}(\Omega)}, \quad \forall \varphi \in H^{2\nu}(\Omega) \tag{4.18}$$

and the inverse property [2]:

$$\|\chi\|_{H^\nu(\Omega)} \leq c_2 h^{-\nu} \|\chi\|_{L^2(\Omega)}, \quad \forall \chi \in S_h^\nu(\Omega). \tag{4.19}$$

The convergence given by (4.12) and (4.13) is improved with the higher-order rate,

$$\|\varphi - \varphi_h\|_{H^\nu(\Omega)} \leq c h^\nu \|\varphi\|_{H^{2\nu}(\Omega)} \tag{4.20}$$

provided a higher-order regularity for the solution φ to (4.2) is established:

$$\|\varphi\|_{H^{2\nu}} \leq c \|f\|_{L^2(\Omega)} \leq c \|m\|_{L^\infty(\Omega)} \|r\|_{L^2(\Omega)}. \tag{4.21}$$

Since the data in B_0 are not necessarily smooth and Ω is a rectangular domain, the standard assumptions on the smoothness of coefficients and of the domain boundary do not apply in the present context, und therefore the following is proved in [50].

Theorem 8 *The solution φ to (4.2) satisfies $\varphi \in H^{2\nu}(\Omega)$ and (4.21).*

The multigrid strategy employed in [50] is built upon a set of nested subspaces based upon nested grids which can be described as follows. The nested grids range from the coarsest at level $l = 0$ to the finest at $l = l_{\max}$. The grid at level l consists of cells having unit aspect ratio and width h_l where the cell widths satisfy the following on adjacent levels:

$$h_l \leq 2 h_{l+1} \tag{4.22}$$

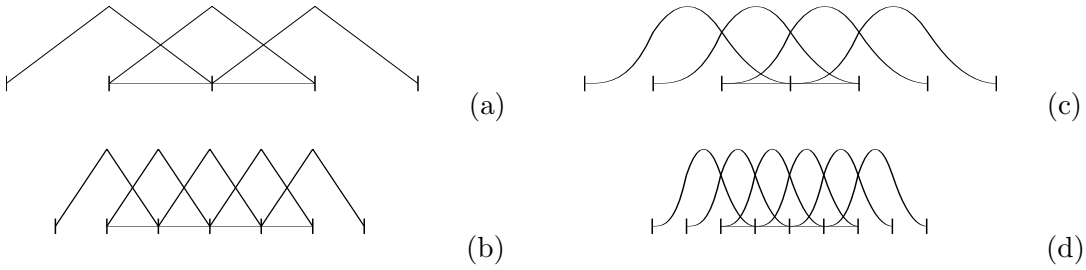

Figure 16: Examples of one-dimensional nested grids: (a) $\nu = 1$, $l = 0$, (b) $\nu = 1$, $l = 1$, (c) $\nu = 2$, $l = 0$, and (d) $\nu = 2$, $l = 1$. Vertical line segments denote cell boundaries. The horizontal line segments represent actual grid cells within $\Omega = (0, 1)$, and cells outside Ω are ghost cells.

and h_0 is large enough that the linear system on level $l = 0$ can easily be solved directly. The spline bases for $S_l^\nu(\Omega) = S_{h_l}^\nu(\Omega)$ are illustrated in Fig. 16 along with their corresponding nested grids for $N = 1$, $\nu = 1, 2$, $l = 0$ and $l = 1$. Note the ghost cells shown outside Ω in Fig. 16 and see also the discussion of grids in relation to the lumping shown in (4.15).

As with (4.8) there exists an operator L_l such that:

$$(L_l\chi, \psi)_{L^2(\Omega)} = B(\chi, \psi), \quad \forall \chi, \psi \in S_l^\nu(\Omega). \tag{4.23}$$

Defining the projection operator $P_l : L^2(\Omega) \to S_l^\nu(\Omega)$ and $f_l = P_l f$ allows (4.11) to be expressed as:

$$L_l\varphi_l = f_l, \quad \text{where} \quad L_h\varphi_h = f_h, \quad l = l_{\max}. \tag{4.24}$$

If I_{l-1} denotes the injection operator from $(S_{l-1}^\nu(\Omega), \|\cdot\|_{L^2(\Omega)})$ into $(S_l^\nu(\Omega), \|\cdot\|_{L^2(\Omega)})$, then the variational problems on adjacent levels are related according to:

$$L_{l-1} = I_{l-1}^* L_l I_{l-1}. \tag{4.25}$$

To realize these relations in terms of basis function coefficients Φ_l for functions $\varphi_l \in S_l^\nu(\Omega)$ instead of on the operator level above, let $\boldsymbol{R}_l$ denote the Euclidean space of coefficients equipped with the norm $[X_l] = [X_l, X_l]^{\frac{1}{2}}$ where $[X_l, Y_l] = h_l^N \sum_{\boldsymbol{i},\boldsymbol{j}} X_{l,\boldsymbol{i}} Y_{l,\boldsymbol{j}}$. Then let K_l denote the bijective mapping from $(\boldsymbol{R}_l, [\cdot])$ to $(S_l^\nu(\Omega), \|\cdot\|_{L^2(\Omega)})$ so that $\varphi_l = K_l\Phi_l$. These norms satisfy [2]:

$$c_1[\Phi] \le \|K_l\Phi\|_{L^2(\Omega)} \le c_2[\Phi], \quad \forall \Phi \in \boldsymbol{R}_l. \tag{4.26}$$

Thus, for a given basis $\{\chi_{\boldsymbol{i}}^\nu\}$ of $S_l^\nu(\Omega)$, the coefficient matrix representations of the operators L_l are given by:

$$A_{l,\boldsymbol{ij}} = (L_l\chi_{\boldsymbol{i}}^\nu, \chi_{\boldsymbol{j}}^\nu)_{L^2(\Omega)}. \tag{4.27}$$

Through the coefficient representations $A_l = K_l^* L_l K_l$ and $f_l = K_l F_l$, the problem (4.24) takes the form:

$$A_l\Phi_l = F_l, \quad \text{where} \quad A_h\Phi_h = F_h, \quad l = l_{\max}. \tag{4.28}$$

Then the variational problems on adjacent levels are related on the coefficient spaces $\boldsymbol{R}_l$ according to the following counterpart to (4.25):

$$A_{l-1} = R_l^{l-1} A_l E_{l-1}^l \tag{4.29}$$

where $E_{l-1}^l : \boldsymbol{R}_{l-1} \to \boldsymbol{R}_l$ and $R_l^{l-1} : \boldsymbol{R}_l \to \boldsymbol{R}_{l-1}$ are the canonical expansion and restriction operators satisfying:

$$I_{l-1}K_{l-1} = K_l E_{l-1}^l, \quad R_l^{l-1} = (E_{l-1}^l)^*. \tag{4.30}$$

From (4.7) it follows that the symmetric matrices A_l of (4.27) are positive definite. The principal ingredients of the multigrid strategy are thus given by (4.29) and (4.30) and the following symmetric Gauss-Seidel iteration:

$$\Phi_l^{k+1} = S_l\Phi_l^k + W_l^{-1}F_l, \quad S_l = I - W_l^{-1}A_l. \tag{4.31}$$

Here W_l is given by:

$$W_l = (\mathcal{D}_l + \mathcal{L}_l)\mathcal{D}_l^{-1}(\mathcal{D}_l + \mathcal{L}_l^{\mathrm{T}}) = A_l + \mathcal{L}_l\mathcal{D}_l^{-1}\mathcal{L}_l^{\mathrm{T}}, \quad W_l = W_l^{\mathrm{T}} \tag{4.32}$$

for diagonal, strictly lower triangular and strictly upper triangular parts of A_l given by the respective terms in the sum $A_l = \mathcal{D}_l + \mathcal{L}_l + \mathcal{L}_l^{\mathrm{T}}$. In [50] it is shown that the following hold:

$$0 < [A_l\Phi, \Phi] \leq [W_l\Phi, \Phi], \quad \forall \Phi \in \boldsymbol{R}_l, \quad \text{and} \quad [W_l] \leq \theta[A_l] \tag{4.33}$$

where $\theta = \theta(\|m\|_{L^\infty(\Omega)}, \mu, N, \nu)$.

With the above constructions, a two-grid cycle is defined by:

$$M_l^{\mathrm{TGC}}(\sigma) = S_l^\sigma[I - E_{l-1}^l A_{l-1}^{-1} R_l^{l-1} A_l] S_l^\sigma \tag{4.34}$$

which is symmetric as σ_1 pre-smoothing steps $\hat{S}_l$ and σ_2 post-smoothing S_l steps are used, where:

$$\sigma = \sigma_1 = \sigma_2, \quad \text{and} \quad \hat{S}_l = S_l. \tag{4.35}$$

Then, a symmetric multigrid cycle is defined by:

$$M_l^{\mathrm{MGC}}(\sigma, \tau) = M_l^{\mathrm{TGC}}(\sigma) + S_l^\sigma E_{l-1}^l [M_{l-1}^{\mathrm{MGC}}(\sigma, \tau)]^\tau A_{l-1}^{-1} R_l^{l-1} A_l S_l^\sigma. \tag{4.36}$$

The convergence framework in [34] requires to establish an approximation property and a smoothing property, which are given respectively as follows in [50] based upon [34].

Theorem 9 *Under the conditions (4.3), (4.8), (4.6), (4.19), (4.20), (4.22), (4.26), (4.27), (4.30), (4.29), (4.32), (4.33), (4.35), it follows that:*

$$0 \leq A_l^{-1} - E_{l-1}^l A_{l-1}^{-1} R_l^{l-1} \leq \theta W_l^{-1}. \tag{4.37}$$

Theorem 10 *Under the assumptions of Theorem 9, the smoother S_l, written in the form $X_l = I - A_l^{1/2} S_l A_l^{-1/2} = A_l^{1/2} W_l^{-1} A_l^{1/2}$, satisfies:*

$$0 \leq (I - X_l)^\sigma X_l (I - X_l)^\sigma \leq \eta(\sigma) I \tag{4.38}$$

where $\eta(\sigma) = \sigma^\sigma/(1+\sigma)^{(1+\sigma)}$ satisfies $\lim_{\sigma\to\infty} \eta(\sigma) = 0$.

These results are combined in [50] based upon [34] to give the following two-grid and multigrid convergence.

Theorem 11 *Under the assumptions of Theorem 9, the two grid cycle satisfies:*

$$[A_l^{1/2} M_l^{\mathrm{TGC}}(\sigma) A_l^{-1/2}] \leq \theta\eta(\sigma). \tag{4.39}$$

Theorem 12 *Under the assumptions of Theorem 9, the multigrid iteration matrices $M_l^V(\sigma) = M_l^{\mathrm{MGC}}(\sigma, 1)$ and $M_l^W(\sigma) = M_l^{\mathrm{MGC}}(\sigma, 2)$ satisfy the following:*

$$[A_l^{1/2} M_l^V(\sigma) A_l^{-1/2}] \leq \frac{\theta}{\theta + \sigma}, \qquad [A_l^{1/2} M_l^W(\sigma) A_l^{-1/2}] \leq \frac{\sqrt{\theta}}{\sqrt{\theta} + \sigma}. \tag{4.40}$$

When lumping is implemented as shown in (4.14) and (4.15), L_h is decomposed according to $L_h = L_h^\mu + L_h^0$ where L_h^μ and L_h^0 are defined by:

$$(L_h^\mu \chi_{\boldsymbol{i}}^\nu, \chi_{\boldsymbol{j}}^\nu)_{L^2(\Omega)} = \mu\langle \chi_{\boldsymbol{i}}^\nu, \chi_{\boldsymbol{j}}^\nu \rangle_{H^\nu(\Omega)}, \quad (L_h^0 \chi_{\boldsymbol{i}}^\nu, \chi_{\boldsymbol{j}}^\nu)_{L^2(\Omega)} \to \delta_{\boldsymbol{ij}} m_{\boldsymbol{i}-\frac{\nu}{2}}^2 \|\chi_{\boldsymbol{i}-\frac{\nu}{2}}^0\|_{L^2(\Omega)}^2. \tag{4.41}$$

Then L_l^μ and L_l^0 are defined through (4.25) for $0 \leq l \leq l_{\max}$ and $A_l = A_l^\mu + A_l^0$ is similarly decomposed according to (4.29) for $0 \leq l \leq l_{\max}$. Also, A_l^μ and A_l^0 are conveniently computed according to (4.27) and (4.29) respectively:

$$A_{l,\boldsymbol{ij}}^\mu = \mu\langle \chi_{\boldsymbol{i}}, \chi_{\boldsymbol{j}} \rangle_{H^\nu(\Omega)}, \quad A_{l-1}^0 = R_l^{l-1} A_l^0 E_{l-1}^l. \tag{4.42}$$

The relations (4.29) and (4.30) hold in any case for A_l, A_l^μ and A_l^0. Then, (4.33) is established in [50] for the lumped formulation.

A multi-colored ordering of unknowns is used in [50] in order to facilitate vectorization of the relaxation scheme on image processing systems such as IDL. Specifically, with a stencil diameter of $(2\nu+1)$, the set of all stencil centers, separated from one another in any of N coordinate directions by exactly ν stencil centers, contains stencils which do not weight any other stencil centers in the set. The stencil centers within such a set are painted with the same color, ordered along coordinate directions within that color, and then ordered sequentially among the colors. With such a multi-colored ordering, (4.31) can be implemented by performing a Jacobi iteration on same-colored cells while looping in one direction and then the other over the colors:

$$\begin{array}{c} \text{for } c = 1, \ldots, (\nu+1)^N \text{ and then } c = (\nu+1)^N, \ldots, 1 \\ \Phi_l^c \leftarrow \Phi_l^c - [\mathcal{D}_l^{-1}(A_l\Phi_l - F_l)]^c \end{array} \tag{4.43}$$

Thus, same-colored cells may be updated simultaneously. Similarly, the known stencil diameter can also be used to advantage to vectorize the computation of elements of the coarse grid matrix according to (4.42) [50].

The Gauss-Seidel iteration of (4.31) or (4.43) is guaranteed by Theorem 7 to converge, but Theorem 7 is only valid in exact arithmetic, and the iteration is found in [50] to diverge because of treatable floating point errors. For example, the Galerkin multiplication (4.29) can produce a representation of a coarse grid matrix which is so poor as not even to be positive definite. This problem can be corrected as shown in (4.42) by using the Galerkin multiplication only to compute the zero-order terms and otherwise to compute the elements of the coarse grid matrix exactly by scalar products directly. Errors can still emerge in (4.42) because of the inaccurate computation of scalar products in matrix-vector multiplications, and these can be corrected by using a specialized command such as `total` in IDL. Further floating point errors can still prevent the Gauss-Seidel iteration from converging when the problem is very high-order and the coefficient matrix is *stored* with sufficient inaccuracy that it fails to be positive definite. This problem can be avoided by choosing parameters so that grouped products can be stored exactly with the selected precision.

The finite element approach explained above is compared in [50] with a multigrid framework based upon finite differences as follows. For a given ν let the expansion operator map values from cell centers in a coarse grid to cell centers in a fine grid in such a way that the transformation is exact for polynomials of degree ν. While it is natural to consider constructing the restriction operator similarly, the canonical transpose in (4.30) is much more accurate and maintains symmetry. With this finite difference approach to the inter-grid transfer operators, the discrete coarse grid operator is defined by the Galerkin multiplication (4.29). In spite of the apparent naturalness of this construction, it is found to be inadequate on the basis of the example of Fig. 17, which is specified in detail in [50]. Here, finite difference and finite element approximations to an exact polynomial solution to (4.15) are shown respectively on the left and on the right, where the image on the right is visibly indistinguishable from the exact solution. The accuracy of the finite element solution is conspicuously higher.

While Dirichlet or other low-order boundary conditions are often expediently implemented because of theoretical or computational ease [54], it is shown in [50] not only that computed solutions with Neumann boundary conditions are clearly more natural in appearance but also that the multigrid reduction factor is more favorable for Neumann than for Dirichlet boundary conditions for $\nu > 1$. Further experimentation proposes on the basis of the multigrid reduction factor that the regularization lie in the range $0 \leq \log(\mu/h^{2\nu}) \leq 5$ and that an optional relaxation parameter lie in the range $1 \leq \omega \leq 2$. Furthermore, data support is found to have a very strong effect on the multigrid reduction factor and on the computational results. The multigrid reduction factors reflect that for regularization smaller than $\log(\mu/h^{2\nu}) = 0$ the coefficient matrix of (4.15) rapidly becomes indefinite when the data are compactly supported or else ever more nearly the identity when the data are fully supported. These differences are also revealed

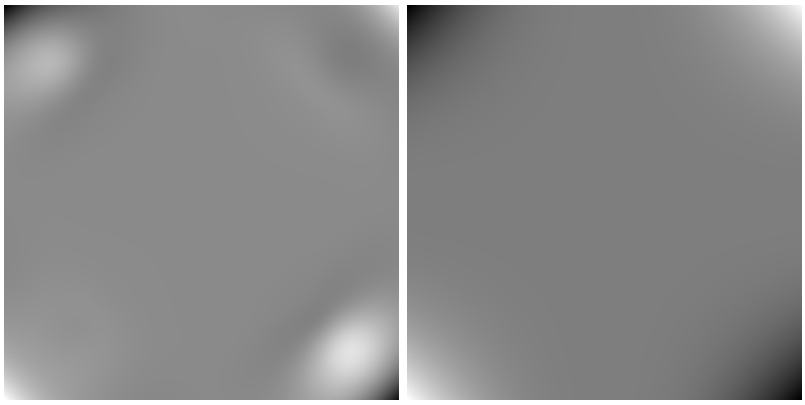

Figure 17: Finite difference and finite element approximations to an exact polynomial solution to (4.15) are shown respectively on the left and on the right, where the image on the right is visibly indistinguishable from the exact solution.

in the computational results of Fig. 18. Here, phantom data similar to those shown in Fig. 13

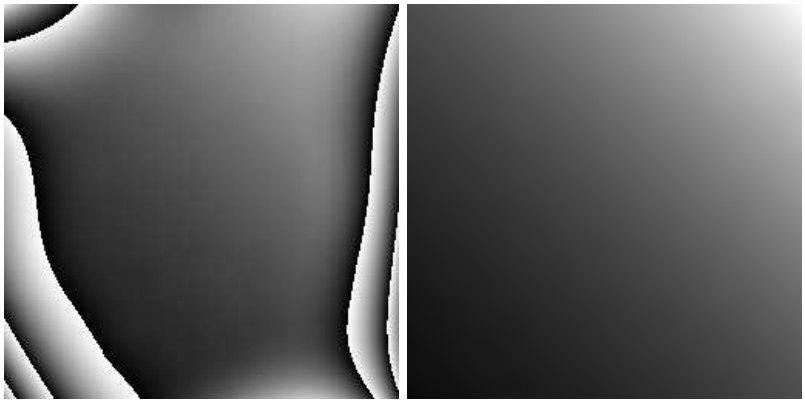

Figure 18: With phantom data such as shown in Fig. 13, (4.15) is solved approximately with $\nu = 4$ using compactly supported data to obtain the image on the left and fully supported data to obtain the image on the right, where the image on the right is indistinguishable from the exact solution.

are used to solve (4.15) with $\nu = 4$ until differences between successive iterates are not reduced further. The images shown on the left and on the right are obtained respectively with compactly and fully supported data, and the image shown on the right is visibly indistinguishable from the exact solution. Note that the values of the image on the left are wrapped through the interval $[0, 1]$ several times, and the accuracy of the solution with fully supported data is conspicuously higher. As can be seen from convergence histories shown in Fig. 19, solutions obtained for $\nu < 4$ manifest better convergence, but compactly supported data always compromise the multigrid reduction factor unless sufficiently high regularization is chosen. It is seen in [50] that solutions obtained with $\nu = 3$ are the most accurate and efficiently computed for exact solutions possessing exponential growth.

5 Image Registration and Interpolation

5.1 Generalized Rigid and Generalized Affine Methods [52], [47], [45], [13]

The methods of the previous subsection are adapted in [45] for what is defined here as generalized rigid and generalized affine image registration and interpolation. These notions are defined precisely as follows. Following the illustration in Fig. 20 for 2D images, let two given images I_0 and I_1 be situated respectively on the front face $\Omega_0 = (0, 1)^N$ and back face

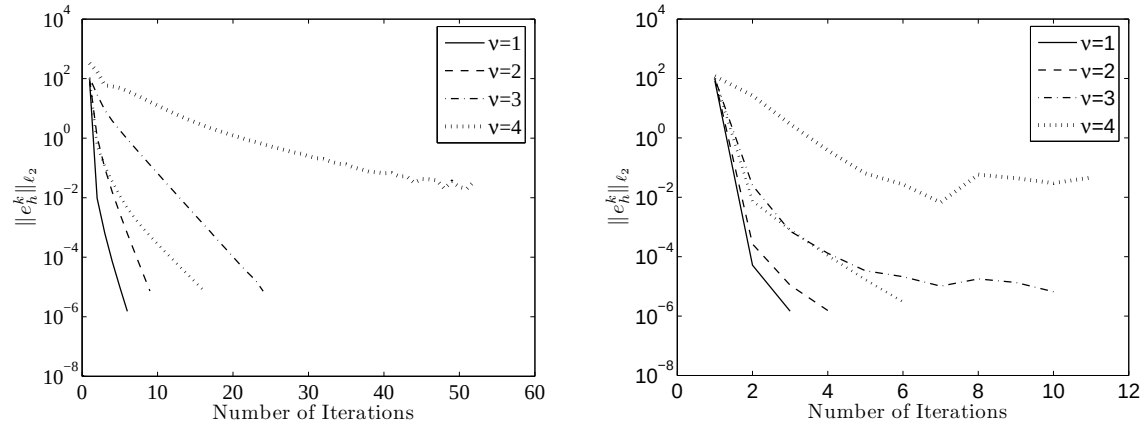

Figure 19: For $\nu = 1$ to $\nu = 4$, convergence histories of $e_h^k = \Phi_h^k - \Phi_h^{k-1}$ are shown for $M_l^V(1)$ iterations on the left and $M_l^W(1)$ iterations on the right. The steeper dotted curves are the convergence histories for $\nu = 4$ and fully supported data, while the other curves are convergence histories for compactly supported data.

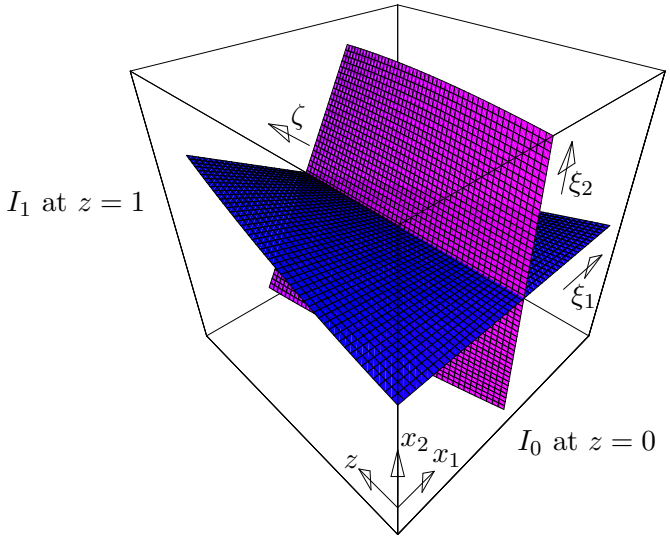

Figure 20: The domain Q with 2D images I_0 and I_1 on the front and back faces Ω_0 and Ω_1, respectively. Curvilinear coordinates are defined to be constant on trajectories connecting like points in I_0 and I_1.

$\Omega_0 = (0,1)^N$ of a box $Q = (0,1)^{N+1}$ with generic cross section $\Omega = (0,1)^N$. Define Cartesian coordinates $(\boldsymbol{x}, z)$, $\boldsymbol{x} \in \Omega$, $z \in (0,1)$, and curvilinear coordinates $(\boldsymbol{\xi}, \zeta)$ so that $\boldsymbol{\xi}$ is constant along trajectories through Q that connect like points in I_0 and I_1, and $\zeta = z$. Also, suppose that $\boldsymbol{x} = \boldsymbol{\xi}$ holds in Ω_0 and therefore the displacement vector within Q is $\boldsymbol{d} = \boldsymbol{x} - \boldsymbol{\xi}$. Similarly define $\boldsymbol{\eta}$ and $\boldsymbol{y}$ so that $\boldsymbol{\eta}$ is constant along trajectories together with $\boldsymbol{\xi}$, and $\boldsymbol{y} = \boldsymbol{\eta}$ holds in Ω_1. Further, a trajectory tangent is given by $(\boldsymbol{u}, 1)$ in terms of the optical flow defined as $\boldsymbol{u} = \boldsymbol{x}_\zeta$.

In order to permit purely rigid or purely affine transformations, trajectories are allowed to move out of the box Q. Let the subsets of Ω_0 and Ω_1 with respect to which trajectories extend completely through the full depth of Q be denoted respectively by Ω_0^{c} and Ω_1^{c}. Their respective complements are denoted by $\Omega_0^{\mathrm{i}} = \Omega_0 \backslash \Omega_0^{\mathrm{c}}$ and $\Omega_1^{\mathrm{i}} = \Omega_1 \backslash \Omega_1^{\mathrm{c}}$. Then an image similarity measure, which does not favor a given image order, is given for finite displacements $\boldsymbol{d}(\boldsymbol{\xi}, 1) = \boldsymbol{x}(\boldsymbol{\xi}, 1) - \boldsymbol{\xi}$ by the following sum of squared intensity differences:

$$\begin{aligned} \mathcal{S}_{\mathrm{fd}}(\boldsymbol{x}) &= \int_{\Omega_0^{\mathrm{c}}} [I_0(\boldsymbol{\xi}) - I_1(\boldsymbol{x}(\boldsymbol{\xi}))]^2 \, d\boldsymbol{\xi} + \int_{\Omega_0^{\mathrm{i}}} [I_0(\boldsymbol{\xi}) - I_1^{\infty}]^2 \, d\boldsymbol{\xi} \qquad (\boldsymbol{x}(\boldsymbol{\xi}) = \boldsymbol{x}(\boldsymbol{\xi}, 1)) \\ &+ \int_{\Omega_1^{\mathrm{c}}} [I_0(\boldsymbol{y}(\boldsymbol{\eta})) - I_1(\boldsymbol{\eta})]^2 \, d\boldsymbol{\eta} + \int_{\Omega_1^{\mathrm{i}}} [I_0^{\infty} - I_1(\boldsymbol{\eta})]^2 \, d\boldsymbol{\eta} \qquad (\boldsymbol{y}(\boldsymbol{\eta}) = \boldsymbol{y}(\boldsymbol{\eta}, 0)) \end{aligned} \tag{5.1}$$

where I_0^∞ and I_1^∞ are the *background* intensities respectively of I_0 and I_1. These background intensities are used as though the sides $\Gamma = \partial Q \backslash \{\Omega_0 \cup \Omega_1\}$ of the box Q were not present and the trajectories impinging upon Γ from Ω_1 or Ω_0 would respectively be connected with I_0 and I_1 continued in $\boldsymbol{R}^N$ by their background intensities. A similarity measure which involves infinitesimal instead of finite displacements is obtained by replacing intensity differences in (5.1) with corresponding ζ-integrals of $[dI/d\zeta]^2$ and by applying the optical flow equation [41], $dI/d\zeta(\boldsymbol{x}(\boldsymbol{\xi},\zeta),\zeta) = \nabla_{\boldsymbol{x}} I \cdot \boldsymbol{x}_\zeta + I_\zeta = \nabla_{\boldsymbol{x}} I \cdot \boldsymbol{u} + I_z$, in (5.1) to obtain:

$$\mathcal{S}_{\rm of}(I,\boldsymbol{u}) = \int_Q [\nabla_{\boldsymbol{x}} I \cdot \boldsymbol{u} + I_z]^2 \, d\boldsymbol{x}dz \tag{5.2}$$

which has an integrand involving purely local information throughout Q. In other words, (5.2) gives a convenient *Eulerian* (local) counterpart to the *Lagrangian* (trajectory following) form appearing in (5.1). It also differs from (5.1) by not including the transformation Jacobian $1/\det[\nabla_{\boldsymbol{\xi}}\boldsymbol{x}]$, and this difference leads to the appearance of metric terms in one formulation and not the other. Furthermore, since the Lagrangian integrals of $[dI/d\zeta]^2$ suggested above are constrained by boundary conditions on ∂Q [45], these must be transformed to their Eulerian counterparts as follows [52]:

$$I = I_0 \text{ on } \Omega_0, \qquad I = I_1 \text{ on } \Omega_1 \tag{5.3}$$

and [45]:

$$I = I_1^\infty \text{ on } \Gamma^+, \quad I = I_0^\infty \text{ on } \Gamma^- \tag{5.4}$$

where inflow and outflow boundaries are defined respectively by $\Gamma^- = \{(\boldsymbol{x},z) \in \Gamma : \boldsymbol{u}\cdot\boldsymbol{n} < 0\}$ and $\Gamma^+ = \{(\boldsymbol{x},z) \in \Gamma : \boldsymbol{u}\cdot\boldsymbol{n} > 0\}$. Thus, an image similarity measure without intensity scaling is given for optical flow by (5.2) under the constraints (5.3) and (5.4).

Image registration is achieved by means of finite displacements by minimizing:

$$J_{\rm fd}(\boldsymbol{x}) = \mathcal{S}_{\rm fd}(\boldsymbol{x}) + \mathcal{R}_{\rm fd}(\boldsymbol{x}) \tag{5.5}$$

where the similarity measure $\mathcal{S}_{\rm fd}$ is given in (5.1) with the notations $\boldsymbol{x}(\boldsymbol{\xi})$ and $\boldsymbol{y}(\boldsymbol{\eta})$ used in the context of finite displacements since the alternative notations $\boldsymbol{x}(\boldsymbol{\xi},1)$ and $\boldsymbol{y}(\boldsymbol{\eta},0)$ refer to trajectories. Also, the regularity measure $\mathcal{R}_{\rm fd}$ is defined by:

$$\mathcal{R}_{\rm fd}(\boldsymbol{x}) = \mu \sum_{|\alpha|=2} \frac{2!}{\alpha!} \int_{\Omega_0^{\rm c}} |\partial_{\boldsymbol{\xi}}^\alpha \boldsymbol{x}|^2 d\boldsymbol{\xi}. \tag{5.6}$$

The second-order regularity measure $\mathcal{R}_{\rm fd}$ under natural boundary conditions provides generalized affine registration since $J_{\rm fd}$ vanishes for images related by an affine transformation. As shown in [52], generalized rigid registration is ruled out for finite displacements since linearized elastic potential energy does not select rigid transformations preferentially and nonlinearized elastic potential energy is computationally intractable.

Image registration and interpolation are achieved by means of optical flow by minimizing [52]:

$$J_{{\rm of},i}(I,\boldsymbol{u}) = \mathcal{S}_{\rm of}(I,\boldsymbol{u}) + \mathcal{R}_{{\rm of},i}(\boldsymbol{u}), \quad i = 1,2 \tag{5.7}$$

subject to (5.3) and (5.4), where the similarity measure $\mathcal{S}_{\rm of}$ is given in (5.2). Under natural boundary conditions the regularity measure $\mathcal{R}_{{\rm of},i}$ can be defined as:

$$\mathcal{R}_{{\rm of},1}(\boldsymbol{u}) = \int_Q \left[\phi(|\nabla \boldsymbol{u}^{\rm T} + \nabla \boldsymbol{u}|^2) + \gamma |\boldsymbol{u}_z|^2\right] d\boldsymbol{x}dz. \tag{5.8}$$

for generalized rigid registration, as shown in [52], and as:

$$\mathcal{R}_{{\rm of},2}(\boldsymbol{u}) = \int_Q \left[\mu \sum_{\substack{|\alpha|=2 \\ \alpha_{N+1}=0}} \frac{2!}{\alpha!} |\partial_{\boldsymbol{x}}^\alpha \boldsymbol{u}|^2 + \gamma |\boldsymbol{u}_z|^2 \right] d\boldsymbol{x}dz \tag{5.9}$$

for generalized affine registration, as shown in [45]. Specifically, $J_{\mathrm{of},1}$ vanishes for images related by a rigid transformation and $J_{\mathrm{of},2}$ vanishes for images related by an affine transformation. Here, $|\nabla \boldsymbol{u}|^2 = \nabla \boldsymbol{u} : \nabla \boldsymbol{u}$ and : denotes a componentwise matrix scalar product. Also $\phi(s) = \sqrt{s}$ for total variation regularization which is appropriate for object excision, and $\phi(s) = s$ for Gaussian regularization which is appropriate for smoother regularizations [52]. Trajectories through the domain Q are defined by integrating the optical flow under boundary conditions, i.e., by solving:

$$\boldsymbol{x}(\boldsymbol{\xi}, \zeta) = \boldsymbol{\xi} + \int_0^\zeta \boldsymbol{u}(\boldsymbol{x}(\boldsymbol{\xi}, \rho), \rho) d\rho, \quad \boldsymbol{\xi} \in \Omega_0, \quad \zeta \in [0, 1] \tag{5.10}$$

and

$$\boldsymbol{y}(\boldsymbol{\eta}, \zeta) = \boldsymbol{\eta} + \int_\zeta^1 \boldsymbol{u}(\boldsymbol{y}(\boldsymbol{\eta}, \rho), \rho) d\rho, \quad \boldsymbol{\eta} \in \Omega_1, \quad \zeta \in [0, 1]. \tag{5.11}$$

A registration is given by the coordinate transformation $\boldsymbol{x}(\boldsymbol{\xi}, 1)$ and by the inverse transformation $\boldsymbol{y}(\boldsymbol{\eta}, 0)$. The given images I_0 and I_1 are interpolated by the intensity I.

As explained in [52], computational experiments indicate that in practice the optical flow can as well be chosen to be autonomous. On the other hand, the example shown in Fig. 21 and explained in detail in [45] shows that there is indeed a theoretical difference between the

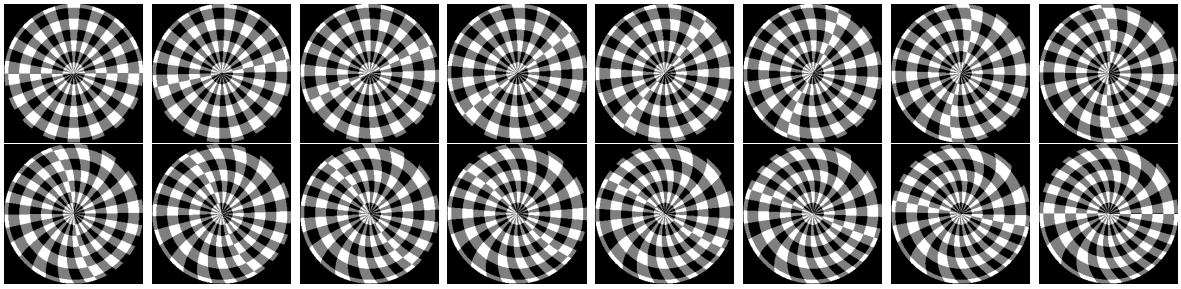

Figure 21: The two given images I_0 and I_1 are shown in the upper left and in the lower right. The sequence of images, read from left to right and from top to bottom, has been determined by minimizing $J_{\mathrm{of},1}$.

autonomous and non-autonomous cases of $\gamma = \infty$ and $\gamma < \infty$ respectively. Specifically, The sequence of images shown in Fig. 21 has been determined by minimizing $J_{\mathrm{of},1}$ for $\gamma < \infty$ while no such result is possible with $\gamma = \infty$. Nevertheless, it is found in practice that the optical flow can as well be chosen to be autonomous, $\boldsymbol{u}_z = 0$, and autonomous flows are the focus for the computational examples.

The cost J_{fd} is stationary in the displacement when $\boldsymbol{x}$ satisfies:

$$0 = \frac{1}{2} \frac{\delta J_{\mathrm{fd}}}{\delta \boldsymbol{x}}(\boldsymbol{x}, \bar{\boldsymbol{x}}) = B_{\mathrm{fd}}(\boldsymbol{x}, \bar{\boldsymbol{x}}) - F_{\mathrm{fd}}(\boldsymbol{x}, \bar{\boldsymbol{x}}), \quad \forall \bar{x} \in H^2(\Omega, \boldsymbol{R}^N) \tag{5.12}$$

where B_{fd} and F_{fd} are defined by:

$$B_{\mathrm{fd}}(\boldsymbol{x}, \bar{\boldsymbol{x}}) = \mu \sum_{|\alpha|=2} \frac{2!}{\alpha!} \int_{\Omega_0} [\partial_{\boldsymbol{\xi}}^\alpha \boldsymbol{x}] \cdot [\partial_{\boldsymbol{\xi}}^\alpha \bar{\boldsymbol{x}}] d\boldsymbol{\xi} \tag{5.13}$$

$$\begin{aligned} F_{\mathrm{fd}}(\boldsymbol{x}, \bar{\boldsymbol{x}}) &= \int_{\Omega_0^c} [I_0(\boldsymbol{\xi}) - I_1(\boldsymbol{x}(\boldsymbol{\xi}))] \nabla_{\boldsymbol{x}} I_1(\boldsymbol{x}(\boldsymbol{\xi}))^{\mathrm{T}} \bar{\boldsymbol{x}}(\boldsymbol{\xi}) d\boldsymbol{\xi} \\ &+ \int_{\Omega_1^c} [I_0(\boldsymbol{y}(\boldsymbol{\eta})) - I_1(\boldsymbol{\eta})] \nabla_{\boldsymbol{y}} I_0(\boldsymbol{y}(\boldsymbol{\eta}))^{\mathrm{T}} \nabla_{\boldsymbol{\eta}} \boldsymbol{y}(\boldsymbol{\eta}) \bar{\boldsymbol{x}}(\boldsymbol{y}(\boldsymbol{\eta})) d\boldsymbol{\eta}. \end{aligned} \tag{5.14}$$

In [45], (5.12) is solved by the following quasi-Newton iteration:

$$\left\{ \begin{array}{rcl} D_{\mathrm{fd}}(\boldsymbol{dx}_k, \boldsymbol{x}_k, \bar{\boldsymbol{x}}) &=& -\left[B_{\mathrm{fd}}(\boldsymbol{x}_k, \bar{\boldsymbol{x}}) - F_{\mathrm{fd}}(\boldsymbol{x}_k, \bar{\boldsymbol{x}})\right], \quad \forall \bar{\boldsymbol{x}} \in H^2(\Omega_0, \boldsymbol{R}^N) \\ \boldsymbol{x}_{k+1} &=& \boldsymbol{x}_k + \theta \boldsymbol{dx}_k \end{array} \right. \qquad k = 0, 1, 2, \ldots \tag{5.15}$$

where:

$$D_{\mathrm{fd}}(\boldsymbol{dx}_k, \boldsymbol{x}_k, \bar{\boldsymbol{x}}) = B_{\mathrm{fd}}(\boldsymbol{dx}_k, \bar{\boldsymbol{x}}) + \int_{\Omega_0^{\mathrm{c}}} [\nabla_{\boldsymbol{x}} I_1(\boldsymbol{x}_k(\boldsymbol{\xi})) \cdot \boldsymbol{dx}_k(\boldsymbol{\xi})][\nabla_{\boldsymbol{x}} I_1(\boldsymbol{x}_k(\boldsymbol{\xi})) \cdot \bar{\boldsymbol{x}}(\boldsymbol{\xi})] d\boldsymbol{\xi} \tag{5.16}$$

and θ is chosen by a line search to minimize $\mathcal{S}_{\mathrm{fd}}$ [36]. Note that no additional boundary conditions are imposed by restricting the domain of the forms B_{fd}, F_{fd} and D_{fd}, and thus natural boundary conditions hold. The following solvability of (5.15) for fixed k is established in [45].

Theorem 13 *For $\boldsymbol{x}_k \in H^2(\Omega_0, \boldsymbol{R}^N)$ and $\boldsymbol{y}_k \in H^2(\Omega_1, \boldsymbol{R}^N)$ suppose $\boldsymbol{x}_k = \boldsymbol{y}_k^{-1}$ on $\Omega_0^{\mathrm{c}} = \Omega_0 \cap \boldsymbol{y}_k(\Omega_1)$ and $\boldsymbol{y}_k = \boldsymbol{x}_k^{-1}$ on $\Omega_1^{\mathrm{c}} = \Omega_1 \cap \boldsymbol{x}_k(\Omega_0)$. Suppose that for every $\boldsymbol{c} \in \boldsymbol{R}^N$ and for every matrix $W \in \boldsymbol{R}^{N \times N}$ the image $I_1 \in W^{1,\infty}(\Omega_1, \boldsymbol{R})$ satisfies:*

$$\int_{\Omega_0^{\mathrm{c}}} |\nabla_{\boldsymbol{x}} I_1(\boldsymbol{x}_k(\boldsymbol{\xi})) \cdot (\boldsymbol{c} + W\boldsymbol{\xi})|^2 d\boldsymbol{\xi} > 0, \tag{5.17}$$

unless $\boldsymbol{c} = 0$ and $W = 0$ hold. Then there exists a unique $\boldsymbol{dx}_k \in H^2(\Omega_0, \boldsymbol{R}^N)$ such that (5.15) holds.

The cost $J_{\mathrm{of},1}$ is stationary in the intensity I for fixed $\boldsymbol{u}$ when I satisfies the following in terms of quantities defined below in a Lagrangian frame [52]:

$$I(\boldsymbol{x}(\boldsymbol{\xi}, \zeta), \zeta) = \begin{cases} I_0(\boldsymbol{\xi})[1 - U(\boldsymbol{\xi}, \zeta, 1)] + I_1(\boldsymbol{x}(\boldsymbol{\xi}, 1)) U(\boldsymbol{\xi}, \zeta, 1), & \boldsymbol{\xi} \in \Omega_0^{\mathrm{c}} \\ I_0(\boldsymbol{\xi})[1 - U(\boldsymbol{\xi}, \zeta, \acute{\zeta})] + I_1^{\infty} U(\boldsymbol{\xi}, \zeta, \acute{\zeta}), & \boldsymbol{x}(\boldsymbol{\xi}, \acute{\zeta}) \in \Gamma, \quad \boldsymbol{\xi} \in \Omega_0^{\mathrm{i}} \end{cases} \tag{5.18}$$

$$I(\boldsymbol{y}(\boldsymbol{\eta}, \zeta), \zeta) = \begin{cases} I_1(\boldsymbol{\eta})[1 - V(\boldsymbol{\eta}, 0, \zeta)] + I_0(\boldsymbol{y}(\boldsymbol{\eta}, 0)) V(\boldsymbol{\eta}, 0, \zeta), & \boldsymbol{\eta} \in \Omega_1^{\mathrm{c}} \\ I_1(\boldsymbol{\eta})[1 - V(\boldsymbol{\eta}, \grave{\zeta}, \zeta)] + I_0^{\infty} V(\boldsymbol{\eta}, \grave{\zeta}, \zeta), & \boldsymbol{y}(\boldsymbol{\eta}, \grave{\zeta}) \in \Gamma, \quad \boldsymbol{\eta} \in \Omega_1^{\mathrm{i}}. \end{cases} \tag{5.19}$$

The parameters $\acute{\zeta}$ and $\grave{\zeta}$ denote the ζ coordinates at which trajectories emanating respectively from Ω_0^{i} and Ω_1^{i} meet Γ. Also, U and V are defined by:

$$U(\boldsymbol{\xi}, \zeta, \acute{\zeta}) = \frac{\tilde{U}(\boldsymbol{\xi}, \zeta) - \tilde{U}(\boldsymbol{\xi}, 0)}{\tilde{U}(\boldsymbol{\xi}, \acute{\zeta}) - \tilde{U}(\boldsymbol{\xi}, 0)}, \qquad \tilde{U}(\boldsymbol{\xi}, \zeta) = \int_{\zeta_0}^{\zeta} \exp\left[- \int_{\zeta_0}^{\varrho} \nabla \cdot \boldsymbol{u}(\boldsymbol{x}(\boldsymbol{\xi}, \rho), \rho) d\rho \right] d\varrho, \tag{5.20}$$

for $\boldsymbol{\xi} \in \Omega_0$, $\zeta \in [0, \acute{\zeta}]$, and arbitrary $\zeta_0 \in [0, \acute{\zeta}]$, and:

$$V(\boldsymbol{\eta}, \grave{\zeta}, \zeta) = \frac{\tilde{V}(\boldsymbol{\eta}, 1) - \tilde{V}(\boldsymbol{\eta}, \zeta)}{\tilde{V}(\boldsymbol{\eta}, 1) - \tilde{V}(\boldsymbol{\eta}, \grave{\zeta})}, \qquad \tilde{V}(\boldsymbol{\eta}, \zeta) = \int_{\zeta_0}^{\zeta} \exp\left[- \int_{\zeta_0}^{\varrho} \nabla \cdot \boldsymbol{u}(\boldsymbol{y}(\boldsymbol{\eta}, \rho), \rho) d\rho \right] d\varrho, \tag{5.21}$$

for $\boldsymbol{\eta} \in \Omega_1$, $\zeta \in [\grave{\zeta}, 1]$, and arbitrary $\zeta_0 \in [\grave{\zeta}, 1]$.

The cost $J_{\mathrm{of},1}$ is stationary in the optical flow $\boldsymbol{u}$ for fixed I when $\boldsymbol{u}$ satisfies:

$$0 = \frac{1}{2} \frac{\delta J_{\mathrm{of}}}{\delta \boldsymbol{u}}(\boldsymbol{u}, \bar{\boldsymbol{u}}) = B_{\mathrm{of},1}(\boldsymbol{u}, \boldsymbol{u}, \bar{\boldsymbol{u}}) - F_{\mathrm{of}}(\bar{\boldsymbol{u}}), \quad \forall \bar{\boldsymbol{u}} \in H^1(Q, \boldsymbol{R}^N), \tag{5.22}$$

where $B_{\mathrm{of},1}$ and F_{of} are defined by:

$$\begin{aligned} B_{\mathrm{of},1}(\boldsymbol{u}, \boldsymbol{v}, \bar{\boldsymbol{u}}) &= \int_Q \left[(\nabla I \cdot \boldsymbol{u})(\nabla I \cdot \bar{\boldsymbol{u}}) + \gamma \left(\boldsymbol{u}_z \cdot \bar{\boldsymbol{u}}_z \right) \right] d\boldsymbol{x} dz \\ &+ \int_Q \phi' \left(\left| \nabla \boldsymbol{v}^{\mathrm{T}} + \nabla \boldsymbol{v} \right|^2 \right) \left(\nabla \boldsymbol{u}^{\mathrm{T}} + \nabla \boldsymbol{u} \right) : \left(\nabla \bar{\boldsymbol{u}}^{\mathrm{T}} + \nabla \bar{\boldsymbol{u}} \right) d\boldsymbol{x} dz \end{aligned} \tag{5.23}$$

$$F_{\mathrm{of}}(\bar{\boldsymbol{u}}) = - \int_Q I_z \nabla I \cdot \bar{\boldsymbol{u}} d\boldsymbol{x} dz. \tag{5.24}$$

In [45], (5.22) is solved by the lagged diffusivity iteration [79]:

$$B_{\mathrm{of},1}(\boldsymbol{u}_k, \boldsymbol{u}_{k-1}, \bar{\boldsymbol{u}}) = F_{\mathrm{of}}(\bar{\boldsymbol{u}}), \quad \forall \bar{\boldsymbol{u}} \in H^1(Q, \boldsymbol{R}^N), \qquad k = 1, 2, 3, \ldots \tag{5.25}$$

Note that no additional boundary conditions are imposed by restricting the domain of the form $B_{\mathrm{of},1}$, and thus natural boundary conditions hold. The following solvability of (5.25) is established in [52].

Theorem 14 *Suppose that for every $\boldsymbol{c} \in \boldsymbol{R}^N$ and for every skew symmetric matrix $W \in \boldsymbol{R}^{N\times N}$ the intensity $I \in W^{1,\infty}(Q, \boldsymbol{R})$ satisfies:*

$$\int_Q |\nabla I \cdot (\boldsymbol{c} + W\boldsymbol{x})|^2 d\boldsymbol{x}dz > 0, \tag{5.26}$$

unless $\boldsymbol{c} = 0$ and $W = 0$ hold. Then with $\phi(s) = \mu(\boldsymbol{x}, z)s$, $0 < \mu_0 \le \mu(\boldsymbol{x}, z) \le \mu_1 < \infty$, there exists a unique $\boldsymbol{u}_k \in H^1(Q, \boldsymbol{R}^N)$ such that (5.25) holds. If $\gamma = \infty$ so that the arguments of $B_{\mathrm{of},1}$ in (5.23) are z-independent, then (5.25) holds with Q replaced by Ω.

It is furthermore assumed that $\boldsymbol{u} \in H^1(Q, \boldsymbol{R}^N)$ has sufficient regularity so that (5.10) and (5.11) are well defined; see the discussion and references in [52].

The cost $J_{\mathrm{of},2}$ is stationary in the optical flow $\boldsymbol{u}$ for fixed I when $\boldsymbol{u}$ satisfies:

$$0 = \frac{1}{2}\frac{\delta J_{\mathrm{of}}}{\delta \boldsymbol{u}}(\boldsymbol{u}, \bar{\boldsymbol{u}}) = B_{\mathrm{of},2}(\boldsymbol{u}, \bar{\boldsymbol{u}}) - F_{\mathrm{of}}(\bar{\boldsymbol{u}}), \quad \forall \bar{\boldsymbol{u}} \in \mathcal{H}^2(Q, \boldsymbol{R}^N), \tag{5.27}$$

where $B_{\mathrm{of},2}$ is defined by:

$$\begin{aligned} B_{\mathrm{of},2}(\boldsymbol{u}, \bar{\boldsymbol{u}}) &= \int_Q \left[(\nabla I \cdot \boldsymbol{u})(\nabla I \cdot \bar{\boldsymbol{u}}) + \gamma\,(\boldsymbol{u}_z \cdot \bar{\boldsymbol{u}}_z)\right] d\boldsymbol{x}dz \\ &+ \mu \sum_{\substack{|\alpha| = 2 \\ \alpha_{N+1}=0}} \frac{2!}{\alpha!} \int_Q (\partial^\alpha \boldsymbol{u}) \cdot (\partial^\alpha \bar{\boldsymbol{u}}) d\boldsymbol{x}dz \end{aligned} \tag{5.28}$$

F_{of} is again defined by (5.24), and the Hilbert space and norm are defined according to:

$$\begin{aligned} &\mathcal{H}^2(Q, \boldsymbol{R}^N) = \{\boldsymbol{u} \in H^1(Q, \boldsymbol{R}^N) : \quad \partial^\alpha \boldsymbol{u} \in L^2(Q, \boldsymbol{R}^N), \quad |\alpha| = 2, \quad \alpha_{N+1} = 0\} \\ &\|\boldsymbol{u}\|^2_{\mathcal{H}^2(Q,\boldsymbol{R}^N)} = \|\boldsymbol{u}\|^2_{H^1(Q,\boldsymbol{R}^N)} + \sum_{\substack{|\alpha| = 2 \\ \alpha_{N+1}=0}} \int_Q |\partial^\alpha \boldsymbol{u}|^2 d\boldsymbol{x}dz. \end{aligned} \tag{5.29}$$

Note that no additional boundary conditions are imposed by restricting the domain of the form $B_{\mathrm{of},2}$, and thus natural boundary conditions hold. The following solvability of (5.27) is established in [45].

Theorem 15 *Suppose that for every $\boldsymbol{c} \in \boldsymbol{R}^N$ and for every matrix $W \in \boldsymbol{R}^{N\times N}$ the intensity $I \in W^{1,\infty}(Q, \boldsymbol{R})$ satisfies:*

$$\int_Q |\nabla I \cdot (\boldsymbol{c} + W\boldsymbol{x})|^2 d\boldsymbol{x}dz > 0, \tag{5.30}$$

unless $\boldsymbol{c} = 0$ and $W = 0$ hold. Then there exists a unique $\boldsymbol{u} \in \mathcal{H}^2(Q, \boldsymbol{R}^N)$ such that (5.27) holds. If $\gamma = \infty$ so that the arguments of $B_{\mathrm{of},2}$ in (5.28) are z-independent, then (5.27) holds with Q replaced by Ω.

It is furthermore assumed that $\boldsymbol{u} \in \mathcal{H}^2(Q, \boldsymbol{R}^N)$ has sufficient regularity so that (5.10) and (5.11) are well defined; see the discussion and references in [45].

Note that (5.1) and (5.2) are constructed with the priority that registration be independent of image order. However, it is shown in [45] that this order independence can only be shown in general for optical flow and not for finite displacements.

An image sequence may be registered or interpolated by processing the images only pairwise and concatenating the results. On the other hand, a coupling among images may be introduced as follows; see also [63]. The images of a sequence $\{I_l\}_{l=0}^L$ can be registered simultaneously using finite displacements $\{\boldsymbol{x}_l\}_{l=1}^L$ by minimizing:

$$J_{\mathrm{fd}}^{(L)}(\boldsymbol{x}_1,\ldots,\boldsymbol{x}_L)=\sum_{l=1}^{L}\mathcal{S}_{\mathrm{fd}}^{(l)}(\boldsymbol{x}_1,\ldots,\boldsymbol{x}_L)+\mathcal{R}_{\mathrm{fd}}(\boldsymbol{x}_l) \tag{5.31}$$

where:

$$\mathcal{S}_{\mathrm{fd}}^{(l)}(\boldsymbol{x}_1,\ldots,\boldsymbol{x}_L)=\sum_{|l-j|=1}\int_{\boldsymbol{R}^N}\left[I_j(\boldsymbol{x}_j(\boldsymbol{\xi}))-I_l(\boldsymbol{x}_l(\boldsymbol{\xi}))\right]^2 d\boldsymbol{\xi}. \tag{5.32}$$

When (5.31) has been minimized, the point $\boldsymbol{x}_i(\boldsymbol{\xi})\in\Omega_i$ has been matched to the point $\boldsymbol{x}_j(\boldsymbol{\xi})\in\Omega_j$. In [45], ${J_{\mathrm{fd}}}^{(L)}$ is minimized with respect to $\boldsymbol{x}_l$ while all other transformations are held fixed by replacing F_{fd} in (5.12) and (5.15) with ${F_{\mathrm{fd}}}^{(l)}=-\frac{1}{2}\delta{\mathcal{S}_{\mathrm{fd}}}^{(l)}/\delta\boldsymbol{x}$:

$$F_{\mathrm{fd}}^{(l)}(\boldsymbol{x}_l,\bar{\boldsymbol{x}})=\int_{\boldsymbol{R}^N}\sum_{|l-j|=1}\left[I_j(\boldsymbol{x}_j(\boldsymbol{\xi}))-I_l(\boldsymbol{x}_l(\boldsymbol{\xi}))\right]\nabla_{\boldsymbol{x}}I_l(\boldsymbol{x}_l(\boldsymbol{\xi}))^{\mathrm{T}}\bar{\boldsymbol{x}}(\boldsymbol{\xi})d\boldsymbol{\xi}. \tag{5.33}$$

This calculation shows that $J_{\mathrm{fd}}^{(L)}$ is just as well minimized with respect to $\boldsymbol{x}_l$ by registering the image I_l with the image $I_{l_{\mathrm{n}}}(\boldsymbol{\xi})=\sum_{|j-l|=1}^{0\le j\le L}I_j(\boldsymbol{x}_j(\boldsymbol{\xi}))/\sum_{|j-l|=1}^{0\le j\le L}$. The functional $J_{\mathrm{fd}}^{(L)}$ is minimized in [45] by a Jacobi update strategy. Known transformations remain frozen as fixed boundary conditions, e.g., at one or both of the end indices $l=0$ and $l=L$ in (5.31) when the position of one or both of the end images I_0 and I_L is known.

The images $\{I_l\}_{l=0}^L$ can be interpolated from autonomous optical flows $\{\boldsymbol{u}_l\}_{l=0}^{L-1+\nu}$ using the semi-discretization defined on $Q^{(L)}=\Omega\times(0,L)$:

$$\boldsymbol{u}(\boldsymbol{x},z)=\sum_{l=0}^{L}\boldsymbol{u}_l(\boldsymbol{x})\chi_l^{\nu}(z) \tag{5.34}$$

where $\{\chi_l^{\nu}\}$ is the canonical basis for the B-splines of degree ν defined on the grid $\{[l,l+1]\}_{l=0}^{L-1}$ of $[0,L]$. Then, as shown explicitly in [45], the transformations are given by modifications of (5.10) and (5.11) and the intensities by modifications of (5.18) and (5.19). For instance, for $\nu=0$, χ_l^0 is the characteristic function for the interval $[l,l+1]$, and the above procedure corresponds to pairwise interpolation of the given images. When smoother trajectories and greater coupling among images are desired, higher-order splines are used in (5.34), and (5.22) or (5.27) can be solved for $\{\boldsymbol{u}_l\}_{l=0}^{L-1+\nu}$ with $\gamma=0$ and Q replaced by $Q^{(L)}$. This approach will be investigated further in forthcoming work.

The generalized rigid optical flow is obtained under landmark constraints, $\boldsymbol{x}(\boldsymbol{\xi}_\jmath,1)=\boldsymbol{x}_\jmath$, $\jmath=1,\ldots,\hat{\jmath}$, when the following Lagrangian function is stationary:

$$L(\boldsymbol{u},\boldsymbol{\lambda})=\tfrac{1}{2}J_{\mathrm{of},1}(I,\boldsymbol{u})+\boldsymbol{\lambda}^{\mathrm{T}}\boldsymbol{E}(\boldsymbol{u}), \tag{5.35}$$

where the intensity is fixed by (5.18) and (5.19), $\boldsymbol{\lambda}\in\boldsymbol{R}^{N\hat{\jmath}}$ and:

$$\boldsymbol{E}_\jmath(\boldsymbol{u})=\boldsymbol{x}(\boldsymbol{\xi}_\jmath,1)-\boldsymbol{x}_\jmath=\boldsymbol{\xi}_\jmath-\boldsymbol{x}_\jmath+\int_0^1\boldsymbol{u}(\boldsymbol{x}(\boldsymbol{\xi}_\jmath,\rho),\rho)d\rho,\qquad \jmath=1,\ldots,\hat{\jmath}. \tag{5.36}$$

As shown in [47], the stationarity conditions for L are:

$$\frac{\delta L}{\delta\boldsymbol{u}}(\boldsymbol{u};\bar{\boldsymbol{u}}) \;=\; B_{\mathrm{of},1}(\boldsymbol{u},\boldsymbol{u},\bar{\boldsymbol{u}})-F_{\mathrm{of}}(\bar{\boldsymbol{u}})+\boldsymbol{\lambda}^{\mathrm{T}}\boldsymbol{G}(\boldsymbol{u},\bar{\boldsymbol{u}}) \;=\; 0,\qquad \forall\bar{\boldsymbol{u}}\in C^{\infty}(\bar{Q}), \tag{5.37}$$

$$\frac{\partial L}{\partial\boldsymbol{\lambda}} \;=\; \boldsymbol{E}(\boldsymbol{u}) \;=\; 0. \tag{5.38}$$

where $B_{\text{of},1}$ and F_{of} are given by (5.23) and (5.24), and $\boldsymbol{G}$ is the functional with $\jmath$th component:

$$\boldsymbol{G}_\jmath(\boldsymbol{u}, \bar{\boldsymbol{u}}) = \int_0^1 S_{\boldsymbol{u},\jmath}(1,\rho)\bar{\boldsymbol{u}}(\boldsymbol{x}(\boldsymbol{\xi}_\jmath,\rho),\rho)d\rho, \quad \jmath = 1,\ldots,\hat{\jmath} \tag{5.39}$$

defined in terms of the evolution operator:

$$\begin{array}{rcll} S_{\boldsymbol{u},\jmath}(\zeta,\varrho)S_{\boldsymbol{u},\jmath}(\varrho,\rho) &=& S_{\boldsymbol{u},\jmath}(\zeta,\rho), & 0 \le \rho \le \varrho \le \zeta \le 1 \\ S_{\boldsymbol{u},\jmath}(\zeta,\zeta) &=& I, & \zeta \in [0,1] \\ \partial_\zeta S_{\boldsymbol{u},\jmath}(\zeta,\rho) &=& \nabla\boldsymbol{u}(\boldsymbol{x}(\boldsymbol{\xi}_\jmath,\zeta),\zeta)S_{\boldsymbol{u},\jmath}(\zeta,\rho) & \\ \partial_\rho S_{\boldsymbol{u},\jmath}(\zeta,\rho) &=& -S_{\boldsymbol{u},\jmath}(\zeta,\rho)\nabla\boldsymbol{u}(\boldsymbol{x}(\boldsymbol{\xi}_\jmath,\rho),\rho). & \end{array} \tag{5.40}$$

As stated after Theorem 14, it is assumed that $\boldsymbol{u} \in H^1(Q,\boldsymbol{R}^N)$ has sufficient regularity so that (5.10) and (5.11) are well defined; see the discussion and references in [47]. Thus, the following existence of the Lagrange multipliers in (5.37) is established in [47].

Theorem 16 *Assume that $J(\boldsymbol{u})$ is minimized subject to $\boldsymbol{E}(\boldsymbol{u}) = 0$ at $\boldsymbol{u}^* \in H^1(Q) \cap W^{1,\infty}(Q)$. Then there exists a $\boldsymbol{\lambda}^* \in \boldsymbol{R}^{2\hat{\jmath}}$ such that $(\boldsymbol{u}^*, \boldsymbol{\lambda}^*)$ satisfy (5.37).*

The form of (5.37) and (5.38) are elucidated by simple examples in [47], and landmark constrained image registration and interpolation by means of optical flow will be investigated in forthcoming work.

5.2 Numerical and Computational Formulations [52], [45], [13]

The registration schemes for finite displacements and for optical flow are summarized algorithmically as follows.

- For finite displacements: set $\boldsymbol{x}(\boldsymbol{\xi}) = \boldsymbol{\xi}$ and continue the following until changes in $\boldsymbol{x}$ meet a convergence criterion:
  - solve one step of (5.15) for the solution of (5.12), and in the process,
  - perform a line search to determine the step size in (5.15) so that (5.1) is minimized.
- For optical flow: set $\boldsymbol{u} = 0$ and continue the following until changes in $\boldsymbol{u}$ meet a convergence criterion:
  - perform the integrations (5.10), (5.11), (5.20) and (5.21),
  - compute I from (5.18) and (5.19),
  - solve (5.27) for the optical flow, or
  - solve one step of (5.25) for the solution of (5.22), while (5.25) is equivalent to (5.22) when (5.22) is linear.

The discretization and numerical solution of these equations is obtained as follows. First, Q and thus Ω are discretized by a grid of cells, where nested cells are illustrated in Fig. 16 for Ω. For finite displacements $\boldsymbol{x}$, for the given images I_0 and I_1, and for autonomous optical flows $\boldsymbol{u}$, only the discretization of Ω is required, and $(I_0)_{\boldsymbol{i}}$ for instance denotes the value of I_0 at the cell centroid $\mathbf{x}_{\boldsymbol{i}}$. However, the intensity I for optical flow is defined throughout Q and $I_{\boldsymbol{i},k}$ denotes the value of I at the cell centroid $(\mathbf{x}_{\boldsymbol{i}}, \mathrm{z}_k)$.

For finite displacements computed in [45], (5.14) is computed using multilinear interpolation of I_0 and I_1, and (5.14) and (5.16) are computed using central differences to construct ∇I_0 and ∇I_1 and multilinear interpolation to evaluate these gradients. The quadrature rule for these integrals involves sums of integrands evaluated at spline peaks.

For the computation of optical flows, it is explained in [52] that the associated intensity must be computed according to a Lagrangian discretization, as illustrated in Fig. 22, since an

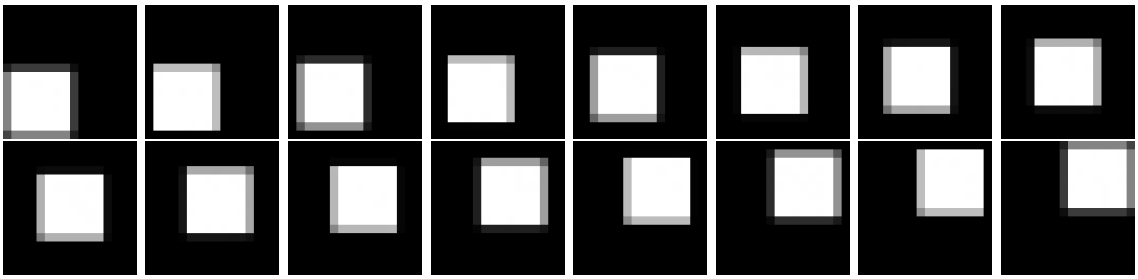

Figure 22: End images I_0 and I_1 are shown in the upper left and in the lower right, and the sequence of images between them, read from left to right and from top to bottom, has been determined with a Lagrangian discretization based upon (5.18) and (5.19).

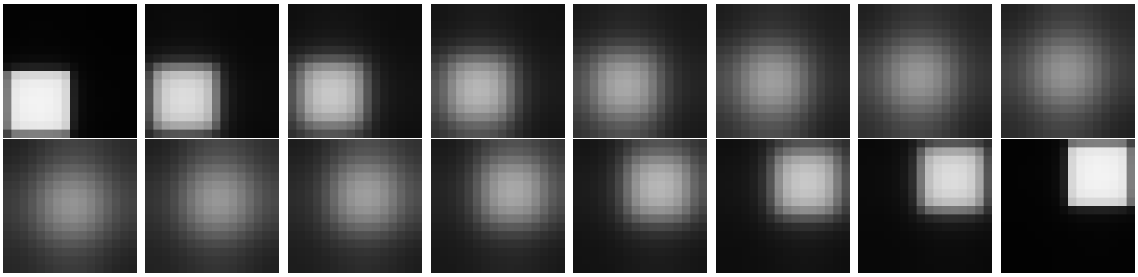

Figure 23: End images I_0 and I_1 are shown in the upper left and in the lower right, and the sequence of images between them, read from left to right and from top to bottom, has been determined with an Eulerian discretization based upon the optimality condition for $J_{\text{of},1}$.

Eulerian discretization is too dissipative, as illustrated in Fig. 23. Furthermore, the Lagrangian discretization must be implemented by performing the trajectory integrations (5.10), (5.11), (5.20) and (5.21) from each cell center in Q both toward Ω_0 and toward Ω_1. Nevertheless, a considerable savings is achieved for these integrations when the optical flow is autonomous since trajectories emanating from cells differing only in depth overlap in the optical flow phase space. These trajectory integrations are approximated using a Runge-Kutta method, where multilinear interpolation is used to obtain distributed values of the optical flow and its divergence, and optical flow derivatives are computed using central differences. The terms ∇I and I_z are computed for (5.23), (5.24) and (5.28) by using central differences for ∇I and by determining I_z from the optical flow equation using the current optical flow and the trajectory derivative $dI/d\zeta$ available from (5.18) or (5.19). The quadrature rule for the integrals in (5.23), (5.24) and (5.28) involves sums of integrands evaluated at spline peaks.

When only autonomous optical flows are considered numerically, each of the boundary value problems (5.15), (5.25) and (5.27) has the form detailed from (4.2) to (4.21) with each function space, e.g., $S_h^\nu(\Omega)$, replaced by a vector-valued counterpart, e.g., $S_h^\nu(\Omega, \boldsymbol{R}^N)$, and with each function, e.g., $\varphi_h \in S_h^\nu(\Omega)$, replaced by its vector-valued counterpart, e.g., $\boldsymbol{\varphi}_h \in S_h^\nu(\Omega, \boldsymbol{R}^N)$. For (5.15) and (5.27), $\nu = 2$ and the regularity (4.21) follows from Theorem 8. For (5.22), $\nu = 1$ and the regularity is seen in examples of [52] not to hold for total variation regularization. On the other hand, for a fixed k the solution to (5.25) possesses the regularity corresponding to Gaussian regularization, and while the regularity (4.21) for (5.22) or (5.25) does not follow immediately from Theorem 8, such regularity is assumed for the examples of interest in [45]. In the lumped formulation the coefficients $\boldsymbol{\Phi}_{h,\boldsymbol{i}} = \{\boldsymbol{\Phi}_{h,\boldsymbol{i}}^{(n)}\} \in \boldsymbol{R}^N$ are solution values $\boldsymbol{\Phi}_{h,\boldsymbol{i}} = \boldsymbol{\varphi}_h(\mathbf{x}_{\boldsymbol{i}-\frac{\nu}{2}})$ at basis function peaks, and (4.15) takes the form:

$$\sum_{\substack{1 \le n \le N \\ \mathbf{1} \le \boldsymbol{j} \le (2^p+\nu)\cdot\mathbf{1}}} \left[B_\mu(\chi_{\boldsymbol{i}}^\nu \boldsymbol{e}_m, \chi_{\boldsymbol{j}} \boldsymbol{e}_n) + B_0(\chi_{\boldsymbol{i}-\frac{\nu}{2}}^0 \boldsymbol{e}_m, \chi_{\boldsymbol{j}-\frac{\nu}{2}}^0 \boldsymbol{e}_n) \right] \boldsymbol{\Phi}_{h,\boldsymbol{j}}^{(n)} = F(\chi_{\boldsymbol{i}-\frac{\nu}{2}}^0 \boldsymbol{e}_m),$$

$$\mathbf{1} \le \boldsymbol{i} \le (2^p+\nu)\cdot\mathbf{1}, \quad 1 \le m \le N \tag{5.41}$$

where $\{\chi_{\boldsymbol{i}}^{\nu}\}$ is the canonical B-spline basis for $S_n^{\nu}(\Omega)$ and $\boldsymbol{e}_n \in \boldsymbol{R}^N$ satisfies $(\boldsymbol{e}_n)^{(m)} = \delta_{mn}$. The coefficient matrix in (5.41) is computed for the bilinear form D_{fd} of (5.15) using the structure shown in (4.3), where the first term in (5.16) corresponds to B_μ and the remaining term in (5.16) corresponds to B_0. For the bilinear form $B_{\text{of},1}$ of (5.22) and (5.25) the first integral in (5.23) (with $\gamma = 0$) corresponds to B_0 and the second integral of (5.23) (with integration over Q replaced by integration over Ω) corresponds to B_μ. For the bilinear form $B_{\text{of},2}$ of (5.27) the first integral in (5.28) (with $\gamma = 0$) corresponds to B_0 and the second integral in (5.28) (with integration over Q replaced by integration over Ω) corresponds to B_μ. For these cases (5.16), (5.23) and (5.28), the coefficient matrix of (5.41) is shown in [45] to be positive definite as follows.

Theorem 17 *For a given $\boldsymbol{x}_k \in H^2(\Omega_0)$, suppose that for every $\boldsymbol{c} \in \boldsymbol{R}$ and for every matrix $W \in \boldsymbol{R}^{N\times N}$ the image I_1 satisfies:*

$$\sum_{\mathbf{1}\le \boldsymbol{i} \le (2^p+\nu)\cdot\mathbf{1}} |\nabla_{\boldsymbol{x}} I_1(\boldsymbol{x}_k(\mathbf{x}_{\boldsymbol{i}-\frac{\nu}{2}})) \cdot (\boldsymbol{c} + W\mathbf{x}_{\boldsymbol{i}-\frac{\nu}{2}})|^2 > 0 \tag{5.42}$$

unless $\boldsymbol{c} = 0$ and $W = 0$ hold. Then the coefficient matrix A_{fd} of (5.41) corresponding to D_{fd} is symmetric and positive definite.

Theorem 18 *Suppose that for every $\boldsymbol{c} \in \boldsymbol{R}$ and for every skew symmetric matrix $W \in \boldsymbol{R}^{N\times N}$ the intensity I satisfies:*

$$\sum_{1\le k\le 2^q} \sum_{\mathbf{1}\le \boldsymbol{i} \le (2^p+\nu)\cdot\mathbf{1}} |(\nabla I)_{\boldsymbol{i}-\frac{\nu}{2},k} \cdot (\boldsymbol{c} + W\mathbf{x}_{\boldsymbol{i}-\frac{\nu}{2}})|^2 > 0 \tag{5.43}$$

unless $\boldsymbol{c} = 0$ and $W = 0$ hold. Then the coefficient matrix $A_{\text{of},1}$ of (5.41) corresponding to $B_{\text{of},1}$ is symmetric and positive definite.

Theorem 19 *Suppose that for every $\boldsymbol{c} \in \boldsymbol{R}$ and for every matrix $W \in \boldsymbol{R}^{N\times N}$ the intensity I satisfies:*

$$\sum_{1\le k\le 2^q} \sum_{\mathbf{1}\le \boldsymbol{i} \le (2^p+\nu)\cdot\mathbf{1}} |(\nabla I)_{\boldsymbol{i}-\frac{\nu}{2},k} \cdot (\boldsymbol{c} + W\mathbf{x}_{\boldsymbol{i}-\frac{\nu}{2}})|^2 > 0 \tag{5.44}$$

unless $\boldsymbol{c} = 0$ and $W = 0$ hold. Then the coefficient matrix $A_{\text{of},2}$ of (5.41) corresponding to $B_{\text{of},2}$ is symmetric and positive definite.

The geometric multigrid formulation for the solution of each of the boundary value problems (5.15), (5.25) and (5.27) has the form detailed from (4.22) to (4.42). In particular, using the structure of (4.3) to (4.5) and including lumping (5.41), it is proved in [45] for each of these cases that (4.33) holds, and it is further shown that Theorems 9 – 12 hold.

The discussion of implementation aspects following (4.42) applies equally well for the problems (5.15), (5.25) and (5.27), including the treatment of floating point errors by the careful computation of scalar products, the rejection of alternative finite difference formulations and the study of the effect of variations in data support and method parameters. In the present context, certain aspects deserve special attention, including a multi-colored ordering for vector-valued functions and the treatment of nonlinearities.

For the multi-colored ordering, let the coefficient matrix A_h shown in (5.41) by partitioned into $N \times N$ blocks corresponding to pairs (m, n):

$$A_h^{(m,n)} = \{B_\mu(\chi_{\boldsymbol{i}}^{\nu}\boldsymbol{e}_m, \chi_{\boldsymbol{j}}\boldsymbol{e}_n) + B_0(\chi^0_{\boldsymbol{i}-\frac{\nu}{2}}\boldsymbol{e}_m, \chi^0_{\boldsymbol{j}-\frac{\nu}{2}}\boldsymbol{e}_n) : \mathbf{1} \le \boldsymbol{i}, \boldsymbol{j} \le (2^p + \nu)\cdot\mathbf{1}\}. \tag{5.45}$$

For a fixed block (m, n), the multi-colored ordering described for (4.43) applies. Thus, the vector-valued counterpart to (4.31) can be implemented by performing an outer symmetric

Gauss-Seidel iteration over component blocks (m, n) and an inner Jacobi iteration on same-colored stencils c looping in one direction and then the other over the colors:

$$\begin{aligned}
&\text{for } m = 1, \ldots, N \text{ and then } m = N, \ldots, 1 \\
&\quad \boldsymbol{R}_l^{(m)} = \boldsymbol{F}_l^{(m)} - \textstyle\sum_{n \neq m} A_l^{(m,n)} \boldsymbol{\Phi}_l^{(m)} \\
&\quad \text{for } c = 1, \ldots, (\nu+1)^N \text{ and then } c = (\nu+1)^N, \ldots, 1 \\
&\qquad \boldsymbol{\Phi}_l^{(m)}(c) \leftarrow \boldsymbol{\Phi}_l^{(m)}(c) - \omega[(\mathcal{D}_l^{(m,m)})^{-1}(A_l^{(m,m)} \boldsymbol{\Phi}_l^{(m)} - \boldsymbol{R}_l^{(m)})](c).
\end{aligned} \tag{5.46}$$

As with (4.43), same-colored cells may be updated simultaneously.

The nonlinearity leading to the lagged diffusivity iteration (5.25) may alternatively be considered in the context of nonlinear multigrid [78], but such a formulation was tested in [45] and found as follows to be unacceptable. Specifically, to determine the coarse grid operator, a representation of $\boldsymbol{u}$ must be selected for the diffusivity $\phi'(|\nabla \boldsymbol{u}^{\mathrm{T}} + \nabla \boldsymbol{u}|^2)$ which appears in the following counterpart to (4.23):

$$(L_l(\boldsymbol{u})\boldsymbol{\chi}, \boldsymbol{\psi})_{L^2(\Omega, \boldsymbol{R}^N)} = B(\boldsymbol{\chi}, \boldsymbol{u}, \boldsymbol{\psi}), \quad \forall \boldsymbol{\chi}, \boldsymbol{\psi} \in S_l^{\nu}(\Omega, \boldsymbol{R}^N). \tag{5.47}$$

Given a suitable approximation $\boldsymbol{u}_{l+1} \in S_{l+1}^{\nu}(\Omega, \boldsymbol{R}^N)$, the natural candidate for $\boldsymbol{u}$ in (5.47) is $\boldsymbol{u}_l = I_l^* \boldsymbol{u}_{l+1}$. However, the canonical restriction operator transforms $\boldsymbol{u}_{l+1}$ to a function $\boldsymbol{u}_l$ which is always diminished on $\partial\Omega$ in relation to $\boldsymbol{u}_{l+1}$, and thus the diffusivity obtained on level l from restriction is significantly different on the boundary than the corresponding diffusivity on level $l+1$. It is readily demonstrated that this difference corrupts the coarse grid correction of nonlinear multigrid. It is also shown in [78] that an outer iteration update strategy can be combined with linear multigrid in an inner iteration so that the total computational work is comparable to that of nonlinear multigrid when it functions, and such strategies can be implemented in relation to (5.25). Nevertheless, no visible advantage to non-quadratic penalties could be demonstrated for practical examples in [45], in spite of the apparent advantages evident from simple examples shown in [52].

Even when a nonlinearity such as (5.25) is not present and the regularity measure is quadratic, the minimization of J_{fd}, $J_{\mathrm{of},1}$ and $J_{\mathrm{of},2}$ is still nonlinear because of the similarity measure. For this, a pyramidal scheme is implemented in [45] for a chosen $l_{\min}$, $0 \leq l_{\min} \leq l_{\max}$, in combination with the algorithmic outline given above:

- For $l = l_{\max}, \ldots, l_{\min} + 1$ restrict I_0 and I_1 from multigrid level l to level $l-1$.
- For $l = l_{\min}, \ldots, l_{\max}$:
  - if $l = l_{\min}$ initialize the displacement or optical flow trivially,
  - else expand the displacement or optical flow from multigrid level $l-1$ to level l.
  - solve for the displacement or optical flow on multigrid level l.

The efficiency of this pyramidal scheme depends upon the accurate representation of the images on the coarse grids. As explained in relation to (5.47), images are diminished at the image domain boundary by restriction. If the restricted images are not particularly representative of those given on the fine grid, the displacement or the optical flow computed on a coarse grid may also be correspondingly biased. In such cases, stronger regularization is used on coarser grids or else $l_{\min}$ is chosen nearer to $l_{\max}$.

Generalized rigid and generalized affine image registration and interpolation are demonstrated in terms of a simple example in Fig. 24. Here, the two given images I_0 and I_1, shown respectively at the left and at the right of the first row, are related by an affine transformation. The other images shown in the first row of Fig. 24 are interpolated between the given images by generalized affine optical flow (5.27). The successful computation of an affine interpolation is evident visually from the sequence of images and quantitatively from very small registration

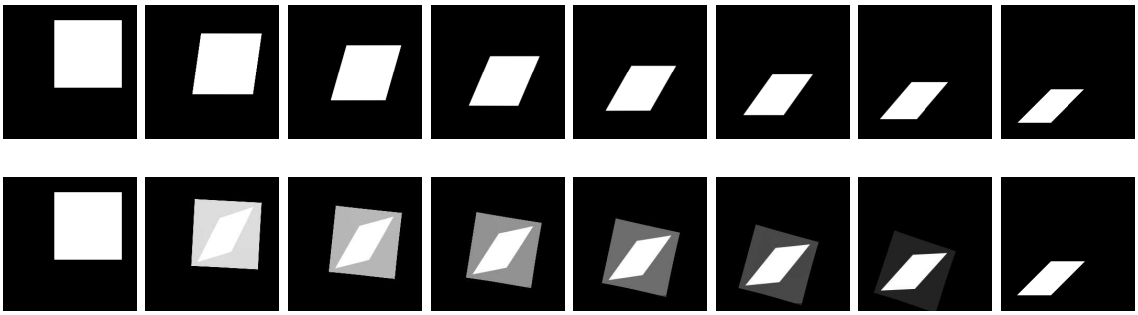

Figure 24: An interpolated image sequence obtained by generalized affine optical flow (5.27) is shown in the first row. The sequence is to be read from left to right. The given images I_0 and I_1 are shown respectively at the beginning and at the end of the sequence. For the same given images I_0 and I_1, an interpolated image sequence obtained by generalized rigid optical flow (5.22) is shown in the second row.

errors [45]. The interpolation obtained by (5.27) is also visually independent of regularization strength. On the other hand, the images shown in the second row of Fig. 24 are interpolated between the same given images by generalized rigid optical flow (5.22) with a Gaussian penalty. The regularization here is strong enough that each image is transported rigidly toward the other and the interpolation is the average of the respective morphs. Considering a single morph gives a registration of one image to the other, and for the chosen regularization strength the associated registration errors are relatively large [45]. In case the given images are related by a rigid registration, the resulting interpolation and registration are as accurate and natural as is (5.27) for the example shown in Fig. 24; see [52]. When the given images I_0 and I_1 in Fig. 24 are registered according to (5.12), the morphed images are visually indistinguishable from the original images, and the registration errors are very small [45].

The computations described above were carried out according to the algorithmic outlines given earlier, and chosen parameters are detailed in [45]. For the final outer iteration on the finest pyramidal level, convergence histories of $M_l^V(1)$ iterations for (5.12), (5.22) and (5.27) for the example of Fig. 24 are shown in Fig. 25. On the basis of the results reported in [50], the

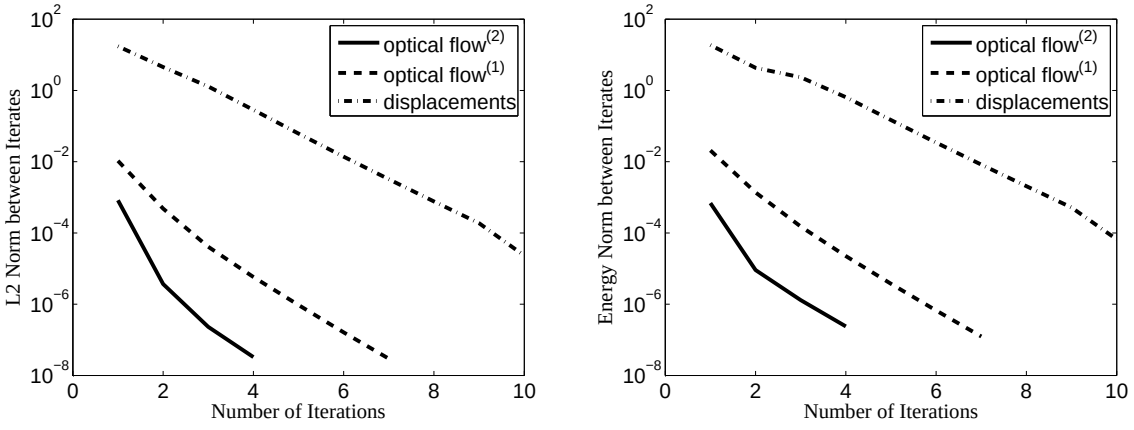

Figure 25: Convergence histories for (5.12), (5.22) and (5.27) of successive iterates are shown for $M_l^V(1)$ iterations in the norm $\|\cdot\|_{\ell_2}$ on the left and in the norm $\|A_h^{1/2}\cdot\|_{\ell_2}$ on the right. The solid curve is for (5.27), the dashed curve is for (5.22), and the dot-dashed curve is for (5.12).

smaller multigrid reduction factors for optical flow can be understood from the fact that the data $\int_0^1 \nabla I(\boldsymbol{x},z)\nabla I(\boldsymbol{x},z)^{\mathrm{T}}dz$ for optical flow have broader support than the data $\nabla I_1(\boldsymbol{x})\nabla I_1(\boldsymbol{x})^{\mathrm{T}}$ for finite displacements.

Although the registration result with (5.22) in Fig. 24 is unnaturally rigid, Fig. 26 shows an example to compare strongly and weakly rigid registration, which according to [52] are obtained respectively by flexing or relaxing the strength of the rigidity penalty in $J_{\mathrm{of},1}$; see [52] for details.

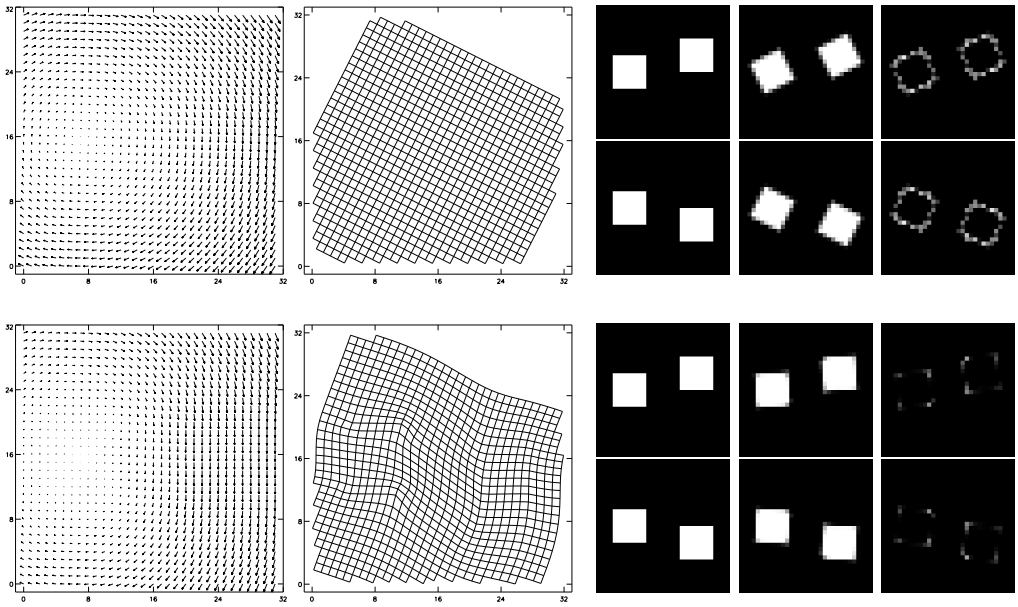

Figure 26: Strongly and weakly rigid registration are demonstrated in the top and bottom rows respectively. The optical flow shown in the left column happens to be autonomous. The middle column shows the morphing of a uniform grid from Ω_0 to Ω_1. The image I_0 is displayed above the image I_1 in the third column, the morphing of I_1 is displayed above the morphing of I_0 in the fourth column, and the errors between images and corresponding morphs are shown in the final column on the right.

Note that in the example of strongly rigid registration in the top row the morphed images are clearly the result of a rigid transformation applied to the original images, whereas in the example of weakly rigid registration in the bottom row the morphed images match the original images much more closely. As demonstrated by the morphed uniform grids, trajectories are allowed to move out of the box Q, and such movement is necessary for rigid motion. Note further in this example that the optical flow has not been constrained to be autonomous, but the minimization of $J_{\text{of},1}$ has led to an autonomous flow even for the weakly rigid case.

While all other registration examples are processed with quadratic penalties, Fig. 27 demonstrates the use of a non-quadratic penalty to process a model of an excision. Specifically, a vertical stripe of the brightest intensities in the middle of I_0 is removed and the remainder is translated toward the central vertical axis and joined to create I_1. The two images are registered using Gaussian and (regularized) total variation penalties; see [52] for details. The differences in registration accuracy appear conspicuously from the morphed uniform grids. The Gaussian penalty causes points outside the excised stripe to be crowded and deformed together with points inside the stripe. With the total variation penalty, points inside the excised stripe appear to have disappeared into the vertical axis while points outside the stripe appear to have been translated identically toward the vertical axis. As discussed following (5.47), the example of Fig. 27 promises to allow discontinuities in the optical flow and thereby to permit accurate registration in the presence of rigid and non-rigid objects; however, the result shown below for the realistic example of Fig. 29 is not visibly affected by the use of a total variation penalty instead of a Gaussian penalty.

Examples of registered and interpolated magnetic resonance images are given in [52], [45] and [46], and the next two examples are selected to demonstrate the processing of image sequences. For Fig. 28, the sequence of histological sections of a mouse heart shown on the left have been aligned by generalized affine registration (5.31) as shown on the right; see [45] for further details concerning the computations as well as films of the raw and registered sequences. This alignment has been achieved by first shifting all images to the same center of mass and then performing a single iteration of the update strategy described for the minimization of (5.31). Generalized affine registration is considered suitable for histological applications since sections may be affine

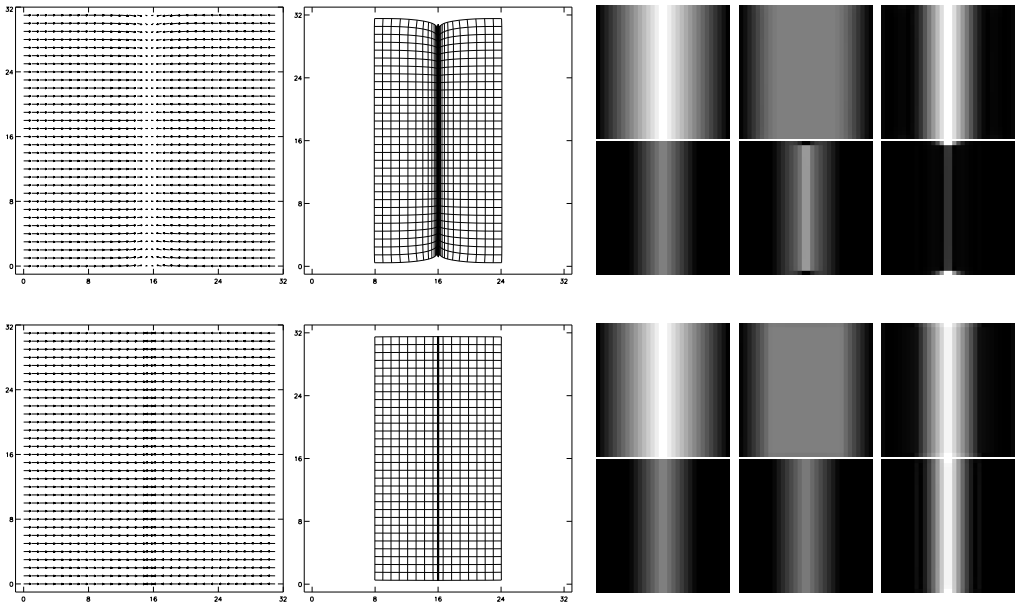

Figure 27: Using the same format as in Fig. 26, results obtained by Gaussian and (regularized) total variation penalties are shown respectively in the top and bottom rows.

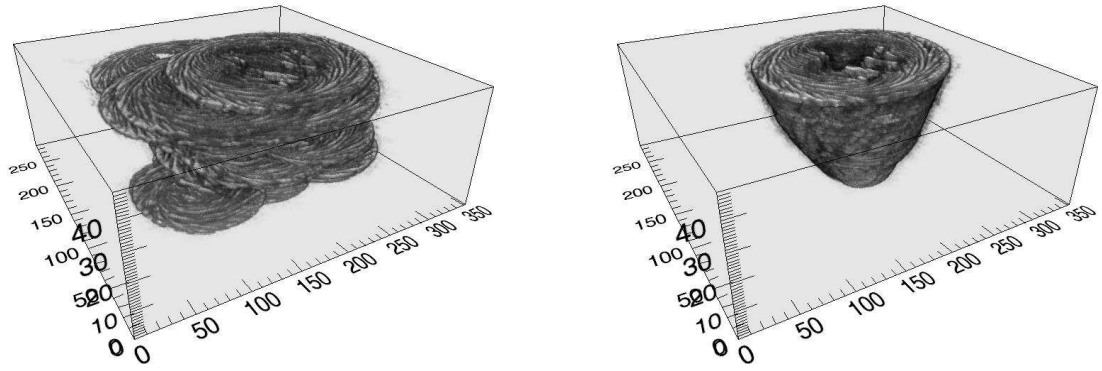

Figure 28: A sequence of histological sections of a mouse heart are shown unregistered on the left and registered by finite displacements on the right.

deformed in the process of slicing, but unless certain images in (5.31) are fixed, (generalized) affine transformations can expand or contract images so that an object is deformed essentially to the same size throughout the entire stack. This effect can also be controlled by the number of updates performed in order to solve the entire coupled optimality system for (5.31).

On the other hand, generalized rigid registration provides resistance to deformation, and it is used for the example of Fig. 29. Here, respiratory motion accompanies the sudden and widespread appearance of contrast agent, particularly in the kidneys, and it is required to interpolate between the two given images shown respectively at the extreme upper left and at the extreme lower right. The other images shown in the figure have been interpolated using generalized rigid optical flow (5.22) combined with intensity scaling described below. Note that several objects move and deform as a result of respiration but the spinal column, for instance, remains rigid and motionless. Such an example appears to be a good candidate for a realistic application of total variation regularization as discussed in [52]. However, and as indicated following (5.47), the result shown in Fig. 29 is not perceptibly affected by the use of total variation regularization. The raw and interpolated images shown in Fig. 29 are actually samples taken from a lengthy temporal sequence in which temporal resolution is low enough for the raw

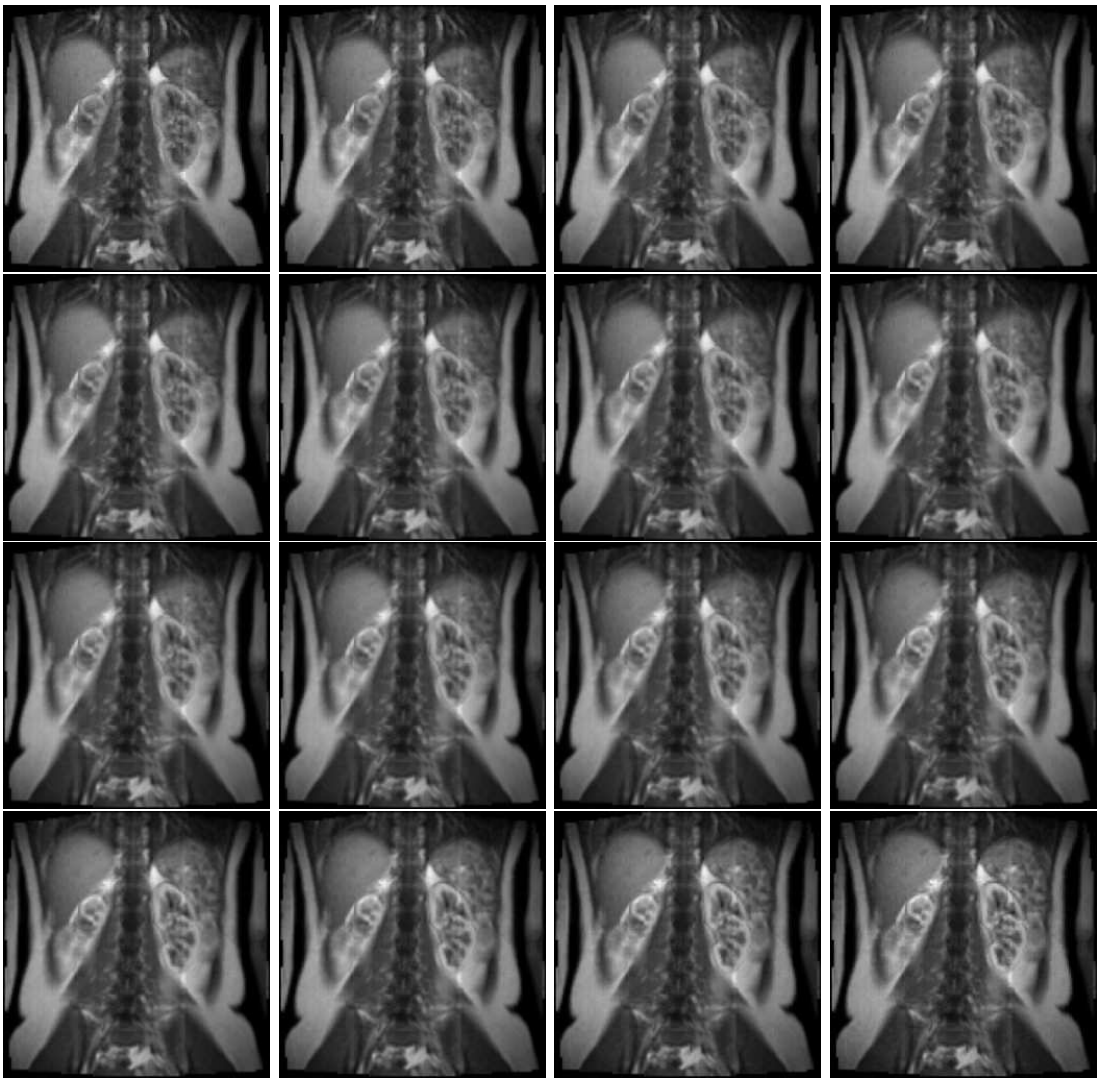

Figure 29: The two given images I_0 and I_1 are shown respectively in the extreme upper left and in the extreme lower right. The images in between are read from left to right and from top to bottom and they have been interpolated by generalized rigid optical flow.

sequence to be quite jerky but high enough to permit a smooth interpolation which facilitates the medical examination. The entire raw image sequence has been interpolated pairwise as described for Fig. 29; see [45] and [46] for further details concerning the computations as well as films of the raw and interpolated sequences.

5.3 Image Similarity by Intensity Scaling [46]

In the procedures discussed above, the image similarity measure is based upon pure intensities, while realistic medical applications are complicated by the appearance of contrast agent or an intensity modulation in one image and not in another to which the first must be matched. For such applications, an image similarity measure based upon intensity scaling, as opposed to intensity differentiation [20] [21], is developed in [46] for both finite displacements and for optical flow.

Intensity scaling is introduced as follows to the similarity measures (5.1) and (5.2) without favoring a given image order. Specifically, reciprocal scaling is necessary in order that registration be independent of image order, and it is shown in [46] that order independence can be achieved in general for optical flow but for finite displacements only under limited circumstances. For reciprocal scaling, let $\sigma_0 : [0,1] \to [0,1]$ and $\sigma_1 : [0,1] \to [0,1]$ be functions scaling

the intensities of I_0 and I_1 respectively. Then intensity scaling is introduced into (5.1) according to:

$$\begin{aligned}
&\mathcal{S}_{\rm fd}(\boldsymbol{x},\sigma_0,\sigma_1)\\
&=\int_{\Omega_0^{\rm c}}\left[\sigma_0(I_0(\boldsymbol{\xi}))-I_1(\boldsymbol{x}(\boldsymbol{\xi}))\right]^2 d\boldsymbol{\xi}+\int_{\Omega_0^{\rm i}}\left[\sigma_0(I_0(\boldsymbol{\xi}))-I_1^{\infty}\right]^2 d\boldsymbol{\xi}+\int_{\Omega_1^{\rm i}}\left[\sigma_0(I_0^{\infty})-I_1(\boldsymbol{\eta})\right]^2 d\boldsymbol{\eta}\\
&+\int_{\Omega_1^{\rm c}}\left[I_0(\boldsymbol{y}(\boldsymbol{\eta}))-\sigma_1(I_1(\boldsymbol{\eta}))\right]^2 d\boldsymbol{\eta}+\int_{\Omega_0^{\rm i}}\left[I_0(\boldsymbol{\xi})-\sigma_1(I_1^{\infty})\right]^2 d\boldsymbol{\xi}+\int_{\Omega_1^{\rm i}}\left[I_0^{\infty}-\sigma_1(I_1(\boldsymbol{\eta}))\right]^2 d\boldsymbol{\eta}
\end{aligned}\tag{5.48}$$

where each line in (5.48) represents the effect of scaling just one of the given images. Intensity scaling is introduced into (5.2) according to:

$$\mathcal{S}_{\rm of}(\boldsymbol{u},I^{(1)},I^{(2)},\sigma_0,\sigma_1)=\int_Q\left\{[\nabla_{\boldsymbol{x}}I^{(0)}\cdot\boldsymbol{u}+I_z^{(0)}]^2+[\nabla_{\boldsymbol{x}}I^{(1)}\cdot\boldsymbol{u}+I_z^{(1)}]^2\right\}d\boldsymbol{x}dz\tag{5.49}$$

where the intensity $I^{(0)}$ is constrained by the following modifications of (5.3) and (5.4):

$$I^{(0)}=I_0 \text{ on } \Omega_0,\quad I^{(0)}=\sigma_1(I_1) \text{ on } \Omega_1,\quad I^{(0)}=\sigma_1(I_1^{\infty}) \text{ on } \Gamma_+,\quad I^{(0)}=I_0^{\infty} \text{ on } \Gamma_-\tag{5.50}$$

in which only I_1 is scaled, and the intensity $I^{(1)}$ is constrained by the following modifications of (5.3) and (5.4):

$$I^{(1)}=\sigma_0(I_0) \text{ on } \Omega_0,\quad I^{(1)}=I_1 \text{ on } \Omega_1,\quad I^{(1)}=I_1^{\infty} \text{ on } \Gamma_+,\quad I^{(1)}=\sigma_0(I_0^{\infty}) \text{ on } \Gamma_-\tag{5.51}$$

in which only I_0 is scaled.

For image registration by means of finite displacements, (5.5) is modified as follows [46]:

$$J_{\rm fd}(\boldsymbol{x},\sigma_0,\sigma_1)=\mathcal{S}_{\rm fd}(\boldsymbol{x},\sigma_0,\sigma_1)+\mathcal{R}_{\rm fd}(\boldsymbol{x}).\tag{5.52}$$

For image registration and interpolation by means of optical flow, (5.7) is modified as follows [46]:

$$J_{{\rm of},i}(\boldsymbol{u},I^{(0)},I^{(1)},\sigma_0,\sigma_1)=\mathcal{S}_{\rm of}(\boldsymbol{u},I^{(0)},I^{(1)},\sigma_0,\sigma_1)+\mathcal{R}_{{\rm of},i}(\boldsymbol{u})\tag{5.53}$$

subject to (5.50) and (5.51). The intensity I used to compute the optical flow in (5.22) or (5.27) is:

$$I=[I^{(0)}+I^{(1)}]/2.\tag{5.54}$$

This intensity permits reciprocal scaling and avoids intensity variations, such as in

$$\mathcal{I}(\boldsymbol{x},z)=(1-z)I^{(0)}(\boldsymbol{x},z)+zI^{(1)}(\boldsymbol{x},z),\tag{5.55}$$

which result only from scaling differences as opposed to misregistration. On the other hand, once the optical flow has been computed, the intensity $\mathcal{I}$ is a more suitable interpolation than I.

The cost $J_{\rm fd}$ is stationary in the displacement $\boldsymbol{x}$ for fixed σ_0 and σ_1 when $\boldsymbol{x}$ satisfies (5.12), where $F_{\rm fd}$ in (5.14) is modified as follows [46]:

$$\begin{aligned}
F_{\rm fd}(\boldsymbol{x},\bar{\boldsymbol{x}}) &= \int_{\Omega_0^{\rm c}}\left[\sigma_0(I_0(\boldsymbol{\xi}))-I_1(\boldsymbol{x}(\boldsymbol{\xi}))\right]\nabla_{\boldsymbol{x}}I_1(\boldsymbol{x}(\boldsymbol{\xi}))^{\rm T}\bar{\boldsymbol{x}}(\boldsymbol{\xi})d\boldsymbol{\xi}\\
&+ \int_{\Omega_1^{\rm c}}[I_0(\boldsymbol{y}(\boldsymbol{\eta}))-\sigma_1(I_1(\boldsymbol{\eta}))]\nabla_{\boldsymbol{y}}I_0(\boldsymbol{y}(\boldsymbol{\eta}))^{\rm T}\nabla_{\boldsymbol{\eta}}\boldsymbol{y}(\boldsymbol{\eta})\bar{\boldsymbol{x}}(\boldsymbol{y}(\boldsymbol{\eta}))d\boldsymbol{\eta}.
\end{aligned}\tag{5.56}$$

Then, (5.12) is solved by the quasi-Newton iteration in (5.15). The cost J_{of} is stationary in the intensities $I^{(0)}$ and $I^{(1)}$ for fixed $\boldsymbol{u}$, σ_0 and σ_1 when $I^{(0)}$ and $I^{(1)}$ satisfy the following [46]:

$$I^{(0)}(\boldsymbol{x}(\boldsymbol{\xi},\zeta),\zeta) = \begin{cases} I_0(\boldsymbol{\xi})[1-U(\boldsymbol{\xi},\zeta,1)] + \sigma_1(I_1(\boldsymbol{x}(\boldsymbol{\xi},1)))U(\boldsymbol{\xi},\zeta,1), & \boldsymbol{\xi}\in\Omega_0^{\mathrm{c}} \\ I_0(\boldsymbol{\xi})[1-U(\boldsymbol{\xi},\zeta,\acute{\zeta})] + \sigma_1(I_1^{\infty})U(\boldsymbol{\xi},\zeta,\acute{\zeta}), & \boldsymbol{x}(\boldsymbol{\xi},\acute{\zeta})\in\Gamma,\ \boldsymbol{\xi}\in\Omega_0^{\mathrm{i}} \end{cases}$$

$$I^{(1)}(\boldsymbol{x}(\boldsymbol{\xi},\zeta),\zeta) = \begin{cases} \sigma_0(I_0(\boldsymbol{\xi}))[1-U(\boldsymbol{\xi},\zeta,1)] + I_1(\boldsymbol{x}(\boldsymbol{\xi},1))U(\boldsymbol{\xi},\zeta,1), & \boldsymbol{\xi}\in\Omega_0^{\mathrm{c}} \\ \sigma_0(I_0(\boldsymbol{\xi}))[1-U(\boldsymbol{\xi},\zeta,\acute{\zeta})] + I_1^{\infty}U(\boldsymbol{\xi},\zeta,\acute{\zeta}), & \boldsymbol{x}(\boldsymbol{\xi},\acute{\zeta})\in\Gamma,\ \boldsymbol{\xi}\in\Omega_0^{\mathrm{i}} \end{cases} \tag{5.57}$$

and:

$$I^{(0)}(\boldsymbol{y}(\boldsymbol{\eta},\zeta),\zeta) = \begin{cases} \sigma_1(I_1(\boldsymbol{\eta}))[1-V(\boldsymbol{\eta},0,\zeta)] + I_0(\boldsymbol{y}(\boldsymbol{\eta},0))V(\boldsymbol{\eta},0,\zeta), & \boldsymbol{\eta}\in\Omega_1^{\mathrm{c}} \\ \sigma_1(I_1(\boldsymbol{\eta}))[1-V(\boldsymbol{\eta},\grave{\zeta},\zeta)] + I_0^{\infty}V(\boldsymbol{\eta},\grave{\zeta},\zeta), & \boldsymbol{y}(\boldsymbol{\eta},\grave{\zeta})\in\Gamma,\ \boldsymbol{\eta}\in\Omega_1^{\mathrm{i}} \end{cases}$$

$$I^{(1)}(\boldsymbol{y}(\boldsymbol{\eta},\zeta),\zeta) = \begin{cases} I_1(\boldsymbol{\eta})[1-V(\boldsymbol{\eta},0,\zeta)] + \sigma_0(I_0(\boldsymbol{y}(\boldsymbol{\eta},0)))V(\boldsymbol{\eta},0,\zeta), & \boldsymbol{\eta}\in\Omega_1^{\mathrm{c}} \\ I_1(\boldsymbol{\eta})[1-V(\boldsymbol{\eta},\grave{\zeta},\zeta)] + \sigma_0(I_0^{\infty})V(\boldsymbol{\eta},\grave{\zeta},\zeta), & \boldsymbol{y}(\boldsymbol{\eta},\grave{\zeta})\in\Gamma,\ \boldsymbol{\eta}\in\Omega_1^{\mathrm{i}} \end{cases} \tag{5.58}$$

where $\acute{\zeta}$, $\grave{\zeta}$, U and V have the same definitions as for (5.57) and (5.58). The cost $J_{\mathrm{of},i}$ is stationary in the optical flow $\boldsymbol{u}$ for fixed $I^{(0)}$, $I^{(1)}$, σ_0 and σ_1 when $\boldsymbol{u}$ satisfies (5.22) or (5.27), where the intensity I is given by (5.54) [46].

The optimality conditions for the scaling functions can be described roughly as follows. The value of $\sigma_0(\iota)$ should be a weighted average over the level set $I_0(\boldsymbol{\xi})=\iota$ of the intensities obtained by morphing I_1 to Ω_0. The scaling function σ_1 should satisfy the reciprocal property. The optimality conditions are shown precisely in [46] to be given as follows. Let $\check{\iota}_0$, $\hat{\iota}_0$, $\check{\iota}_1$ and $\hat{\iota}_1$ be determined by minimum and maximum values of I_0 and I_1 so that the ranges of I_0 and I_1 are contained respectively in $[\check{\iota}_0,\hat{\iota}_0]$ and $[\check{\iota}_1,\hat{\iota}_1]$. Then assume that $|\nabla I_0|=0$ when I_0 assumes values $K_0\subset[\check{\iota}_0,\hat{\iota}_0]$ and $|\nabla I_1|=0$ when I_1 assumes values $K_1\subset[\check{\iota}_1,\hat{\iota}_1]$. Then the optimal σ_0 and σ_1 necessarily satisfy:

$$\sigma_0(\iota) = \begin{cases} \left[\displaystyle\int_{I_0(\boldsymbol{\xi})=\iota}\mathcal{I}_1(\boldsymbol{\xi})\mathcal{U}(\boldsymbol{\xi})d\boldsymbol{\xi} + \int_{\Omega_1^{\mathrm{i}}} I_1(\boldsymbol{\eta})\mathcal{V}(\boldsymbol{\eta})d\boldsymbol{\eta}\right] \Big/ \\ \qquad\qquad \left[\displaystyle\int_{I_0(\boldsymbol{\xi})=\iota}\mathcal{U}(\boldsymbol{\xi})d\boldsymbol{\xi} + \int_{\Omega_1^{\mathrm{i}}}\mathcal{V}(\boldsymbol{\eta})d\boldsymbol{\eta}\right], & \iota = I_0^{\infty} \\ \displaystyle\int_{I_0(\boldsymbol{\xi})=\iota}\mathcal{I}_1(\boldsymbol{\xi})\mathcal{U}(\boldsymbol{\xi})d\boldsymbol{\xi} \Big/ \int_{I_0(\boldsymbol{\xi})=\iota}\mathcal{U}(\boldsymbol{\xi})d\boldsymbol{\xi}, & \iota\in K_0\backslash\{I_0^{\infty}\} \\ \displaystyle\int_{I_0(\boldsymbol{\xi})=\iota}\frac{\mathcal{I}_1(\boldsymbol{\xi})\mathcal{U}(\boldsymbol{\xi})d\boldsymbol{\xi}}{|\nabla I_0(\boldsymbol{\xi})|} \Big/ \int_{I_0(\boldsymbol{\xi})=\iota}\frac{\mathcal{U}(\boldsymbol{\xi})d\boldsymbol{\xi}}{|\nabla I_0(\boldsymbol{\xi})|}, & \iota\in[\check{\iota}_0,\hat{\iota}_0]\backslash K_0 \end{cases} \tag{5.59}$$

and:

$$\sigma_1(\iota) = \begin{cases} \left[\displaystyle\int_{I_1(\boldsymbol{\eta})=\iota}\mathcal{I}_0(\boldsymbol{\eta})\mathcal{V}(\boldsymbol{\eta})d\boldsymbol{\eta} + \int_{\Omega_0^{\mathrm{i}}} I_0(\boldsymbol{\xi})\mathcal{U}(\boldsymbol{\xi})d\boldsymbol{\xi}\right] \Big/ \\ \qquad\qquad \left[\displaystyle\int_{I_1(\boldsymbol{\eta})=\iota}\mathcal{V}(\boldsymbol{\eta})d\boldsymbol{\eta} + \int_{\Omega_0^{\mathrm{i}}}\mathcal{U}(\boldsymbol{\xi})d\boldsymbol{\xi}\right], & \iota = I_1^{\infty} \\ \displaystyle\int_{I_1(\boldsymbol{\eta})=\iota}\mathcal{I}_0(\boldsymbol{\eta})\mathcal{V}(\boldsymbol{\eta})d\boldsymbol{\eta} \Big/ \int_{I_1(\boldsymbol{\eta})=\iota}\mathcal{V}(\boldsymbol{\eta})d\boldsymbol{\eta}, & \iota\in K_1\backslash\{I_1^{\infty}\} \\ \displaystyle\int_{I_1(\boldsymbol{\eta})=\iota}\frac{\mathcal{I}_0(\boldsymbol{\eta})\mathcal{V}(\boldsymbol{\eta})d\boldsymbol{\eta}}{|\nabla I_1(\boldsymbol{\eta})|} \Big/ \int_{I_1(\boldsymbol{\eta})=\iota}\frac{\mathcal{V}(\boldsymbol{\eta})d\boldsymbol{\eta}}{|\nabla I_1(\boldsymbol{\eta})|}, & \iota\in[\check{\iota}_1,\hat{\iota}_1]\backslash K_1 \end{cases} \tag{5.60}$$

where the morphed images are given by:

$$\mathcal{I}_0(\boldsymbol{\eta}) = \begin{cases} I_0(\boldsymbol{y}), & \boldsymbol{y} = \boldsymbol{y}(\boldsymbol{\eta}) \text{ or } \boldsymbol{y}(\boldsymbol{\eta}, 0) \quad \boldsymbol{\eta} \in \Omega_1^{\mathrm{c}} \\ I_0^{\infty}, & \boldsymbol{\eta} \in \Omega_1^{\mathrm{i}} \end{cases} \tag{5.61}$$

$$\mathcal{I}_1(\boldsymbol{\xi}) = \begin{cases} I_1(\boldsymbol{x}), & \boldsymbol{x} = \boldsymbol{x}(\boldsymbol{\xi}) \text{ or } \boldsymbol{x}(\boldsymbol{\xi}, 1) \quad \boldsymbol{\xi} \in \Omega_0^{\mathrm{c}} \\ I_1^{\infty}, & \boldsymbol{\xi} \in \Omega_0^{\mathrm{i}}. \end{cases} \tag{5.62}$$

and for finite displacements, $\mathcal{U} = 1$ and $\mathcal{V} = 1$ hold, while for optical flow the following hold:

$$\mathcal{U}(\boldsymbol{\xi}) = \begin{cases} \displaystyle\int_0^1 U_\zeta^2(\boldsymbol{\xi}, \zeta, 1) \det\left(\nabla_{\boldsymbol{\xi}} \boldsymbol{x}\right) d\zeta, & \boldsymbol{\xi} \in \Omega_0^{\mathrm{c}} \\ \displaystyle\int_0^{\acute{\zeta}(\boldsymbol{\xi})} U_\zeta^2(\boldsymbol{\xi}, \zeta, \acute{\zeta}(\boldsymbol{\xi})) \det\left(\nabla_{\boldsymbol{\xi}} \boldsymbol{x}\right) d\zeta, & \boldsymbol{\xi} \in \Omega_0^{\mathrm{i}} \end{cases} \tag{5.63}$$

$$\mathcal{V}(\boldsymbol{\eta}) = \begin{cases} \displaystyle\int_0^1 V_\zeta^2(\boldsymbol{\eta}, 0, \zeta) \det\left(\nabla_{\boldsymbol{\eta}} \boldsymbol{y}\right) d\zeta, & \boldsymbol{\eta} \in \Omega_1^{\mathrm{c}} \\ \displaystyle\int_{\grave{\zeta}(\boldsymbol{\eta})}^1 V_\zeta^2(\boldsymbol{\eta}, \grave{\zeta}(\boldsymbol{\eta}), \zeta) \det\left(\nabla_{\boldsymbol{\eta}} \boldsymbol{y}\right) d\zeta, & \boldsymbol{\eta} \in \Omega_1^{\mathrm{i}}. \end{cases} \tag{5.64}$$

Thus, σ_0 and σ_1 are given respectively by weighted averages of $\mathcal{I}_1$ and $\mathcal{I}_0$ over levels sets of of I_0 and I_1 respectively.

The importance of reciprocal scaling is shown in Fig. 30, where the image I_0 is shown in

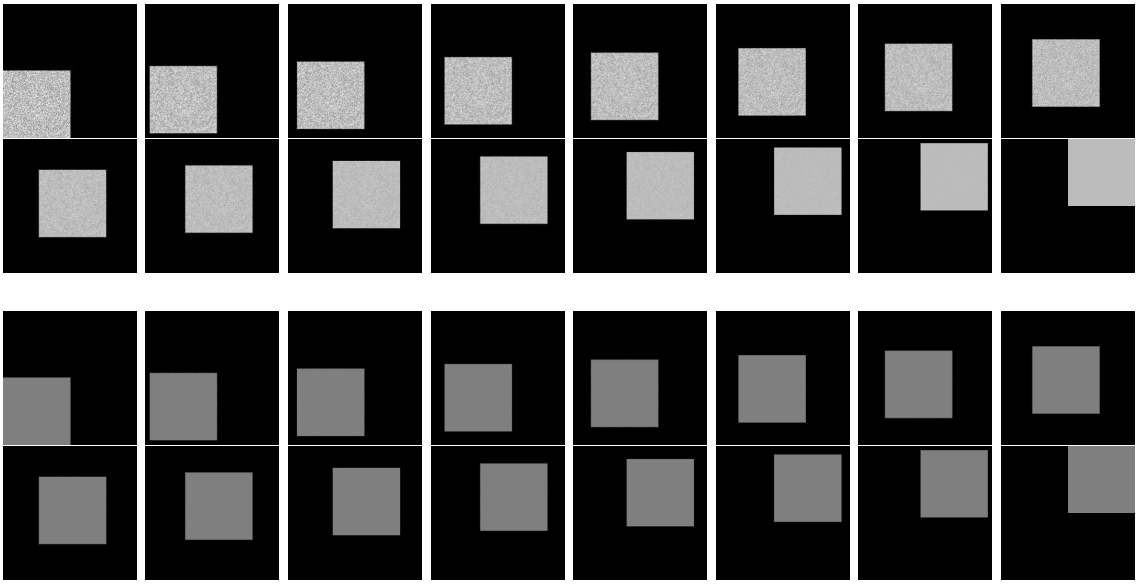

Figure 30: The two given images I_0 and I_1 are shown respectively in the extreme upper left and the extreme lower right. The intensities I and $\mathcal{I}$ are constructed for optical flow from $I^{(0)}$ and $I^{(1)}$ which are shown respectively in the top two and bottom two rows. Each sequence is to be read from left to right and from top to bottom.

the extreme upper left and the image I_1 is shown in the extreme lower right. These two images have quite different scalings and noise levels but are clearly related by a simple translation. An optical flow is used in [46] to interpolate between these images, and $I^{(0)}$ is shown in the top two rows while $I^{(1)}$ is shown in the bottom two rows. Note that $I^{(0)}$ is computed by scaling only I_1 with the average of the noisy non-trivial values in I_0. Also, $I^{(1)}$ is computed by scaling only I_0 with the (average of the) single non-trivial value in I_1. With $I^{(0)}$ the intensity differences between I_0 and $\sigma_1(I_1)$ drive changes in the registration. On the other hand, with $I^{(1)}$ the images

$\sigma_0(I_0)$ and I_1 are registered perfectly. Thus, reciprocal scaling as implemented in (5.54) and (5.55) is required for the registration to be independent of image order. The intensity I in (5.54) is the average of $I^{(0)}$ and $I^{(1)}$, and it is found to be more appropriate for determining the optical flow. The intensity $\mathcal{I}$ in (5.55) begins in Ω_0 with $I^{(0)}$ and ends in Ω_1 with $I^{(1)}$, and thus $\mathcal{I}$ is more appropriate for interpolating images once the optical flow has been determined. Both intensities are simply reflected when the image order is reversed. Such examples in [46] also suggests that scaling can have an image smoothing effect.

As can be seen from Fig. 31 shown below, the formulas (5.59) and (5.60) can lead to very irregular scaling functions, particularly when the given images are noisy. In such cases, Tikhonov regularization can be implemented by minimizing the following augmented cost functions:

$$J^{\nu}_{\mathrm{fd}}(\boldsymbol{x},\sigma_0,\sigma_1) = J_{\mathrm{fd}}(\boldsymbol{x},\sigma_0,\sigma_1) + \nu\int_0^1 |\sigma_0'(\iota)|^2 d\iota + \nu\int_0^1 |\sigma_1'(\iota)|^2 d\iota \quad (5.65)$$

$$J^{\nu}_{\mathrm{of}}(\boldsymbol{u},I^{(0)},I^{(1)},\sigma_0,\sigma_1) = J_{\mathrm{of}}(\boldsymbol{u},I^{(0)},I^{(1)},\sigma_0,\sigma_1) + \nu\int_0^1 |\sigma_0'(\iota)|^2 d\iota + \nu\int_0^1 |\sigma_1'(\iota)|^2 d\iota. \quad (5.66)$$

These estimations can be further simplified by making the realistic assumption that the images are cell-wise constant so that the ranges of I_0 and I_1 are K_0 and K_1 respectively. Under this assumption, let $\hat{\sigma}_0$ and $\hat{\sigma}_1$ denote the functions on the right sides of (5.59) and (5.60). Then the minimizers of the augmented costs above are determined by:

$$\left\{\begin{array}{rcll} -\nu\sigma_0''+\sigma_0 &=& \hat{\sigma}_0, & \iota\in(\check{\iota}_0,\hat{\iota}_0) \\ \sigma_0' &=& 0, & \iota=\check{\iota}_0,\hat{\iota}_0 \end{array}\right. \qquad \left\{\begin{array}{rcll} -\nu\sigma_1''+\sigma_1 &=& \hat{\sigma}_1, & \iota\in(\check{\iota}_1,\hat{\iota}_1) \\ \sigma_1' &=& 0, & \iota=\check{\iota}_1,\hat{\iota}_1. \end{array}\right. \quad (5.67)$$

The functions $\hat{\sigma}_0, \mathcal{I}_1, I_0$ and $\hat{\sigma}_1, \mathcal{I}_0, I_1$ are defined numerically in [46] in terms of cell centers of Ω_0 and Ω_1 respectively. The trajectory integrations (5.10), (5.11), (5.20), (5.21), (5.63) and (5.64) are approximated using a Runge-Kutta method, where multilinear interpolation is used to obtain distributed values of the optical flow and its divergence, and optical flow derivatives as well as metric terms, $\det[\nabla_{\boldsymbol{\xi}}\boldsymbol{x}(\mathbf{x}_{\boldsymbol{i}},\zeta)]$, $\det[\nabla_{\boldsymbol{\eta}}\boldsymbol{y}(\mathbf{x}_{\boldsymbol{i}},\zeta)]$, are computed using central differences. Thus, with $\hat{\sigma}_0$ and $\hat{\sigma}_1$ so determined from a given displacement or optical flow, the scaling functions are determined by (5.67), where derivatives are approximated by central differences in points ι in which values of $\hat{\sigma}_0$ and $\hat{\sigma}_1$ are given.

An alternative to the optimize-then-discretize approach outlined above is the discretize-then-optimize approach of minimizing the unaugmented cost functions in (5.52) and (5.53) over a finite-dimensional basis for the scaling functions. This approach is investigated in [46]. Specifically, let the intervals $[\check{\iota}_0,\hat{\iota}_0]$ and $[\check{\iota}_1,\hat{\iota}_1]$ be divided into uniform grids of subintervals. Then let $\{\psi_k^{(0)}\}$ and $\{\psi_k^{(1)}\}$ be the canonical linear splines which form a basis for the piecewise linear continuous functions on the respective grids. In terms of these bases, the scaling functions take the form:

$$\sigma_0(\iota) = \sum_k \alpha_k^{(0)}\psi_k^{(0)}(\iota), \qquad \sigma_1(\iota) = \sum_k \alpha_k^{(1)}\psi_k^{(1)}(\iota) \quad (5.68)$$

where the coefficients $\{\alpha_k^{(0)}\}$ and $\{\alpha_k^{(1)}\}$ are determined by minimizing the unaugmented cost functions, i.e., $\mathcal{S}_{\mathrm{fd}}$ in (5.48) or $\mathcal{S}_{\mathrm{of}}$ in (5.49). This basis functions approach is compared to the Tikhonov regularization approach in Fig. 31 for an example from [46] in which magnetic resonance images are registered. In order not to reduce the discrimination capacity of the image similarity measure excessively, regularization of the highly oscillatory functions, $\hat{\sigma}_0$ and $\hat{\sigma}_1$, is advantageous. The Tikhonov regularization approach is clearly regularizing, while the basis functions approach suffers extreme oscillations near large separations between isolated peaks in the respective histograms. The Tikhonov regularization approach is preferred in [46].

Thus, the algorithmic outlines of Subsection 5.2 are modified so that (5.67) is solved in each loop. For the optical flow computation, (5.63) and (5.64) are assembled at the same time other trajectories are computed. Also, (5.18) and (5.19) are replaced by (5.57), (5.58), (5.54)

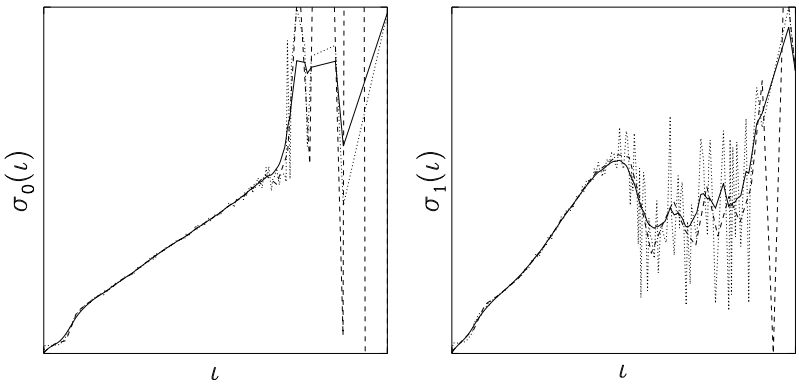

Figure 31: On the left are estimations of σ_0 and on the right are estimations of σ_1 for a registration example from [46]. The dotted curves are $\hat{\sigma}_0$ and $\hat{\sigma}_1$ respectively. The dashed curves are scaling functions obtained by the basis functions approach. The solid curves are scaling functions obtained by the Tikhonov regularization approach.

and (5.55) to obtain $I^{(0)}$, $I^{(1)}$, I and $\mathcal{I}$. Thus, the extra computational costs for implementing scaling functions are insignificant in relation to the work required to solve for the displacement field or for the optical flow.

To demonstrate the advantages of image scaling, examples involving magnetic resonance images are presented in [46]. In one example, contrast agent appears in one image of a hand and not in another, and scaled images naturally remove the effect of altered intensities and thus permit a closer registration match than with unscaled images. In another example, the first two images of Fig. 13 are registered, and the match between scaled images is conspicuously closer than that between unscaled images. In both of these examples, images are registered by finite displacements, although no large displacements are manifested and thus image similarity is the focus. On the other hand, respiratory motion accompanies the sudden and widespread appearance of contrast agent in the example of Fig. 29 in which generalized rigid optical flow is used to interpolate between the end images in Fig. 29. Note from Fig. 30 that neither of the intensities $I^{(0)}$ or $I^{(1)}$ are an adequate interpolation; nevertheless, the interpolated images of Fig. 29, given by $\mathcal{I}$ in (5.55), are well suited to the interpolation problem.

6 Summary of Continuing Investigations

The work of [53] and [44] was motivated by the need for segmentation preprocessing to extract the morphology of vessels from magnetic resonance images [3], [76], [4]. Such vessels are shown *in vitro* in Fig. 4, but when such vessels are measured *in vivo*, the images may be corrupted by intensity modulations as seen in Fig. 13 or even by the appearance of contrast agent as seen in Fig. 29. Thus, it is required to modify segmentation formulations, such as with $m = 1$ in the following Mumford-Shah functional [64] [39],

$$J(u, m, \Gamma) = \int_\Omega |m \cdot u - \tilde{u}|^2 d\boldsymbol{x} + \alpha \int_{\Omega \setminus \Gamma} |\nabla u|^2 d\boldsymbol{x} + \beta \cdot \mu(\Gamma) + \gamma \sum_{|\omega|=\nu} \frac{\nu!}{\omega!} \int_\Omega |\partial^\omega m|^2 d\boldsymbol{x} \quad (6.69)$$

with the product structure of $m \cdot u$, where the smooth modulation m and the bounded variation intensity u have very different regularity character. Also a similar product should be introduced into the image registration and interpolation formulations when the given images are similarly modulated. Such product structures will be studied theoretically and computationally in forthcoming research.

Note that this product structure appears as well in (4.17). Furthermore, the minimization of (4.17) will be investigated by introducing multigrid techniques into the pre-dual formulation of [38]. However, the most important goal in the investigation of (4.17) is the determination

of sampling strategies, which appear as the convolution with K in (4.17), in order to improve parallel imaging strategies such as [71] and [32].

The deconvolution approach of (3.1) for determining transport properties from images such as seen in Fig. 7 is based upon the standard established in [83], and it involves no correlation between neighboring pixels. On the other hand, convection and diffusion of contrast agent, as seen in (3.11), clearly implies a coupling, and the spatial correlation evident in the differences of Fig. 9 further suggests that the coupling is nontrivial. Two approaches for investigating this coupling are planned. One approach involves joint work with the author of [30] using related regularization techniques to correlate the pixelwise results of deconvolving (3.1). Another approach involves to expand estimation techniques of [11] for the estimation of coefficients, particularly convection, in (3.11).

Note also in the images shown in Fig. 9 that macro-vessels appear conspicuously while the goal is to identify transport properties of tissues. It has been shown that the macro-vessel signal can corrupt the tissue signal, and independent component analysis has been used successfully in [72] to separate and remove the macro-vessel signal. It is also found in [72] that independent component analysis can be used successfully for denoising. In addition it is thought that the approach can be used to guide object oriented registration and interpolation within image sequences such as those seen in Figs. 28 and 29 and investigated in current projects such as [13]. For such image processing tasks independent component analysis will be studied theoretically and computationally in forthcoming research.

Acknowledgments

Working together with the members of the Institute of Mathematics and Scientific Computing of the University of Graz is a pleasure, and the author thanks his colleagues for such a pleasant atmosphere, indeed for their valued friendship. In particular the author would like very much to express gratitude to Professors Karl Kunisch and Franz Kappel for their support of the author's professional goals and for their creation of a rich mathematical environment which acts as a catalyst for the synergetic pursuit of such goals. The research projects presented here, both completed and forthcoming, have been stimulated by many individual discussions and seminar interactions at the Institute as well as interdisciplinary exchanges with close colleagues at the Medical University of Graz who have been drawn by shared interests to a successful Special Research Center on Optimization and Control.

References

[1] R. Acar and C.R. Vogel, *Analysis of Bounded Variation Penalty Methods for Ill-Posed Problems*, Inverse Problems, Vol. 18, pp. 1217–1229, 1994.

[2] J. Aubin, *Approximation of Elliptic Boundary-Value Problems*, Krieger, Huntington, New York, 1980.

[3] M. Auer, C. Schulze-Bauer, R. Stollberger, P. Regitnig, F. Ebner, and G. Holzapfel, *Extracting morphology models of atherosclerotic arteries from MR images*, 13th Conference of the European Society of Biomechanics, Wroclaw, Poland, September 1–4, 2002.

[4] M. Auer, R. Stollberger, P. Regitnig, F. Ebner, and G. Holzapfel, *3-D Reconstruction of Tissue Components for Atherosclerotic Human Arteries Using ex vivo High-Resolution MRI*, IEEE Transactions on Medical Imaging, Vol. 25, No. 3, pp. 345–357, March 2006.

[5] M.A.G. Ballester, Y. Machida, Y. Kassai, Y. Hamamura and H. Sugimoto, *Robust Estimation of Coil Sensitivities for RF Subencoding Acquisition Techniques*, Annual Meeting of ISMRM, Glasgow, April 21-27, 2001.

[6] R. Bammer, M. Auer, S.L. Keeling, M. Augustin, L.A. Stables, R.W. Prokesch, R. Stollberger, M.E. Moseley and F. Fazekas, *Diffusion Tensor Imaging Using Single-Shot SENSE-EPI*, Magnetic Resonance in Medicine, Vol. 48, No. 1, pp. 128–136, July 2002.

[7] R. Bammer, S.L. Keeling, M. Auer, K.P. Pruessmann, P. Roeschmann, R. Stollberger, F. Fazekas, *Diffusion Tensor Imaging using SENSE-Single-Shot EPI*, Proceedings of the Ninth Annual Meeting of the International Society for Magnetic Resonance in Medicine, Glasgow, April 21-27, 2001.

[8] R. Bammer, S.L. Keeling, M. Augustin, K.P. Pruessmann, R. Wolf, R. Stollberger, H. Hartung and F. Fazekas, *Improved Diffusion-Weighted Single-Shot Echo-Planar Imaging in Stroke using Sensitivity Encoding*, Magnetic Resonance in Medicine, Vol. 46, No. 3, pp. 548–554, September 2001.

[9] R. Bammer, S.L. Keeling, M. Augustin, K.P. Pruessmann, C. Leussler and F. Fazekas, *Improved Diffusion-Weighted Single-Shot EPI in Stroke using SENSE*, Annual Meeting of ISMRM the International Society for Magnetic Resonance in Medicine, Glasgow, April 21-27, 2001.

[10] R. Bammer, R. Stollberger, M. Augustin, T. Seifert, S. Strasser-Fuchs, H.P. Hartung and F. Fezekas, *Parallel Imaging Strategies for High-Speed Magnetic Resonance Diffusion Imaging*, SPIE International Symposium on Medical Imaging, San Diego, CA, February 12-18, 2000.

[11] H.T. Banks and K. Kunisch, *Estimation Techniques for Distributed Parameter Systems*, Birkhäuser, Boston, 1989.

[12] B. Benhamouda, *Parameter Adaptation for Nonlinear Diffusion in Image Processing*, Master's Thesis, Dept. of Mathematics, University of Kaiserslautern, P.O. Box 3049, 67653 Kaiserslautern, Germany, 1994.

[13] R. Burton, G. Plank, J. Schneider, A.J. Prassl, J. Lee, V. Grau, N. Smith, N. Trayanova, P. Kohl, H. Ahammer and S.L. Keeling, *3-Dimensional Models of Individual Cardiac Histo-Anatomy: Tools and Challenges*, to appear in the Annals of the New York Academy of Sciences.

[14] E. Casas, K. Kunisch and C. Pola, *Regularization by Functions of Bounded Variation and Applications to Image Enhancement*, Applied Mathematics and Optimization, Vol. 40, pp. 229–257.

[15] F. Calamante, D.G. Gadian and A. Connelly, *Quantification of Bolus Tracking MRI: Improved Characterization of the Tissue Residue Function using Tikhonov Regularisation*, Magnetic Resonance in Medicine, Vol. 50, No. 6, pp. 1237–1247, 2003.

[16] E. Carson and C. Cobelli, *Modeling Methodology for Physiology and Medicine*, Academic Press, 2000.

[17] G.E. Christensen and H.J. Johnson, *Consistent Image Registration*, IEEE Trans. Med. Imaging. Vol. 20, No. 7, July 2001, pp. 568-582.

[18] P.G. Ciarlet, *The Finite Element Method for Elliptic Problems*, North-Holland, Amsterdam, New York, Oxford, 1978.

[19] V.J. Cunningham and T. Jones, *Spectral Analysis of Dynamic PET Studies*, Journal of Cerebral Blood Flow and Metabolism, Vol. 13, No. 1, pp. 15–23, 1993.

[20] M. Droske and W. Ring, *A Mumford-Shah Level-Set Approach for Geometric Image Registration*, Preprint Series DFB-SPP 1114, Preprint 99, April 2005.

[21] M. Droske and M. Rumpf, *A Variational Approach to Non-Rigid Morphological Registration*, SIAM J. Appl. Math., Vol. 64, No. 2, pp. 668–687, 2004.

[22] H.W. Engl, M. Hanke and A. Neubauer, *Regularization of Inverse Problems*, Kluwer, Dordrecht, 1996.

[23] L.C. Evans and R. Gariepy, *Measure Theory and Fine Properties of Functions*, CRC Press, Boca Raton, 1992.

[24] A. Fan, W.M. Wells, J.W. Fischer, M. Cetin, S. Haker, R. Mulkern, C. Tempany and A.S. Willsky, *A Unified Variational Approach to Denoising and Bias Correction in MR*, Proceedings of IPMI 2003, Springer LNCS 2732, pp. 148–159, Jul 2003.

[25] B. Fischer and J. Modersitzki, *Curvature Based Image Registration*, J. Math. Imaging and Vision 18, pp. 81–85, 2003.

[26] B. Fischer and J. Modersitzki, *Fast Inversion of Matrices Arising in Image Processing*, Numerical Algorithms 22, pp. 1–11, 1999.

[27] B.G. Fitzpatrick and S.L. Keeling, *On Approximation in Total Variation Penalization for Image Reconstruction*, Numerical Functional Analysis and Optimization, Vol. 18, Nos. 9 and 10, pp. 941–958, 1997.

[28] B.G. Fitzpatrick, S.L. Keeling and S.G. Rock, *A Bounded Variation Approach to Inverse Interferometry*, Proceedings of the Fifteenth ASME Conference on Mechanical Vibration and Noise, Boston, MA, September 17–21, 1995.

[29] A. Friedman, *Partial Differential Equations*, Holt, Rinehart and Winston, Inc., New York, 1969.

[30] F. Greensite, *The Temporal Prior in Bioelectromagnetic Source Imaging Problems*, IEEE Transactions on Biomedical Engineering, Vol. 50, No. 10, pp. 1152-1159, 2003.

[31] J. Griebel, S. Pahernik, R. Lucht, A. DeVries, K.-H. Englmeier, M. Dellian and G. Brix, *Perfusion and Permeability: Can Both Parameters Be Evaluated Separately from Dynamic MR Data?*, Proceedings of the Ninth Annual Meeting of the International Society for Magnetic Resonance in Medicine, Glasgow, April 21-27, 2001.

[32] M.A. Griswold, P.M. Jakob, R.M. Heidemann, M. Nittka, V. Jellus, J. Wang, B. Kiefer and A. Haase, *Generalized autocalibrating partially parallel acquisitions (GRAPPA)*, Magnetic Resonance in Medicine, Vol. 47, No. 6, pp. 1202-1210, June 2002.

[33] S. Haker, A. Tannenbaum, and R. Kikinis, *Mass Preserving Mappings and Image Registration*, MICCAI 2001, pp. 120–127.

[34] W. Hackbusch, *Iterative Solution of Large Sparse Systems of Equations*, Springer, 1993.

[35] E. Henderson, J.S. Sykes, D. Drost, H.-J. Weinmann, B.K. Rutt and T.-Y. Lee, *Simultaneous MRI Measurement of Blood Flow, Blood Volume, and Capillary Permeability in Mammary Tumors Using Two Different Contrast Agents*, Journal of Magnetic Resonance Imaging, Vol. 12, pp. 991–1003, 2000.

[36] S. Henn and K. Witsch, *Iterative Multigrid Regularization Techniques for Image Matching*, SIAM Journal of Scientific Computing, Vol. 23, No. 4, pp. 1077–1093, 2001.

[37] S. Henn, *A Multigrid Method for a Fourth-Order Diffusion Equation with Application to Image Processing*, SIAM Journal of Scientific Computing, Vol. 27, No. 3, pp. 831–849, 2005.

[38] M. Hintermüller and K. Kunisch, *Total Bounded Variation Regularization as a Bilaterally Constrained Optimization Problem*, SIAM Journal on Applied Mathematics, Vol. 64, No. 4, pp. 1311–1333, 2004.

[39] M. Hintermüller and W. Ring, *A Second-Order Shape Optimization Approach for Image Segmentation*, SIAM Journal on Applied Mathematics, Vol. 64, No. 2, pp. 442–467, 2003.

[40] K. Höllig, *Finite Element Methods with B-Splines*, Frontiers in Applied Mathematics 26, SIAM, 2003.

[41] B.K.P. Horn and B.G. Schunck, *Determining Optical Flow*, Artificial Intelligence, Vol. 23, pp. 185 – 203, 1981.

[42] K. Ito and K. Kunisch, *Restoration of Edge-Flat-Grey Scale Images*, Inverse Problems, Vol. 65, pp. 273–298, 2000.

[43] S.S. Kety, *The Theory and Applications of the Exchange of Inert Gas at the Lungs and Tissues*, Pharmacological Review, Vol. 3, pp. 1–41, 1951.

[44] S.L. Keeling, *Total Variation Based Convex Filters for Medical Imaging*, Applied Mathematics and Computation, Vol. 139, pp. 101-119, 2003.

[45] S.L. Keeling, *Geometric Multigrid for Generalized Affine and Generalized Rigid Image Registration*, submitted to the Journal of Mathematical Imaging and Vision.

[46] S.L. Keeling, *Image Similarity Based on Intensity Scaling*, submitted to the Journal of Mathematical Imaging and Vision.

[47] S.L. Keeling, *Medical Image Registration and Interpolation by Optical Flow with Maximal Rigidity*, *Mathematical Methods in Registration for Applications in Industry and Medicine*, O. Scherzer, ed., Mathematics in Industry, Springer Series, to appear.

[48] S.L. Keeling and R. Bammer, *A Variational Approach to Magnetic Resonance Coil Sensitivity Estimation*, Applied Mathematics and Computation, Vol. 158, No. 2, pp. 53–82, 2004.

[49] S.L. Keeling, R. Bammer and R. Stollberger, *Revision of the Theory of Tracer Transport and the Convolution Model of Dynamic Contrast Enhanced Magnetic Resonance Imaging*, submitted to the Journal of Mathematical Biology.

[50] S.L. Keeling and G. Haase, *Geometric Multigrid for High-Order Regularizations of Early Vision Problems*, submitted to Applied Mathematics and Computation.

[51] S.L. Keeling, T. Kogler and R. Stollberger, *Nonparametric Deconvolution Approaches to Dynamic Contrast Enhanced Magnetic Resonance Imaging*, submitted to Medical Image Analysis.

[52] S.L. Keeling and W. Ring, *Medical Image Registration and Interpolation by Optical Flow with Maximal Rigidity*, Journal of Mathematical Imaging and Vision, Vol. 23, No. 1, pp. 47–65, July 2005.

[53] S.L. Keeling and R. Stollberger, *Nonlinear Anisotropic Diffusion Filters for Multiscale Edge Enhancement*, Inverse Problems, Vol. 18, pp. 175–190, January 2002.

[54] S.H. Lai and B.C. Vemuri, *Physically-based Adaptive Preconditioning for Early Vision*, IEEE Transactions on Pattern Analysis and Machine Intelligence, Vol. 19, No. 6, pp. 594–607, 1997.

[55] U. Langer, *Iterative Solution of Some Schemes of the Finite Element Method for Elliptic Equations of Order* $2n$*,* $n \geq 1$, U.S.S.R. Comput. Maths. Math. Phys., Vol. 23, No. 4, pp. 69–76, 1983.

[56] J.E. Lavery, *Shape-Preserving, Multiscale Interpolation by Bi- and Multivariate Cubic* L_1 *Splines*, CAGD, Vol. 18, No. 4, pp. 321–343, 2001.

[57] K.S. St. Lawrence and T.Y. Lee, *An Adiabatic Approximation to the Tissue Homogeneity Model for Water Exchange in the Brain. I. Theoretical Derivation*, Journal of Cerebral Blood Flow and Metabolism, Vol. 18, pp. 1365–1377, 1998.

[58] M. Lefébure and L.D. Cohen, *Image Registration, Optical Flow and Local Rigidity*, Journal of Mathematical Imaging and Vision, Vol. 14, No. 2, pp. 131–147, March 2001,

[59] X. Li and T. Chen, *Nonlinear Diffusion with Multiple Edginess Thresholds*, Pattern Recognition, Vol. 27, pp. 1029 – 1037, 1994.

[60] J.A. Little, D.L.G. Hill, and D.J. Hawkes, *Deformations Incorporating Rigid Structures*, Computer Vision and Image Understanding, Vol. 66, No. 2, pp. 223–232, 1997.

[61] F. Lin, L.L. Wald, Y. Chen and J.W. Belliveau, *Estimation of Coil Sensitivity Map and Correction of Surface Coil Magnetic Resonance Images using Wavelet Decomposition*, Annual Meeting of ISMRM, Glasgow, April 21-27, 2001.

[62] G. Meurant, *Computer Solution of Large Linear Systems*, Elsevier, New York, 1999.

[63] J. Modersitzki, *Numerical Methods for Image Registration*, Oxford University Press, 2004.

[64] D. Mumford and J. Shah, *Optimal Approximations by Piecewise Smooth Functions and Associated Variational Problems*, Communications of Pure and Applied Mathematics, Vol. 42, No. 5, pp. 577-685, 1989.

[65] N. Nordström, *Biased Anisotropic Diffusion – A Unified Regularization and Diffusion Approach to Edge Detection*, Image and Vision Computing, Vol. 8, pp. 318 – 327, 1990.

[66] S. Osher and L.I. Rudin, *Feature-Oriented Image Enhancement Using Shock Filters*, SIAM J. Numer. Anal., Vol. 27, No. 4, pp. 919 – 940, August 1990.

[67] L. Østergaard, R.M. Weisskoff, D.A. Chesler, C. Glydensted, and B.R. Rosen, *High Resolution Measurement of Cerebral Blood Flow using Intravascular Tracer Bolus Passages. Part I: Mathematical Approach and Statistical Analysis*, Magnetic Resonance in Medicine, Vol. 36, pp. 715–725, 1996.

[68] W. Peckar, C. Schnörr, K. Rohr and H.S. Stiehl, *Parameter-Free Elastic Deformation Approach for 2D and 3D Registration using Prescribed Displacements*, Journal of Mathematical Imaging and Vision, Vol. 10, pp. 143–162, 1999.

[69] P. Perona and J. Malik, *Scale Space and Edge Detection Using Anisotropic Diffusion*, Proc. IEEE Comp. Soc. Workshop on Computer Vision, Miami Beach, November 30 – December 2, 1987, IEEE Computer Society Press, Washington, pp. 16 – 22, 1987.

[70] T. Poggio, V. Torre and C. Koch, *Computational Vision and Regularization Theory*, Nature, Vol. 317, pp 314-319, 1985.

[71] K.P. Pruessman, M. Weiger, M.B. Scheidegger and P. Boesiger, *SENSE: sensitivity encoding for fast MRI*, Magn. Reson. Med., 42: 952–962 (1999).

[72] G. Reishofer, F. Fazekas, S.L. Keeling, C. Enzinger, J. Simbrunner and R. Stollberger, *Minimizing Macro Vessel Signal in Cerebral Perfusion Imaging Using Independent Component Analysis*, to appear in Magnetic Resonance in Medicine.

[73] L.I. Rudin, S. Osher and E. Fatemi, *Nonlinear Total Variation Based Noise Removal Algorithms*, Physica D, Vol. 60, pp. 259–268, 1992.

[74] D. Rueckert, L.I. Sonoda, C. Hayes, D.L.G. Hill, M.O. Leach and D.J. Hawkes, *Non-rigid Registration using Free-Form Deformations: Application to Breast MR Images*, IEEE Trans. Med. Imaging, Vol. 18, No. 8, pp. 712–721, 1999.

[75] C. Schnörr, *Unique Reconstruction of Piecewise-Smooth Images by Minimizing Strictly Convex Nonquadratic Functionals*, J. Math. Imaging and Vision, Vol. 4, pp. 189 - 198, 1994.

[76] Ch.A.J. Schulze-Bauer, M. Stadler, R. Stollberger, P. Regitnig and G.A. Holzapfel, *Assessment of Plaque Stability Based on High-Resolution Magnetic Resonance Imaging of Human Atheroschlerotic Lesions and Computational Mechanical Analysis*, Computational Bioengineering: Current Trends and Applications, Imperial College Press: Singapore, pp. 101–115, 2004.

[77] P.S. Tofts, *Modeling Tracer Kinetics in Dynamic Gd-DTPA MR Imaging*, J. Magn. Reson. Imaging, Vol 7, pp. 91–101, 1997.

[78] U. Trottenberg, C. Oosterlee and A. Schüller, *Multigrid*, Academic Press, San diego, San Francisco, New York, Boston, London, Sydney, Tokyo, 2001.

[79] C.R. Vogel and M.E. Oman, *Iterative Methods for Total Variation Denoising*, SIAM Journal on Scientific Computing, Vol. 17, pp. 227-238, 1996.

[80] J. Weickert, *Anisotropic Diffusion in Image Processing*, B. G. Teubner Stuttgart, 1998.

[81] R.T. Whitaker and S.M. Pizer, *A Multi-Scale Approach to Nonuniform Diffusion*, CVGIP: Image Understanding, Vol. 57, pp. 99 – 110, 1993.

[82] K.L. Zierler, *Theoretical Basis of Indicator-Dilution Methods for Measuring Flow and Volume*, Circulation Research, Vol. 10, pp. 393–407, March 1962.

[83] K.L. Zierler, *Theory of Use of Indicators to Measure Blood Flow and Extracellular Volume and Calculation of Transcapillary Movement of Tracers*, Circulation Research, Vol. 12, pp. 464–471, May 1962.